ISSN: 2164-5388 Volume 11, Number 2, April 2021

Scientific Research Publishing

Open Journal of Biophysics

ISSN: 2164-5388

https://www.scirp.org/journal/ojbiphy

Journal Editorial Board

ISSN Print: 2164-5388 ISSN Online: 2164-5396
https://www.scirp.org/journal/ojbiphy

Associate Editors

Editorial Board

Scientific Research Publishing

Open Journal of Biophysics, 2021, 11, 133-224
https://www.scirp.org/journal/ojbiphy
ISSN Online: 2164-5396
ISSN Print: 2164-5388

Table of Contents

Volume 11 Number 2 April 2021

Open Journal of Biophysics (OJBIPHY)
Journal Information

SUBSCRIPTIONS

The *Open Journal of Biophysics* (Online at Scientific Research Publishing, https://www.scirp.org/) is published quarterly by Scientific Research Publishing, Inc., USA.

Subscription rates:
Print: $79 per issue.
To subscribe, please contact Journals Subscriptions Department, E-mail: sub@scirp.org

SERVICES

Advertisements
Advertisement Sales Department, E-mail: service@scirp.org

Reprints (minimum quantity 100 copies)
Reprints Co-ordinator, Scientific Research Publishing, Inc., USA.
E-mail: sub@scirp.org

COPYRIGHT

PRODUCTION INFORMATION

For manuscripts that have been accepted for publication, please contact:
E-mail: ojbiphy@scirp.org

Scientific Research Publishing

Open Journal of Biophysics, 2021, 11, 133-146
https://www.scirp.org/journal/ojbiphy
ISSN Online: 2164-5396
ISSN Print: 2164-5388

The Spreading Depression Propagation: How Electrochemical Patterns Distort or Create Perception

Vera Maura Fernandes de Lima[1], Alfredo Pereira Junior[2], Guilherme Lima de Oliveira[3]

[1]Centro de Biotecnologia CNEN/IPEN-SP, São Paulo, Brazil
[2]Department of Human and Nutritional Sciences, Biosciences Inst., UNESP, Botucatu, São Paulo, Brazil
[3]São Paulo, Brazil
Email: vmflima@ipen.br, guivillares@gmail.com, alfredo.pereira@unesp.br

How to cite this paper: de Lima, V.M.F., Pereira Jr., A. and de Oliveira, G.L. (2021) The Spreading Depression Propagation: How Electrochemical Patterns Distort or Create Perception. *Open Journal of Biophysics*, **11**, 133-146.
https://doi.org/10.4236/ojbiphy.2021.112003

Received: November 26, 2020
Accepted: February 5, 2021
Published: February 8, 2021

Abstract

At the transition from quiescence to propagating waves recorded in isolated retinas, a circular electric current closes in the extracellular matrix; this circular current creates a magnetic torus flow that, when entering quiescent tissue in front of the wave, recruits elements and when leaving behind, helps to build the absolute refractory state. The waving magnetic torus is the consequence of the vortex effect and explains the energy boost that drives propagation. **Methods:** We interpret experimental results from intrinsic and extrinsic fluorescence dyes, voltage, calcium and pH sensitive, optical signals from isolated retinas, and time series recordings using ion exchange resins: Ca, K, pH, Na, Cl recorded extracellularly at retinas, cerebellums and cortices coupled to spreading depression waves. Finally, we checked the ECoG activity, also a time series, at the transition from after discharges to spreading depression in rat hippocampus. **Results:** The integrated assessment of the diversified measurements led to the realization that the magnetic flow at the wavefront is a major contributor to the wave propagation mechanisms. This flow couples mass and charge flows as a swirling torus from excited to quiescent tissue. **Conclusions:** An alternative model of the brain is possible, apart from the classical HH and molecular biology model. Physical chemistry of charged gels and its flows explains the results. The conceptual framework uses far from equilibrium thermodynamics.

Keywords

Brain Electrochemistry, Retinal Model, Resonance, Spreading Depression, Functional CNS Syndromes, Vortex Effect

1. Introduction

The power of the vortex effect in separating matter and energy is known to mankind since millennia. Our species learned how to use it since antiquity, in obtaining drinking water and air conditioning buildings in desertic regions [1]. In this manuscript, we will argue that spreading depression propagation can teach us how the brain works, in the sense of linking electrochemical dynamical patterns to perceptual correlates. Furthermore, we will argue that wave propagation can be explained by the vortex effect.

The spreading depression wave is an emergent property of central gray matter and its existence is demonstrated in all parts of it, from spinal chord to neocortex, for reviews, see [2] [3] [4] [5]. The phenomenon was discovered in 1940 by Aristides Leão, who grasped the implication of his discovery in the understanding of the physiopathology of functional syndromes of the CNS. Lashley, in the same year, predicted such a wave, calculated its propagation velocity and made the same inference about its importance that Leão did. The tittle of his paper says: "Patterns of cerebral integration indicated by the scotomas of migraine" [6]. Therefore, in 1940 it was clear that waves propagated in gray matter and that they had perceptual correlates in the form of distorted perception.

The scotomas of occipital migraines present themselves as bright bars that travel in the visual field followed by a dark spot that grows. The bright part is the front, with a dire price in energy expenditure. For example, there is dissipation of energy in the form of heat and infrared photons liberation [3] [5] [7]. The dark patch is the tissue in absolute refractory state. Like the retinal spreading depression, the action potential is also an excitation wave, has excited and refractory states and expends energy [7] [8] [9]. Both have macroscopic spatial scales and the difference in temporal scale is irrelevant in the context discussed here.

In this text we will argue that magnetic flow within the brain explains not only spreading depression waves propagation. They could be the key to understand perception.

2. Methods

In order to conclude the key role of the magnetic flow in spreading depression waves propagation, we examined decades of diversified data, such as image processing of intrinsic optical signals [Note 1] (IOS) and extrinsic fluorescence dyes Ca, voltage and pH sensitive. As well as time series displaying the ion activity in the extracellular space of the neuropil (inner plexiform layer) in isolated retinas and compared the same type of results from cerebellum and cortices. Finally, we realized that if the conjecture about the influence of the geometry of the glial network was correct, then, the vortex effect would be seen at the frontwave of spreading depressions in the rat hippocampus in the form of split frequencies typical of Von Karmann street effects [Note 2]. A previous study that examined the ECoG of rat hippocampi and recorded with sampling rates of 700 Hz was examined and the split frequencies (up to 250 Hz) observed during

the energy expenditure typical of spreading depressions wavefronts [10].

3. Experimental Results

3.1. Mass and Charge Flows Associated with Spreading Depression Waves

The experimental results discussed here (most of it) concern data from two models: the isolated chick retina and the *in situ* rat hippocampus. In the vertebrate retina, the Intrinsic Optical Signal (IOS) associated with retinal spreading depression waves (RSDs) is macroscopic [Note 1], making this preparation unique for the observation of its propagation. The most probable patterns are solitary circular waves and logarithm spirals. Circular spirals were rarely seen and stay mostly in place with a little jitter, whereas the logarithm spirals wander around the retina creating another level of abstract patterns (see [11]). Circular, two dimensional propagation can be taken mathematically as a special case of a dynamic spiral pattern propagation.

Figure 1 and **Figure 2** show the birth and propagation of a solitary circular retinal wave. At the inset the figure shows two time series that were recorded simultaneously with the video in the Picture In Picture (PIP) mode. One series records the extracellular potential at the electrode tip, the second the mean bright brightness of a square pixel matrix with 50 μm side length overlaying the electrode tip. This time series shows the optical changes or the Intrinsic Optical Signal (IOS). Note that the field potential leads the IOS in this wave (shown in **Figure 2**). This pattern is frequent; however, also frequent is the simultaneous rise of both signals.

Ten seconds later the wave is a large circle of optical changes, what one sees is the loss of retina transparency and consequent increase in light scatter. **Figure 2** shows how the extracellular drop of potential (by historical convention in electrophysiology, negativity is up and due to autoscaling of the recording system, one sees the time series moving in the downward direction) relates to the optical changes in tissue around the electrode tip. Remembering from the previous figure, the wave propagates at the rate of 45 μm/sec. It exactly at this distance from the electrode tip that the wave changes the extracellular potential. One second later that dV/dt will peak (frames 127 - 129). It is at this time that the dIOS/dt catches up and also peaks.

Figure 1 and **Figure 2** show a circle of increase in light scatter; however, the IOS associated with membrane excitation have light scatter and birefringence variations [9] [12] tightly coupled to ionic activity changes.

The temporal evolution of ionic activity associated with wave propagationresult in time series in most experiments. The following relationship exists among them: the peak of the dV/dt = d[k]/dt = d[Na]/dt whereas d[Ca]/dt begins at the peak of dV/dt (see for example [3] [4] [5] [12] [13]).

The calcium activity variation is tightly coupled to a component of the pH changes. This component happens at the frontwave and has a kinetics of seconds and thus cannot be associated with metabolism. It must be something else. Our

interpretation is that protons and hydronium ions "disappearance" is the result of dissociated water becoming liquid water. Therefore, the pH shift at the front wave, or at least the major part of it.

The dissociated water makes the Exclusion Zone (EZ) at membranes; this state of water is denser than the liquid and has birefringence [14]. Both calcium activity and pH changes were recorded in RSDs as changes in fluorescence images [2] [4] [5] [12]. The novelty here was that wave patches of tissue could lack the ionic change response maintaining the light scatter at 545 nm. A second slow pH change associated with RSDs is metabolic-production and secretion of lactic acid by microglia, the kinetics follow the second optical component of the optical profile of RSDs [2] [5] the time scale is minutes. In summary: the ionic activity changes in the frontwave are all compatible with the proposed charged gel (EZ) changes and that includes the early alkalinization that lacks explanation in the HH membrane model of same data.

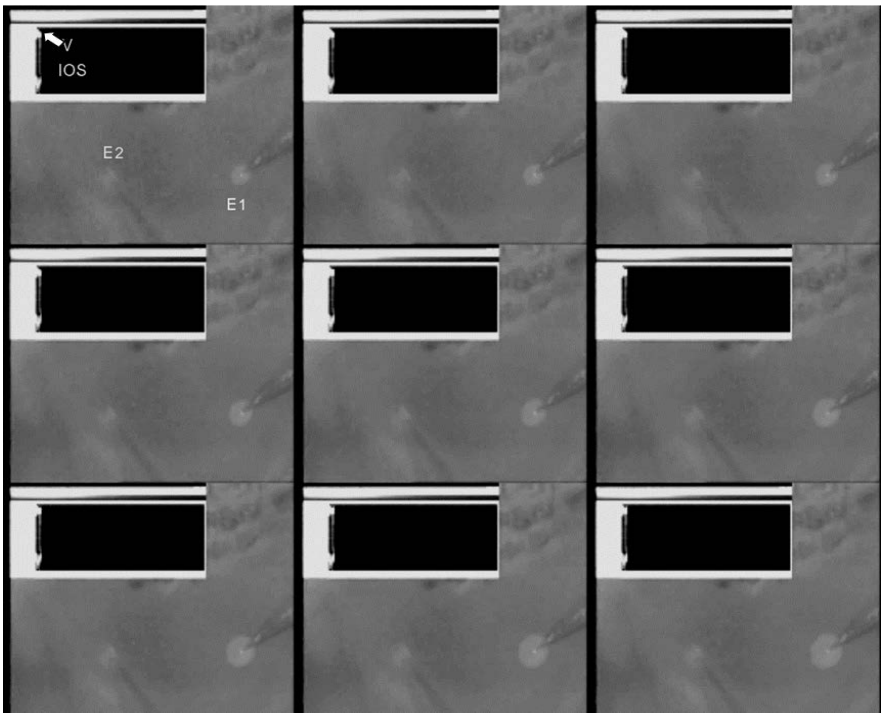

Figure 1. E1 is the stimulating electrode, a glass pipette filled with NaCL. It is positioned very close to the vitreal surface but does not touch it. Rectangular voltage pulses stimulate the tissue and create sharp pulse transients in the PIP time series display. E2 is the recording electrode. It is also a glass pipette filled with KCl solution the electrode tip is inserted in the inner plexiform layer within the extracellular matrix of the tissue. The typical pipettes tips were 20 - 50 μm diameter for both stimulating and recording electrodes. The montage of frames shows the first second of a record. In each row 100 msec in time separates the frames, between columns, 300 msec is the time interval. The inset picture in picture (PIP), shows the two time series recorded simultaneously: above is the extracellular potential labeled V (arrow) in the first frame and below the time series shows the microscale IOS. It shows the average brightness of square pixel matrix about 50 × 50 μm area. The area is above and the closest possible to the recording electrode tip. Note the electrical stimulus artifact in the extracellular potential recording.

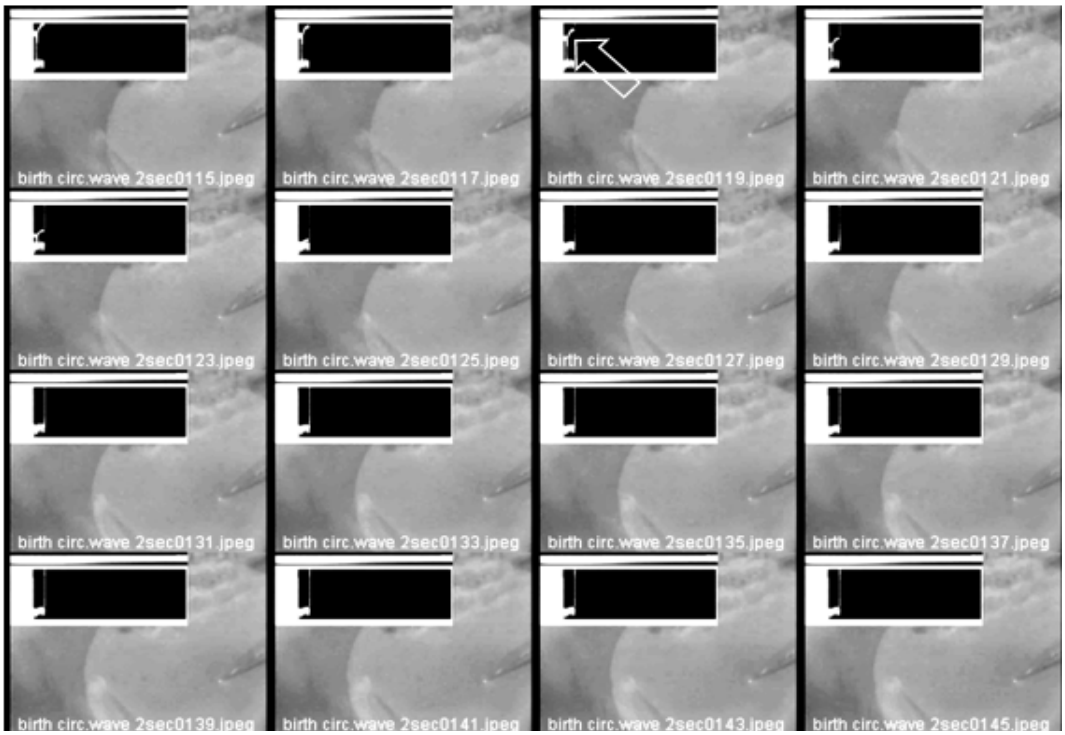

Figure 2. Same experiment showed in the previous figure, 10 seconds propagation later when the circular wave invades the recording electrode sampling space. The time between frames in the same row is 200 msec and 600 msec between columns. The montage shows the recorded time series, extracellular potential [V in previous figure] and the IOS as in the previous figure at their maximum rate of change. Valid for the extracellular potential and optical changes variables due to their tight coupling. **First row**, the near surface stimulating electrode [E1 of previous figure] is to right of the viewer. The inserted recording electrode [E2] on the left. The third frame of the first row, shows the frame when the recording electrode sensed the electromagnetic field of the propagating wave (arrow). Note that the extracellular field potential precedes any changes in the IOS time series. At frame numbered 119 the time series labelled V starts to move with no change in the time series labelled IOS. This displayed pattern is frequent. **Second row**, the wave is close to the tip of the recording electrode. At the second frame the two time series coincide in the display, frame 125. The extracellular voltage drop and the optical changes therefore coincide and grow together. **Third and Fourth rows**, the recording electrode tip is behind the propagating front. The two variables [V and IOS] keep growing together. Due to autoscaling of the display program, the single trace fills the display. The extracellular potential drop is upright because of convention in electrophysiological recordings. Waves recorded in similar experimental contexts, had the peak of potential drop and optical changes 6 - 8 seconds after the initial growth (see [22]). The figure shows the two variables reaching the maximum rate of change. In similar waves, the mean for this maximum is set at 1.8 - 2 seconds after the initial change [22]. The propagation velocity calculated for this wave was 2.7 mm/min, close to the 3 mm/min gran mean across thousands of experiments from several laboratories for temperatures 29 to 32 C.

The kinetics of potassium activity and potential drop are tightly coupled in spreading depression waves; to the point that many researchers attributed entirely to potassium channels activity the potential drop (see for example [13]). Not only that, the potential and ion activity changes have the same signal at both sides of the macroglial membranes. The same is true for the early pH shift, the same alkalinization happens at both sides of glial cells membranes.

The latter variables early pH and potassium activity variables are also tightly coupled to the optical properties changes in chick retinas. In chick retinas in particular a structural feature is of importance: about 2/3 of the length of the Müller cells are divided in fine tubes [5] these tubes have no organelles like mi-

tochondria but are filled with intermediate filaments made of GFAP (Glial Fibrillary Acidic Protein) see also [14]. The telltale part is the acidic mention. In here we assume that around the stack of the acid fibrils, water dissociates and creates and EZ (exclusion zone) [15]. Among the properties of EZs is birefringence. At the quiescence/excited state transition this EZ relaxes and in consequence, the Müller cells lose their lightguide role transiently due to birefringence loss [12] [16] [17] and light scatter increases creating the optical changes or IOS.

In other words, the frontwave releases energy. It does so in several forms of flows, in which water flows are an important part both liquid and dissociated water (for example hydronium ions), free cations and semi mobile anions (radicals in membrane carbohydrates and proteins). The macroscopic circular current that arises at the transition to propagating wave releases red/near infrared light besides heat [8] and when propagation begins green light scatter appears (505 - 540 nm) [5] [12]. We observed this transition many times with voltage sensitive dyes and looking at the Intrinsic Optical Signal (IOS) with infrared and black/white cameras associated with optical filters (see Fig. 9 to Fig. 11 of [5]). We discovered that the red/near infrared scatter followed the potential distribution, therefore a circular linear pattern implies a circular current. When waves were elicited by a light mechanical touch, standing patterns of IOS emerged around the stimulated area and preceded the circular current (see Fig. 17 and Fig. 19 of [2]).

The purpose of **Figure 3** and **Figure 4** is to show how the transition can be followed by observing the tissue IOS.

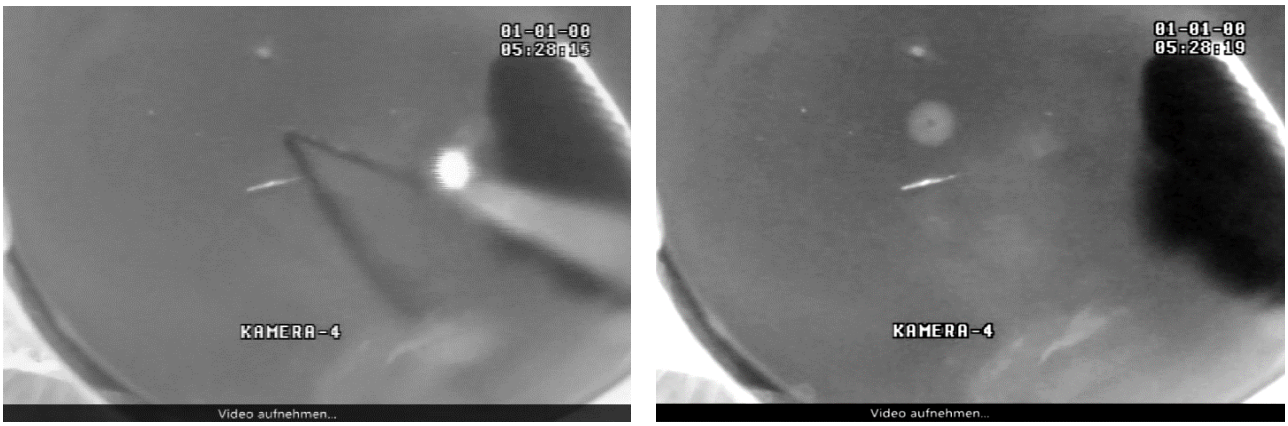

Figure 3. Mechanical stimulation left and circular wave right. Left frame, the frame shows the moment when a tungsten needle (50 μm tip) touches the retinal surface. The eyecup was cut at the equator and glued to a dish. A videocamera records from above. The large structure in the lower right is the pecten, its foot is continuous with the sclera. The length of the pecten foot shown in the frame is 1.8 mm. The pecten consists of blood vessels covered by pigmented epithelium and thus assumed to transport nutrients for this avascular retina. The stimulus is at central retina in a flat region of the chick retina. Right frame 3 seconds later a perfect circular wave is propagating around the stimulation point. Its diameter is 300 μm. Solitary circular waves like this one are the most probable outcome after stimulation. They will invade the whole of the retina without changing the uniform velocity of spread or the brightness of the IOS even after drastic structural changes in the tissue: in front of the pecten is the optical papilla, the exit of the optical nerve fibres. It is a semi-circular area extending from the tip of the pecten to 250 μm in front of it. At this point the tissue consists of only macroglia (Müller cells) and myelinated axons. This change does not affect propagation velocity of retinal waves or its brightness. Therefore, that macroglia dominates the IOS is a foregone conclusion.

Figure 3 (left frame) shows a mechanical stimulation of central retina using a tungsten needle (50 μm). Pressing a charged (piezoelectric) gel will move charges, therefore, mechanical and electrical stimulation are very similar. The mechanical one has an exact point of stimulation, showed in Figure 3. Close to three seconds later, a full blow, perfectly circular propagating wave is present around the stimulation point. The diameter of this wave is 300 μm. Figure 4(a) to Figure 4(f) follow the transition. In the stimulated region a standing dynamical pattern arises hundreds of milliseconds after the touch. The light scatter associated with it contains only red/near-infrared wavelengths. The dynamic character of the spatial pattern conveyed in shimmering bright points inside it and in lower frequency space/time oscillations of brightness of the whole pattern. When a circle closes, Figure 4(d), the IOS includes the blue/green part of the light scatter appears (peak at 545 nm) and propagation begins, Figure 4(e). Because the red/near-infrared part of the IOS matches the field potential distribution, one can see that a circular current closes and initiates propagation. What was lacking was the semblance of the magnetic field associated with the circular current. To realize that a magnetic torus guided water and ions flow, we had first to make experiments with liquid deuterium [18] [19] and interpret these results in the light of the energy release at the wavefront. Second, we looked for experimental models that studied water release of energy in the form of electromagnetic flows, heat and mechanical flow of water. This model exists and is the subject of study of Elmar C. Fuchs and cols. [20] [Note 3].

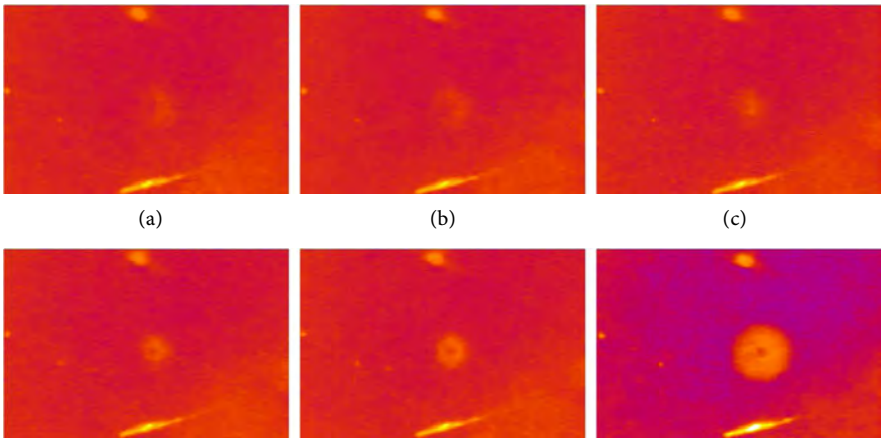

Figure 4. Transition from quiescence to excitation wave seen as changes in the IOS around the stimulated area (previous figure). (a) to (e) have a time interval of 200 msec, frame (f) is the same frame (f) is the same frame shown in the previous Figure 3. The frames adjusted for contrast with Image J software and the display of the 8 bits gray levels is in false colors. (a) to (c) show the standing pattern that precedes propagation. The IOS has only red/near-infrared wavelengths, at (d) a narrow circle closes and at this point, short wavelength components are present. The circle follows the potential distribution or the electrical field, hence a circular current induced; (e) propagation beguis. The illumination in the experiment made with a lamp with a flat emission spectrum between 400 - 600 nm.

First let us examine the liquid deuterium results. We applied liquid deuterium as the solvent in both isolated retinas and Belouzov-Zabotinsky reaction system. As was the case with similar comparative experiments [21] the response of both systems was very similar, both responded with collapse of excitability in a short time (2 hours). The pH of liquid water at 25 degrees Celsius is 7.0, the liquid deuterium pH is 7.4 or deuterium dissociation is five times smaller than that of liquid water dissociation. In our interpretation of the transition from quiescence to propagating wave, these results were not surprising as we first though, but the expected effect of the solvent physical properties changes. It should be noted that the classical HH membrane model does not either predict or explain the solvent deuterium effects, by contrast, Ichiji Tasaki model does [9].

Second, if we examine the flows in a water bridge, at the center, hydronium and hydroxyl ions run toward the cathode and anode electrodes, however twisting around the central current there is mass flow of liquid water and added particles configuring a torus [20]. In water bridges and CNS wavefronts, these charge and mass flows are coupled.

In summary, mechanical stimuli induce a dynamic standing pattern in which fluctuations in release of energy are amplified until a circular current form within the tissue, this current follows the electrical field. In parallel, a magnetic flow guides mass water and particles flow in the shape of a torus. This magnetic torus we propose as a key factor in spreading depression wave propagation.

We also reasoned that time series associated spatial propagation patterns in other parts of the CNS, had to be compatible with such patterns if our conjecture was correct, (see [22]). It was fortunate that in one study of propagation of spreading depression and after discharges, the sampling rate was 700 Hz, very unusual in ECoG recordings [10]. The geometry of the macroglial network in rat hippocampus is cylindrical and that is important. Here we assume that our interpretation about the role of the geometry of the macroglial network in the shape of spreading depression waves is correct [22]. Cylindrical geometry (think of windsocks in small airports) implies Von Karmann Street vortices, they in turn assumed to optimize the energy expenditure within the cylinder. If one measures this pattern in several points in the form of time series, then a split in frequencies should be present. Reexamining the data from the ECoG study [10] at the transition from after discharge to spreading depression, we found the pattern compatible with the expected frequency split of cylindrical geometry vortices. Our conjectures stand.

A further validation can look at vortices presence in excitable tissue and other electrochemical systems such as the B-Z system. Yes, vortices were found in heart tissue and B-Z [23] [24]. Besides these results, another set of experiments suggests vortex effects, non-stationary pathways in B-Z [25] and in isolated retinas [26]. In retinas, the sudden (step) change in potassium activity in the maintenance solutions from 6 to 1or 0 mEq/l, produces a hyper excitable pathway with a succession of spreading depression waves that terminate in tissue death in

about 30 minutes. These waves have altered IOSs. Last, but not least, the alteration of the isolated retinal solution by addition of the liquid glycerol adds viscosity and polarity to the retinal bath solution. The spread velocity, field potential and the IOS observed in the presence of glycerol differed from controls. The red/near infrared light scatter was present whereas the green component was depressed, the spread velocity was slower and voltage record changed kinetics with a prolonged plateau (see [4] [5] [12]). Once more, the electric equivalent model and molecular biology do not predict or explain these results. By contrast, interference with flows do.

3.2. Perceptual and Cognitive Correlates of Spreading Depression Waves

Lashley [6] used the scotomas (bright columns) march through his visual field to predict spreading depression waves as we said in the introduction section. Therefore, the knowledge that the frontwave distorts perception is as old as the wave discovery. Also it is long known that these wave have cognitive consequences in the form of learning and memory mechanisms blockage (for review see Bures, J.1974 [27] Sparks and Gallo, M. 2007 [28]); Bures and Buresova, 1963 [29]; Travis, R.P. and Sparks, D.L. 1963 [30]).

These cognitive impairments occur with structural reversible changes in the gels associated with membranes and energy expenditure in the form of heat and red/near infrared non-Plank dissipation, mass and charge flow. One question arises: is this the maximum rate of dissipation possible? Several sets of data about cortical and retinal waves appear to support that, indeed, this is the case. In the first 10 - 12 seconds of a wave one cannot distinguish between a reversible excitation wave and a non-reversible pathway to tissue death; see, for example [31]; later on, the pattern of spread and the irreversible character of an excitotoxic response makes them clearly distinct. The initial state of several pathways appears the same and thus, vortex effects will explain them all: the magnetic flow guides the mass (carried by liquid water) and charge flows.

Another question emerges: can resonances in the form of eddies of similar flows or Von Karmann street explain a perceptual phenomenon like the epiphanies?

Epiphanies with visualization of problems solutions exist in science. Famous are the ones related by August Kekule and the benzene ring and what Roger Penrose told about visualizing quasi-crystals before chemistry was aware of them [32]. What characterizes these perceptual states are the strong positive emotion (elation) and a strong memory trace let for recall, in contrast with the memory loss associated with the state at the frontwave of spreading depression waves. Here we speculate that an unusual resonant state could be present in the brain during the few seconds long insight period. The spatial shape of the resonances varying in different parts of the brain. The tubular spinal chord and brainstem candidates for Von Karman Street pattern.

Vortex effects appear to be the nature way of maximizing energy expenditure;

their expression present in weather phenomena like tropical storms and hurricanes. Storms can stay put or drift slowly, whereas hurricanes do travel, albeit with different velocities depending on many factors, among which the temperature gradient. The same mechanisms for energy expenditure are present in both phenomena. In the cylindrical rat hipocampus, we found the predicted frequencies split at the frontwaves of spreading depressions [10] [33], either this is a happy coincidence or vortex effects are indeed present in the brain.

4. Conclusions

Eighty years ago, Lashley and Leão inferred and discovered the spreading depression wave, a cortical excitation/inhibition that propagates at mm/min rate. What key factor rules spreading depression propagation remained an unsolved problem.

The visualization of the potential distribution at the quiescence/propagation transition in isolated retinas, led to a deduced circular current around the palisade formed by the glial network. We propose a torus of magnetic flow coupled to the circular current. This torus guides mass and charge transfer *i.e.* water and ions flows from excited to quiescent tissue recruiting new elements of membranes in the frontwave. At the back, the inverted flow is an important part of the absolute inhibition phase of the temporal evolution of tissue states: quiescent, excited, inhibited absolute, inhibited relative, quiescent.

A conjecture is only as good as its integrative power in explaining phenomena believed to be apart. Another aspect is its usefulness and this one can add new aspects to image interpretation in neurology and it will provide help in the interpretation of non-invasive magnetic brain stimulation effects.

Acknowledgments

Frank van den Bovenkamp for discussion in Research Gate, and Wolfgang Hanke for 30 years of friendship and partnership in the adventure of Science (VMFL), FAPESP (APJ).

Conflicts of Interest

The authors declare no conflicts of interest regarding the publication of this paper.

References

[1] Piralishvili, S.A. (2020) Vortex Effect: A History of Its Development in the USSR and Russia. *AIP Conference Proceedings*, **2211**, Article ID: 020004. https://doi.org/10.1063/5.0001006

[2] Fernandes de Lima, V.M. and Hanke, W. (2014) Relevance of Excitable Media Theory and Retinal Spreading Depression in Pre-Clinical Pharmacological Research. *Current Neuropharmacology*, **12**, 413-433. https://doi.org/10.2174/1570159X12666140630190800

[3] Fernandes de Lima, V.M. and Pereira Jr., A. (2016) The Plastic Glial-Synaptic Dy-

namics within the Neuropil: A Self-Organizing System Composed of Polyelectrolytes in Phase Transitions. *Neural Plasticity*, **2016**, Article ID: 7192427. https://doi.org/10.1155/2016/7192427

[4] Fernandes de Lima, V.M., Goldermann, M. and Hanke, W. (1999) The Retinal Spreading Depression. Shaker Verlag, Aachen, 209 p.

[5] Fernandes de Lima, V.M. and Hanke, W. (1997) Excitation Waves in Central Gray Matter: The Retinal Spreading Depression. *Progress in Retinal and Eye Research*, **16**, 657-690. https://doi.org/10.1016/S1350-9462(96)00038-9

[6] Lashley, K.S. (1941) Patterns of Cerebral Integration Indicated by the Scotomas of Migraine. *Archives of Neurology & Psychiatry*, **177**, 199-210.

[7] Tasaki, I. and Byrne, P.M. (1991) Heat Production Associated with Spreading Depression in the Amphibian Retina. *Biochemical and Biophysical Research Communications*, **174**, 293-297. https://doi.org/10.1016/0006-291X(91)90519-D

[8] Tasaki, I. and Byrne, P.M. (1992) Heat Production Associated with a Propagated Impulse in Bullfrog Myelinated Nerve Fibers. *The Japanese Journal of Physiology*, **42**, 805-813. https://doi.org/10.2170/jjphysiol.42.805

[9] Tasaki, I. (2008) On the Reversible Abrupt Structural Changes in Nerve Fibers Underlying Their Excitation and Conduction Processes. In: Pollack, G., Ed., *Phase Transitions in Cell Biology*, Springer Science Business Media, Berlin, 1-21. https://doi.org/10.1007/978-1-4020-8651-9_1

[10] Fernandes de Lima, V.M., Pijn, J.P., Felipe, C. and Lopes da Silva, F. (1990) The Role of Hippocampal Commissures in the Interhemispheric Transfer of Epileptiform after Discharges in the Rat: A Study Using Linear and Non-Linear Regression Analysis. *EEG and Clinical Neurophysiology*, **76**, 520-539. https://doi.org/10.1016/0013-4694(90)90003-3

[11] Dahlem, M. and Müller, S. (1997) Self-Induced Splitting of Spiral-Shaped Spreading Depression Waves in Chicken Retina. *Experimental Brain Research*, **115**, 319-324. https://doi.org/10.1007/PL00005700

[12] Fernandes de Lima, V.M. and Hanke, W. (2020) Reversibility of Excitation Waves in Brain and Heart and the Energy of Interfacial Water. Can Reversibility Be Explained by It? *Progress in Biophysics and Molecular Biology*.

[13] Nicholson, C. (1984) Comparative Neurophysiology of Spreading Depression in the Cerebellum. *Anais da Academia Brasileira de Ciências*, **56**, 481-494.

[14] Khmelinskii, I., Golubeva, T., Korneeva, E., Ynyushin, M., Zueva, L. and Makarov, V. (2017) Spectral Selectivity Model for Light Transmission by the Intermediate Filaments in Müller Cells. *Journal of Photochemistry and Photobiology B: Biology*, **173**, 282-290. https://doi.org/10.1016/j.jphotobiol.2017.06.001

[15] Bunkin, N., Gorelik, V.S., Koslov, V., Shkirin, A. and Suyazov, N.V. (2014) Colloidal Crystal Formation at the "Nafion-Water" Interface. *The Journal of Physical Chemistry B*, **118**, 3372-3377. https://doi.org/10.1021/jp4100729

[16] Franze, K., Groshe, J., Skatchkov, S.N., Shinkinger, S., Foja, C., Skild, D., Ukermann, O., Travis, K., Reichenbach, A. and Guck (2007) Müller Cells Are Living Optical Fibers in the Vertebrate Retina. *PNAS*, **194**, 8287-8292. https://doi.org/10.1073/pnas.0611180104

[17] Reichenbach, A. and Bringmann, A. (2010) Müller Cells in the Healthy and Diseaded Retina. Springer, New York, 91-97.

[18] Fernandes de Lima, V.M. and Hanke, W. (2011) Modulation of CNS Excitability by Water Movement. The D2O Effects on the Non-Linear Neuron-Glial Dynamics.

Journal of Bio-Physical Chemistry, **2**, 253-260.

[19] Klink, O., Hanke, W., Gerbershagen, E. and Fernandes de Lima, V.M. (2010) Influence of Heavy Water in the Belouzov-Zabotinsky Reaction. In: Petrin, A., Ed., *Wave Propagation in Materials for Modern Applications*, INTECH, Rijeka, 400-418.

[20] Fuchs, E.C., Agostinho, L.L.F., Eisenhut, M. and Woisetschlager, J. (2010) Mass and Charge Transfer within a Floating Water Bridge. *Proceedings of SPIE Laser Applications in Life Sciences*, Vol. 7376, 73761E. https://doi.org/10.1117/12.868994

[21] Hanke, W., Wiedemann, M. and Fernandes de Lima, V.M. (2002) Control of Excitability of Neuronal Tissue by Weak External Forces. *Faraday Discussions*, **120**, 237-248. https://doi.org/10.1039/b102706a

[22] Fernandes de Lima, V.M., Piqueira, J.R.C. and Hanke, W. (2014) The Tight Coupling and Non-Linear Relationship between the Macroscopic Electrical and Optical Concomitants of Electrochemical CNS Waves Reflect the Non-Linear Dynamics of Neural-Glial Propagation. *Open Journal of Biophysics*, **5**, Article ID: 51357. https://doi.org/10.4236/ojbiphy.2015.51001

[23] Cabo, C., Pertsov, A.M., Davidenko, J.M., Baxter, W.T., Gray, R.A. and Jalife, J. (1996) Vortex Shedding as a Precursor of Turbulent Electrical Activity in Cardiac Muscle. *Biophysical Journal*, **70**, 1105-1111. https://doi.org/10.1016/S0006-3495(96)79691-1

[24] Ginn, B.T. and Steinbock, O. (2005) Front Aggregation in Multiarmed Excitation Vortices. *Physical Review E*, **72**, Article ID: 046109. https://doi.org/10.1103/PhysRevE.72.046109

[25] Hanke, W. (1999) Inverse Dispersion Relation of B-Z Waves in Nonstationary Gels. *International Journal of Bifurcation and Chaos*, **9**, 2099-2104. https://doi.org/10.1142/S021812749900153X

[26] Dahlem, Y.A., Dahlem, M.A., Mair, T., Braun, K. and Müller, S.C. (2003) Extracellular Potassium Alters Frequency and Profile of Retinal Spreading Depression Waves. *Experimental Brain Research*, **152**, 221-228. https://doi.org/10.1007/s00221-003-1545-y

[27] Bures, J., Buresova, E. and Krivanek, J. (1974) The Mechanism and Applications of Leão's Spreading Depression of Electroencephalographic Activity. Academic Press, Cambridge.

[28] Gallo, M. (2007) Reversible Inactivation of Brain Circuits in Learning and Memory Research. In: Bermúdez-Rattoni, F., Ed., *Neural Plasticity and Memory: From Genes to Brain Imaging*, CRC Press/Taylor & Francis, Boca Raton, Chapter 8. http://www.ncbi.nlm.nih.gov/books/NBK3922 https://doi.org/10.1201/9781420008418.ch8

[29] Bures, J. and Buresova, O. (1963) Cortical Spreading Depression as a Memory Disturbing Factor. *Journal of Comparative and Physiological Psychology*, **56**, 268-272.

[30] Travis, R.P. and Sparks, D.L. (1963) The Influence of Unilateral and Bilateral Spreading Depression during a Learning upon Subsequent Relearning. *Journal of Comparative and Physiological Psychology*, **56**, 56-59. https://doi.org/10.1037/h0043538

[31] Fernandes de Lima, V.M. and Hanke, W. (2012) The Kinetics of Non-Synaptically Triggered Acute Excitotoxic Responses in the Central Nervous System Observed Using Intrinsic Optical Signals. *CNS and Neurological Disorders—Drug Targets*, **11**, 132-141. https://doi.org/10.2174/187152712800269704

[32] Penrose, R. (1991) The Emperor's New Mind. Penguim Books, New York, 435-437.

[33] Pijn, J.P., Vijn, P., Lopes da Silva, F. and Fernandes de Lima, V.M. (1989) Evolution of Interactions between Brain Structures during an Epileptic Seizure in a Kindled Rat. *EEG and Clinical Neurophysiology*, **73**, 172-178. https://doi.org/10.1016/0013-4694(89)90198-3

Notes

1) The IOS in the vertebrate retina is more than 90% of glial membrane activity; in the Gallus gender it is 98% or more. First, it is a vascular and there is no influence of blood vessels in the IOS. Besides the palisade architecture common to all vertebrate Müller cells, in the chick the cell body is divided in fine tubes (8 - 14) filled with closed apposed strands of Glial Fibrillary Acidic Protein (GFAP) in the inner retina (inner plexiform layer, ganglion cell layer and inner limiting membrane) each tube terminated with one end feet [5]. There are no organelles inside these tubes like mitochondria. At the external leaflet, the glial membrane has the EZ of the glycocalix, and at the internal leaflet, the EZ around the GFAP filaments; this EZ fills completely the filaments. Optically, the EZ behaviour is that of a quasi-liquid crystal with birefringence. [10] [12] and physiologically, each tube acts as light guide, the shape of the end feet acts as lens and the EZ a light channel. The current of an approaching wave will flow in the extracellular space above the end feet and around the cell bodies of the glia. The depolarization of the membrane relaxes the EZs at both sides and the cells loose transparency, increasing light scatter concomitant with loss of birefringence. Note that although tightly coupled, the two macroscopic variables are not causally related.

2) For the reader outside biology, a very good analogy of the rat hippocampus is a cashew nut. The head is the dorsal hippocampus and the smaller tail the ventral one. Each mammal has two hippocampi, in the rat the two dorsal heads are close and get apart so that the ventral end is well separated in the rat brain. If one cut the cashew in the frontal plane, what is seen is again two cylinders imbricated one called CA1/CA3 regions and the other Fascia Dentata. No wonder, therefore, that the cylindrical topology dominates the propagation pattern of seizures and spreading depressions. In the hippocampus as well as in the neocortex, the following rule of thumb applies: excitatory input for afar uses acetylcholine (Ach) as chemical mediator and the local circuit and association fibres use glutamate/aspartate and GABA as mediators. The faraway input of the hippocampi is from the septal area and the association input travels in the dorsal and ventral commissures.

3) Elmar C. Fuchs is the rediscoverer of the water bridge and studied in detail this dynamic structure both from experimental and theoretical treatment. The video recordings can be accessed from his homepage: ECFUCHS.com. Infrared cameras documented the torus flow of micro spheres around the bridge, exactly what one expected from the Vortex effect in one-dimensional systems. We quote "The water with Rhodamine B rapidly moved through the bridge, curling close underneath the water surface towards the cathode." … "When tracer particles were added for flow measurements using a laser Doppler anemometer and for visualization, the floating water bridge revealed a rotating outer layer," Woisetschlager et cols., Experiments in a floating water bridge (2010) experiments in fluids, 48: 121-131.

Scientific Research Publishing

Open Journal of Biophysics, 2021, 11, 147-158
https://www.scirp.org/journal/ojbiphy
ISSN Online: 2164-5396
ISSN Print: 2164-5388

Survival at Tumor Recurrence in Soft Matter

Irina Trifonova[1], Galina Kurteva[1], Stefan Z. Stefanov[2]

[1]Specialized Hospital for Active Treatment in Oncology, Sofia, Bulgaria
[2]ESO EAD, Sofia, Bulgaria
Email: itrifa@abv.bg, dr.kurteva@gmail.com, stefanovsz@abv.bg

How to cite this paper: Trifonova, I., Kurteva, G. and Stefanov, S.Z. (2021) Survival at Tumor Recurrence in Soft Matter. *Open Journal of Biophysics*, **11**, 147-158.
https://doi.org/10.4236/ojbiphy.2021.112004

Received: January 9, 2021
Accepted: March 2, 2021
Published: March 5, 2021

Abstract

Survival at tumor recurrence in soft matter, after chemotherapy, is assessed by RNA folding. It is shown that this recurrence is starting with development of a fluidlike globule; it changes the energy of soft matter; it proceeds as a resonant mixing; and at the end it causes diffusion. This diffusion is interpreted as metastasis in soft matter. A tumor memory is designed for its recurrence oscillations. These oscillations are marked as positive or negative according to their influence on life stabilization or destabilization. It is demonstrated that a tumor memorizes two types of recurrences. The intensity of chemotherapy in soft matter for a tumor with such memory is obtained. Survival at tumor recurrence in soft matter, after chemotherapy, is assigned to one of the five regions of the phase diagram of the "thermalized" tumor by microenvironment. To each of these regions is collated a breast cancer survival class. It is found that the survival at tumor recurrence in soft matter, after chemotherapy, well represents actual survival of 32 patients with breast cancer.

Keywords

Survival, Tumor Recurrence, Life Stabilization, Chemotherapy, Soft Matter

1. Introduction

Macromolecules are influenced by different long-distance fields of nature, such as gravity and electromagnetism, in addition to the intrinsic vibratory states of macromolecules that locally generate coherent excitations in the cell [1] [2] [3]. DNA and protein folding, in a biological evolutionary context, may be guided [2] by a set of discrete electromagnetic frequency bands that either promote or inhibit carcinogenesis. Therefore, the tumor recurrence, after chemotherapy, can be considered as evolution of gravitating quantum matter and represents tumor recurrence in soft matter. This is system's oncology consideration [4] [5] of tumor recurrence, after chemotherapy.

Survival at tumor recurrence, in soft matter, for the above embedding of DNA and proteins in integral cellular context, after tumor chemotherapy, is investigated in this paper. That's why the tumor recurrence in soft matter will be studied using the transition [6] from unfolded state into a folded state of the human telomerase RNA pseudoknot upon a jump in the ion concentration (ion-jump) and temperature-quench. In addition, chemotherapy is defined as a probability of success, transferred chemical energy and restoration time.

2. Folding State

Folding state of human telomerase is [6] like a low-energy fluidlike globule. Let the folding state is a fluidlike globule, which is a protein aggregation with fission.

The process [7] of protein aggregation with fission is with Weibull-type limiting distribution. Then the probability of such a protein cluster p_a is found from the probability of chemotherapy success p_s according to graphic by Jo *et al.* [7], when the Weibull-type distribution modules, defining this probability, are equal. The probability for a fluidlike globule occurrence is the probability for occurrence of such a protein cluster p_a.

Let δ_{ex} is the difference of the protein cluster probability p_a and the chemotherapy success probability p_s, $\delta_{ex} = p_a - p_s$. The time to reach the folding state, which is a fluidlike globule at tumor recurrence, τ_{ex} is obtained for the difference δ_{ex}, considered as open system quasiprobability [8] of single qubit in quantum non-demolition noise. Time τ_{ex} is obtained from the graphic in Thapliyal *et al.* [8] of the quasiprobability distribution that is a shifted P-function for a temperature, equals to one. Here the P-function is shifted so that its value to be zero in the initial moment.

3. Folding Kinetics

The human telomerase reaches [6] a folded state through a small number of connected clusters that are repeatedly visited during a pulse sequence in which the folding or unfolding is interrupted. These clusters are hidden states of RNA folding kinetics [6]. This folding kinetics is [6] with two sparsely kinetically connected channels that carry the flux to the folded state. Let the conformation of this two sparsely kinetically connected channels is the knot "Figure-Eight". Then the tumor recurrence in soft matter is characterized by the actual amplitude, connected [9] to Jones polynomial for the knot "Figure-Eight". This actual amplitude is found for the difference of the phase shift θ, after the chemotherapy, of the state in soft matter and the phase shift $\pi/4$ of the maximally coherent state, according to the graphic from Schulte-Herbrüggen *et al.* [9]. Here the phase shift θ is obtained [10] from the restoration time τ_r,

$$\theta = \arccos\left(v_r^2\right),\ v_r = 20/\tau_r . \tag{1}$$

In Equation (1) v_r is the recovery speed at chemotherapy in soft matter.

Time for RNA folding upon ion-jump $\tau_{f,1}$ is obtained from the graphic by

Biyun *et al.* [6] for a square root from the above mentioned actual amplitude, taken with a negative sign. Here is assumed that a square root from the above mentioned actual amplitude, taken with a negative sign, gives the fraction of molecules that remain folded upon ion-jump.

Similarly, the time for RNA folding at a temperature-quench $\tau_{f,2}$ is found from the graphic by Biyun *et al.* [6] for a square root from the above mentioned actual amplitude, with a negative sign. Here again is assumed that a square root from the above mentioned actual amplitude, taken with a negative sign, gives the fraction of molecules that remain folded at temperature-quench.

Let δ_f is the time difference for RNA folding at temperature-quench $\tau_{f,2}$ and the time for RNA folding upon ion-jump $\tau_{f,1}$, $\delta_f = \tau_{f,2} - \tau_{f,1}$. This difference is positive because the rate of human telomerase compaction is [6] greater when folding is initiated by ion-jump than by temperature-quench. Then, similarly to the uncertainty principle, the minimal energy change at tumor recurrence in soft matter as a quantum-classic transition δE and the time difference δ_f can be linked like that

$$\delta E = 1/\left(2\pi\delta_f\right). \tag{2}$$

4. Resonant Mixing

Periodically interrupted RNA folding, upon ion-jump and temperature quench, can be considered as a resonance of a relay relaxation oscillator [11], under periodic external forcing due to the presence of stretching and folding action. Here the relay relaxation oscillator consists of relay hysteresis and an integral feedback, where the periodic external forcing is at the input of the integrator.

Let the normalized autonomous period of the considered oscillator σ is equal to the time for quantum-classical transition of the tumor recurrence τ_{ex}, $\sigma = \tau_{ex}$. Here the normalized autonomous period σ is the ratio of the natural half-period of the relay relaxation oscillator and the half-period of the periodic external forcing T.

Let ε is the amplitude of the periodic external forcing, and θ_1 is the phase at the first switching. Then [11], if $\left\{2+(\varepsilon-1)^2/(\varepsilon+1) < \sigma < 2+(\varepsilon-1)^2/2\right\}$ the oscillator is entrapped at the primary harmonic with a period 2T when θ_1 is in the interval $\left[0, 1-2(\sigma-2)/(\varepsilon-1)^2\right]$ or in the interval $\left[(\sigma-2)/(\varepsilon-1), 1\right]$. Here the "oscillator is entrapped" in sense that its initial phase lies in the domain of attraction of the resonance state. This oscillator is [11] in a resonant mixed mode.

Then RNA folding, upon ion-jump and temperature quench, is entrapped by the primary harmonic with a period $2T$, $T = 10$, if σ fulfils the above σ-condition and if the phase shifting θ of the state in soft matter, after chemotherapy, is the phase at the first switching $\left(1-2(\sigma-2)/(\varepsilon_1-1)^2\right)$ or $\left((\sigma-2)/(\varepsilon_2-1)\right)$. In this case, the amplitude of the tumor recurrence is ε,

$$\varepsilon_1 = 1+\left(2(\sigma-2)/(1-\theta)\right)^{1/2},\ \varepsilon_2 = 1+(\sigma-2)/\theta. \tag{3}$$

5. Tumor Recurrence Metastasis

Tumor metastasis is triggering the tumor recurrence in soft matter through resonant mixing for RNA folding upon ion-jump and temperature quench. Let the tumor recurrence is evolution of gravitating quantum matter, proceeding as nonlinear evolution of weakly perturbed anti-de Sitter space. Then [12] the tumor metastasis in soft matter can be observed as the onset of weakly turbulent instabilization under some arbitrarily small generic perturbations. This metastasis gives rise to [12] diffusion of energy from the low frequencies to high frequencies.

It follows [12] that the tumor recurrence, in soft matter, turns into metastasis in the very moment, when the onset of instabilization is observed. That's why the tumor recurrence in soft matter turns into metastasis in the moment t_1, $t_1 = 20/\varepsilon_1^2$, or in the moment t_2, $t_2 = 20/\varepsilon_2^2$.

6. Oscillations at Tumor Recurrence

Let tumor recurrence in soft matter is a quantum-classic transition with an initial state that is a highly quantum state. Then [13] the gravitating quantum matter in such an initial state tends to "decohere" towards the energy eigenstate with the highest energy. This tumor recurrence, in soft matter, grows into tumor metastasis in soft matter from §5.

Then the probability p_1, the state of the gravitating quantum matter in the moment $t_{n,1}$, not to be the same as its initial state, is [13]

$$\begin{aligned} &p_1 = \cos^2\theta \sin^2\left(\omega_{n,c} t_{n,1}\right),\ \omega_{n,c} = \left(2\pi/10\right)\omega_c, \\ &\omega_c = \left(E + \delta E\right)\sin\theta,\ t_{n,1} = 10t_1/\left(2\pi\right). \end{aligned} \tag{4}$$

Probability p_2, the state of the gravitating quantum matter in moment $t_{n,2}$, to be the same as its initial state, is [13]

$$\begin{aligned} &p_2 = 1 - \cos^2\theta \sin^2\left(\omega_{n,c} t_{n,2}\right),\ \omega_{n,c} = \left(2\pi/10\right)\omega_c, \\ &\omega_c = \left(E + \delta E\right)\sin\theta,\ t_{n,2} = 10t_2/\left(2\pi\right). \end{aligned} \tag{5}$$

In Equation (4) and Equation (5) θ is a phase shift from (1), E is the transferred chemical energy during chemotherapy in soft matter and δE is the minimal energy change at the tumor recurrence in soft matter from Equation (2). Here ω_c is the angular frequency of the oscillations of the probabilities from Equation (4) and Equation (5). This angular frequency is normalized so that the frequency $f_{n,c}$, $f_{n,c} = \omega_{n,c}/\left(2\pi\right)$, to be equal to photo reduction with "10" angular frequency ω_c, $f_{n,c} = \omega_c/10$. Simultaneously are normalized times t_1 and t_2, so that the probabilities p_1 and p_2 not to be changed. New times $t_{n,1}$ and $t_{n,2}$ are with the size of the recovery time τ_r.

7. Marker of Life Stabilization

Viability of life systems is affected [1] [2] by electromagnetic frequencies of tissues, cells and biomolecules, in the range from one-tenth of Hertz till Peta Hertz.

Stabilizing (beneficial) and destabilizing (detrimental) frequencies show repeated patterns of twelve bands and are positioned on two 12-number scales. These two scales, correspondingly, are a coherent scale for electromagnetic frequencies in Hertz (256.00, 269.70, 288.00, 303.41, 324.00, 341.33, 362.04, 384.00, 404.54, 432.00, 455.12, 486.00) [Hz] and non-coherent scale for electromagnetic frequencies in Hertz (249.41, 262.75, 278.71, 295.60, 313.51, 332.47, 351.54, 372.88, 394.12, 418.06, 443.41, 470.28) [Hz]. These scales and their self-similar extensions form octave hierarchies (Geesink and Meijer, 2018).

The above coherent scale for electromagnetic frequencies can be coarse grained to the following color scale: 1) blue-green (269.70, 288.00, 303.41) [Hz]; 2) green-yellow (455.12, 486.00, 256.00) [Hz]; 3) red (384.00, 404.54, 432.00) [Hz]; 4) violet (324.00, 341.33, 362.04) [Hz]. These four coarse grained colors approximately correspond to the colors of CdSe quantum dots [14] for diagnostics of cancer.

Life stabilization marker at tumor recurrence in soft matter m_s is defined by the frequency f_u, $f_u = 10^3 f_{n,c}$, from the interval diagram of beneficial and detrimental frequencies by Meijer and Geesink [2]. Here $f_{n,c}$ is the frequency from §6. Marker values of m_s are:

1) Positive, when the frequency f_u is the frequency, beneficial for life. This marker value is denoted by (+);

2) Negative, when the frequency f_u is the frequency, detrimental for life. This marker value is denoted by (−);

3) Undefined, when the frequency f_u is out of intervals of the beneficial and detrimental frequencies.

In correspondence with two octave hierarchies, the transition time from metastasis tumor state into protein aggregation state $t_{n,1}$ and the time for remaining into the state of metastasis tumor $t_{n,2}$, are measured in weeks.

8. Minimal Memory for Tumor Recurrence

Let the tumor recurrence in soft matter is near-random stochastic process that governs one-dimensional quantum Ising condensates chain. Each of these condensates plays the role of quantum spin. Here one-dimensional quantum Ising chain is a system of interacting quantum spins subject to the influence of a magnetic field. To this stochastic process corresponds [15] classical ε-machine with two causal states s_0 and s_1 and transition probabilities between them T_{ij}, $i, j = 0, 1$. Here T_{ij} is transition probability for the classical ε-machine of the process in state s_i to output $(-1)^j$ and transition to s_j.

This stochastic process possesses [15] an optimal quantum model with two pure states and maximal fidelity F,

$$F^* = \left(T_{00}T_{10}\right)^{1/2} + \left(T_{01}T_{11}\right)^{1/2}. \tag{6}$$

Two pure states of this quantum model are in one-to-one correspondence with classical causal states. Here the optimal quantum model is optimal over all quantum models.

This optimal quantum model is with a minimal memory, required for tumor recurrence modeling in soft matter. Because this model is quantum, it requires less memory than classical ε-machines.

Let the two casual states of the classical ε-machine of tumor recurrence in soft matter are:

1) Casual state s_0 of metastasis that is a state of protein aggregation at tumor recurrence;

2) Casual state s_1 that is a metastasis tumor state at recurrence tumor.

Let this classical ε-machine is with the following transition probabilities:

1) The probability of transition from the metastasis tumor state into a state of protein aggregation T_{10} is the probability p_1, $T_{10}\left(s_1 \to s_0\right) = p_1$;

2) The probability for remaining in a metastasis tumor state T_{11} is the probability p_2, $T_{11}\left(s_1 \to s_1\right) = p_2$;

3) The probability for transition from protein aggregation state into metastasis tumor state T_{01} is the probability of chemotherapy failure, $T_{01}\left(s_0 \to s_1\right) = 1 - p_s$;

4) The probability for staying in a protein aggregation state T_{00} is the probability for chemotherapy success, $T_{00}\left(s_0 \to s_0\right) = p_s$.

Then maximal fidelity of the tumor recurrence in soft matter is:

$$F^* = \left(p_s p_1\right)^{1/2} + \left(\left(1 - p_s\right) p_2\right)^{1/2}. \tag{7}$$

At such tumor recurrence, the transition from a metastasis tumor state into protein aggregation state takes time $t_{n,1}$ with a probability p_1, and staying in a metastasis tumor state is for time $t_{n,2}$ with probability p_2.

9. Types of Recurrence Development

Let metastasis is triggered by magnetic field of the upper quantum Ising chain, and protein aggregation is characterized by spin-spin correlations of the upper quantum Ising chain with a coupling parameter, equals to one. Then the recurrence development time is:

1) Tumor recurrence, where the metastasis is much weaker than protein aggregation;

2) Tumor recurrence, where the metastasis dominates over protein aggregation.

Statistical complexity of the tumor recurrence, where the metastasis is much weaker than the protein aggregation, is obtained by the graphic [16] for the statistical complexity of a quantum Ising chain with a system magnitude, equals to 9, as a ratio function of the magnetic field strength and the coupling parameter. Statistical complexity of this type recurrence is C_μ, when this ratio is equal to maximal fidelity F^* from Equation (7).

The fidelity F_d of recurrence, where the metastasis dominates over protein aggregation, is found from the graphic [16] for the statistical complexity of a quantum Ising chain as a function of the ratio of magnetic field strength and the coupling parameter, for statistical complexity C_μ.

10. Chemotherapy in Soft Matter

Let the chemotherapy protocol, at tumor recurrence in soft matter, is [17] that changes global properties of the tumor state by flipping a local switch. Here the switching of the local switch is a switching between RNA folding and RNA unfolding. Then the chemotherapy at tumor recurrence in soft matter can be determined as non-equilibrium time evolution after quench in quantum XY fermionic chain. This chemotherapy acts as staggered magnetization.

The intensity of this chemotherapy, at a transition from the metastasis tumor state into protein aggregation state $k_{s,1}$, is found from the graphic [17], as a staggered magnetization $B_1/10$ for a time $t_{n,1}/10$.

The intensity of this chemotherapy, while remaining at a state of the metastasis tumor $k_{s,2}$, is found from the graphic by Fagotti [17] as staggered magnetization $B_2/10$ for a time $t_{n,2}/10$.

When times $t_{n,1}$ and $t_{n,2}$ are less than 18 weeks, the intensity of this chemotherapy is found from the graphic by Fagotti [17] for times $\left(t_{n,1}+21\right)$ and $\left(t_{n,2}+21\right)$, correspondingly.

11. Survival at Tumor Recurrence

Survival at tumor recurrence in soft matter after chemotherapy is determined after interacting of the quantum model with a minimal complexity from §8 with tumor microenvironment. Let the tumor microenvironment "thermalizes" [18] this quantum model. Then survival at tumor recurrence in soft matter can be found from a ground-state phase diagram [18] of the one-dimensional axial next-nearest-neighbor Ising model in a transverse field with a system size, equals to 16. Let this system is with a transverse magnetic field B_x, ferromagnetic nearest-neighbor Ising coupling J_1 and antiferromagnetic next-nearest-neighbor interaction J_2. As well, it is assumed [18], that $J_1 = 1$ as the unit of energy.

Phase diagram [18] of this system is with a form of a fan with five sections. Each of these sections is a phase region, determined by the transverse magnetic field strength and antiferromagnetic next-nearest-neighbor interaction. These regions are:

1) Ferromagnetic phase (F_r);
2) Modulated phase (P_3);
3) Modulated phase (P_2);
4) Floating phase (P_1);
5) <2, 2> antiphase.

Here phase regions are numerated from left to right.

Let strength of a transverse magnetic field of this system is equal to maximum fidelity F^* from Equation (7), for tumor recurrence, where the metastasis is much weaker than the protein aggregation. Then, depending on the chemotherapy intensity, antiferromagnetic next-nearest-neighbor interaction is:

$$J_{2,1}=10k_{s,1}/F^*,\ J_{2,2}=10k_{s,2}/F^*. \tag{8}$$

Let the strength of the transverse magnetic field of this system is equal to fidelity F_d, for tumor recurrence, where the metastasis dominates over the protein aggregation. Then, depending on chemotherapy intensity, antiferromagnetic next-nearest-neighbor interaction is:

$$J_{2,3} = 10k_{s,1}/F_d\,,\ J_{2,4} = 10k_{s,2}/F_d\,. \tag{9}$$

Survival after tumor recurrence is determined according to:

1) Recurrence, where the metastasis is much weaker than protein aggregation. Then the survival region is determined by phase diagram [18], at a system size, equals to 16, for:

a) Transverse magnetic field strength F^* and antiferromagnetic next-nearest-neighbor interaction $J_{2,1}$, at a life stabilization marker $m_s = \{(+), \text{undefined}\}$;

b) Transverse magnetic field strength F^* and antiferromagnetic next-nearest-neighbor interaction $J_{2,2}$, at a life stabilization marker $m_s = \{(-), \text{undefined}\}$.

2) Recurrence development, where the metastasis dominates over protein aggregation. Then the survival region is found by the phase diagram [18], at system size, equals to 16, for:

a) Transverse magnetic field strength F_d and antiferromagnetic next-nearest-neighbor interaction $J_{2,3}$, at life stabilization marker $m_s = \{(+), \text{undefined}\}$;

b) Transverse magnetic field strength F_d and antiferromagnetic next-nearest-neighbor interaction $J_{2,4}$, at life stabilization marker $m_s = \{(-), \text{undefined}\}$.

12. Breast Tumor Survival

Survival for breast cancer patients is found in one of the following five classes:

1) Less than 36 months;

2) Between 36 and 60 months;

3) Between 60 and 90 months;

4) Between 90 and 126 months;

5) More than 126 months.

Let the survival of breast cancer patients corresponds to the survival at tumor recurrence in soft matter. Then for the breast cancer patients' survival can be concluded from the above phase diagram. This assessment can be found when the survival class with one number is compared to a region from the phase diagram with the same number. In this case the survival from tumor recurrence in soft matter is measured in weeks in correspondence with two octave hierarchies from §7.

Survival for breast cancer patients is assessed by making an assumption for the recurrence type; the patient's life stabilization marker is calculated; the chemotherapy for this type of recurrence is obtained; the survival region is determined; the patient's survival is classified in accordance with this region.

13. Results

Database is used for 424 patients with breast cancer, who were under treatment at the Clinic of Chemotherapy, National Oncology Medical Center, Bulgaria,

throughout 2003-2014. From them is randomly selected a group of 32 patients with different TNM staging (T-tumor size, N-lymph node status, M-distant metastasis), histology and imunohistochemic characteristics. For all patients the proliferation index has been tested. Research for gene expression has not been done. Their medical history is retrospectively tracked, their current survival is reported (March 2020) and is investigated a correlation with the standard clinical pathological criteria of risk assessment: TNM staging, histology, tumor differentiation grade, (ER, PR, HER2) receptor status. Patients with soft tissue sarcoma or other carcinomas aren't included in the group.

The probability of success, the transferred chemical energy and the restoration time are obtained from the proliferation index of the particular tumor via chemotherapy model in soft matter by Trifonova *et al.* [19].

Proliferation index (PI) estimates the expected time for tumour doubling. PI is assessed by immunohistochemical staining for detecting the proliferating cell nuclear antigen (PCNA). PCNA is a protein that is involved in DNA replication processes, which is found in the nucleus and is a cofactor of the DNA polymerases δ and ε. For PI reference value is accepted its value in a normal matter of 6%. As well, it is accepted that tumor recurrence, where metastasis is much weaker than protein aggregation, occurs with a proliferation index less than 51.01%.

Chemotherapy success, using the chemotherapy model in soft matter by Trifonova *et al.* [19], is not defined for five patients. These cases remain outside the present studies.

One patient is omitted from the study due to a lack of invasive component in the tumor at the subsequent revision.

The case studies with large discrepancies between the chosen survival class and the actual survival are six. In five of them the prognostic survival is assessed correctly and the discrepancy is due to a lack of disease stage in the model. For one patient with a moderate risk of recurrence and death the prognostic survival is overestimated.

Performed research demonstrates that in 25 cases from a total 26 cases (96.2%) there is a nearly coincidence between the chosen prognostic survival class and the actual survival, as well a correlation with the standard clinical pathological criteria of risk assessment.

Life stabilization at recurrence is undefined in two patients with identical disease stages and proliferation index value PI = 50%. Prognostic survival for these two patients is assessed correctly in the light of new research on the role of the tumor stroma for prognostics at triple negative breast cancer.

14. Conclusions

Survival at tumor recurrence in soft matter, after chemotherapy, is obtained in this paper.

This tumor recurrence is related to RNA folding at ion-jump concentration

and a temperature-quench. Therefore:

1) The folding state is considered as a cluster of aggregating proteins in cell division;

2) The conformation of the folding kinetics' two channels is accepted to be a knot "Figure-eight";

3) The folding is described as resonance of a relay relaxation oscillator, subjected to a periodic external influence of extending and folding forcing;

4) Diffusion at this resonance is determined as metastasis.

For tumor recurrence, in soft matter with the above RNA folding is designed a quantum model, with a minimal complexity:

1) Tumor memory is related to the maximal fidelity of this model;

2) Tumor recurrence oscillations are determined as probabilities' oscillations of this model;

3) Life stabilization marker is introduced, through considering the tumor recurrence oscillations as beneficial or detrimental for life.

From the designed quantum model with a minimal complexity are obtained:

1) Two types of tumor recurrence in soft matter-less widespread and dominant;

2) Chemotherapy intensity that acts as staggered magnetization.

Survival at tumor recurrence in soft matter, after chemotherapy, is determined by:

1) Type of tumor recurrence;

2) Life stabilization at tumor recurrence;

3) Interaction with the tumor microenvironment;

4) Chemotherapy intensity.

This survival is referred to one of the five regions of the ground-state phase diagram of "thermalizing", by the tumor microenvironment, a quantum model with a minimal complexity. To each of these regions is compared a survival class of a breast cancer patient.

It is presented that the survival at tumor recurrence in soft matter, after chemotherapy, provides a good idea of the actual survival of 32 patients with breast cancer.

Conflicts of Interest

The authors declare no conflicts of interest regarding the publication of this paper.

References

[1] Melkikh, A.V. and Meijer, D.K.F. (2018) On a Generalized Levinthal's Paradox: The Role of Long- and Short-Range Interactions in Complex Bio-Molecular Reactions, Including Protein and DNA Folding. *Progress in Biophysics and Molecular Biology*, **132**, 57-79. https://doi.org/10.1016/j.pbiomolbio.2017.09.018

[2] Meijer, D.K.F. and Geesink, H.J.H. (2018) Favourable and Unfavourable EMF Frequency Patterns in Cancer: Perspectives for Improved Therapy and Prevention.

Journal of Cancer Therapy, **9**, 188-230. https://doi.org/10.4236/jct.2018.93019

[3] Geesink, H.J.H. and Meijer, D.K.F. (2018) Mathematical Structure for Electromagnetic Frequencies That May Reflect Pilot Waves of Bohm's Implicative Order. *Journal of Modern Physics*, **9**, 851-897. https://doi.org/10.4236/jmp.2018.95055

[4] Stalidzans, E., *et al.* (2020) Mechanistic Modeling and Multiscale Applications for Precise Medicine: Theory and Practice. *Network and Systems Medicine*, **3**, 36-56. https://doi.org/10.1089/nsm.2020.0002

[5] Chamseddine, I.M. and Rejniak, K.A. (2020) Hybrid Modeling Frameworks of Tumor Development and Treatment. *WIREs Systems Biology and Medicine*, **12**, e1461. https://doi.org/10.1002/wsbm.1461

[6] Biyun, S., Cho, S.S. and Thirumalai, D. (2011) Folding of Human Telomerase RNA Pseudoknot Using Ion-Jump and Temperature-Quench Simulations. *Journal of the American Chemical Society*, **133**, 20634-20643. https://doi.org/10.1021/ja2092823

[7] Jo, J., Fortin, J.Y. and Choi, M.Y. (2011) Weibull-Type Limiting Distribution for Replicative Systems. *Physical Review E*, **83**, Article ID: 031123. https://doi.org/10.1103/PhysRevE.83.031123

[8] Thapliyal, K., Banerjee, S., Pathak, A., Omkar, S. and Ravishankar, V. (2015) Quasiprobability Distributions in Open Quantum Systems: Spin-Qubit Systems. *Annals of Physics*, **362**, 261-286. https://doi.org/10.1016/j.aop.2015.07.029

[9] Schulte-Herbrüggen, T., Marx, R., Fahmy, A., Kauffman, L., Lomonaco, S., Khaneja, N. and Glaser, S.J. (2012) Control Aspects of Quantum Computing Using Pure and Mixed States. *Philosophical Transactions of the Royal Society A*: *Mathematical, Physical and Engineering Sciences*, **370**, 4651-4670. https://doi.org/10.1098/rsta.2011.0513

[10] Chandrashekar, C.M., Banerjee, S. and Srikanth, R. (2010) Relationship between Quantum Walks and Relativistic Quantum Mechanics. *Physical Review A*, **81**, Article ID: 062340. https://doi.org/10.1103/PhysRevA.81.062340

[11] Varigonda, S. and Georgiou, T.T. (2001) Dynamics of Relay Relaxation Oscillators. *IEEE Transactions on Automatic Control*, **46**, 65-77. https://doi.org/10.1109/9.898696

[12] Bizoń, P. and Rostworowski, A. (2011) Weakly Turbulent Instabilization of Anti-de Sitter Spacetime. *Physical Review Letters*, **107**, Article ID: 031102. https://doi.org/10.1103/PhysRevLett.107.031102

[13] Bruschi, D.E. (2018) Work Drives Time Evolution. *Annals of Physics*, **394**, 155-161. https://doi.org/10.1016/j.aop.2018.04.028

[14] Smith, A.M., Dave, S., Nie, S., True, L. and Gao, X. (2006) Multicolor Quantum Dots for Molecular Diagnostics of Cancer. *Expert Review of Molecular Diagnostics*, **6**, 231-244. https://doi.org/10.1586/14737159.6.2.231

[15] Suen, W.Y., Thompson, J., Garner, A.J., Vedral, V. and Gu, M. (2017) The Classical-Quantum Divergence of Complexity in Modeling Spin Chains. *Quantum*, **1**, 25. https://doi.org/10.22331/q-2017-08-11-25

[16] Suen, W.Y., Elliot, T.J., Thompson, J., Garner, A.J.P., Mahoney, J.R., Vedral, V. and Gu, M. (2018) Surveying Structural Complexity in Quantum Many-Body Systems. https://arxiv.org/pdf/1812.09738.pdf

[17] Fagotti, M. (2015) Control of Global Properties in a Closed Many-Body Quantum System by Means of a Local Switch. https://arxiv.org/pdf/1508.04401.pdf

[18] Bonfim, Oz de Alcantara, Boechat, B. and Florencio, J. (2017) Quantum Fidelity Approach to the Ground-State Properties of the One-Dimensional Axial Next-

Nearest-Neighbor Ising Model in a Transverse Field. *Physical Review E*, **96**, Article ID: 042140. https://doi.org/10.1103/PhysRevE.96.042140

[19] Trifonova, I., Kurteva, G. and Stefanov, S.Z. (2014) Success of Chemotherapy in Soft Matter. https://arxiv.org/pdf/1404.0936.pdf

Scientific Research Publishing

Open Journal of Biophysics, 2021, 11, 159-176
https://www.scirp.org/journal/ojbiphy
ISSN Online: 2164-5396
ISSN Print: 2164-5388

A Quantum State Scenario for Biological Self-Replication

Robert Englman

Ariel University, Ariel, Israel
Email: englmanrobert@gmail.com

How to cite this paper: Englman, R. (2021) A Quantum State Scenario for Biological Self-Replication. *Open Journal of Biophysics*, **11**, 159-176.
https://doi.org/10.4236/ojbiphy.2021.112005

Received: January 19, 2021
Accepted: March 8, 2021
Published: March 11, 2021

Abstract

With the prevalent conception of self-replication (SR, a hallmark of living systems) as a non-equilibrium process subject to thermodynamic laws, a complementary approach derives the low energy quantum states arising from a Hamiltonian that appears to be specific for bio-systems by its containing some strongly binding terms. The bindings attract *properties* of the template (T) and the reactants to form a replicate (R). The criterion for SR that emerges from the theory is that second order (bi-linear) interaction terms between degrees of motion of T-R and the thermal bath dominate negatively over a linear self-energy term, and thereby provide a binding between the attributes of T and R. The formalism (reminiscent of the Kramers-Anderson mechanism for superexchange) is from first principles, but hinges on a drastic simplification by modelling the T, R and bath variables on interacting qubits and by congesting the attraction into a single (control) parameter. The development relies on further simplifying features, such as Random Phase Approximations and an Effective Hamiltonian formalism. The entropic balance to replication is considered and found to reside in the far surroundings.

Keywords

Self-Organization, Living Systems, Protein Conformations, Bifurcation, Curie-Weiss Spin Model

1. Introduction

It is remarkable that the concept and process of self-organization feature in so many different major disciplines [1]: in Applied Mathematics (Robotics, pioneered by von Neumann [2] and also [3]), in Physics (by a thermodynamic viewpoint, e.g. [4]) in Chemistry (primarily Organic Chemistry, and specifically Dynamic Combinatorial Chemistry [5] [6] and also in Crystallography) and,

notably, in Biology (e.g., DNA copying as in meiosis, mitosis or binary fission, in cell divisions [7] [8] [9]). With a net so widely spread, it cannot be expected to be doing justice to all the work done heretofore.

While addressing the subject with methods in physics, the inquiry takes us to Biology, and particularly to a specific phenomenon of self-organization, namely, self-replication (SR) [6], existing in a large variety of biological entities and recognized as one of the main marks distinguishing animate from non-animate matter. (Though, there may be rare instances of SR also in the inorganic world, but not as a cyclic process [10], or in auto-catalysis but lacking the specificity of SR [11].) Notably in Biology, SR occurs at enormously differing size scales, ranging from large animals to tiny biomolecules. Accounts of real life and laboratory occurrences of SR can be found in [11] [12], including experiments at synthesising self-replication by Leslie Orgel, Rebek, von Kiedrowski [13] [14] [15] and others, as well as template-guided nonenzymatic SR, the latter also characterizing primordial RNA replication [16]. Past theoretical works, including Stuart Kauffman's set autocatalysis, have been summarized in [17] [18], with a mathematical framework that addressed in particular the citric acid - >CO and the formose (formaldehyde - > sugar) reactions.

We have made it our aim to connect up biological SR with Physics and that at a most basic level. The price that we pay for the temerity of such undertaking is doing the job in an extreme schematic and simplified fashion, thereby producing only a preliminary investigation, to be hopefully followed by further more specific and detailed works.

Remarkably enough, the guiding idea of the present approach (though arrived at independently by us) had already been given expression in a work remote from basic Physics, in a review of Dynamic Combinatorial Chemistry (DCC) dealing with the autonomous formation of receptors, that read: "Addition of a guest (a template molecule in the terminology of the present study, RE), which *binds strongly* (my italics) to one of the libraries (available components, RE) shifts the equilibrium towards its formation (of a new creature or offspring, RE), resulting in the amplification (renewed formation, RE) of the successful receptor at the expense of the less successful" [5]. The italicised words "*binds strongly*" are the leitmotif of the present work, as will be apparent in the sequel. Even more supportive is the concluding sentence of the same reference: "We are confident therefore that DCC will engender generations of ingenious concepts and lead to new, as yet unpredictable theories". Yet closer to the approach here taken is the assertion made about 70 years earlier than that: "The living organism seems to be a macroscopic system which in part of its behaviout approaches to that purely mechanical (as contrasted with thermodyamic) conduct to which all systems tend, as the temperature approaches absolute zero …" ([19], Chapter 6). It seems that we are at liberty, and not in conflict with the author, to qualify "mechanical" by *quantum* mechanical, as will be argued next. Regarding the quantum mode of the formalism, this is analogous to Kramers' and P.W. An-

derson's mechanism for superexchange [20] [21], with the bath replacing the bridging anion and exploitation of the randomness of the former. [Note the "attractive coupling" expression (based there on third order perturbation) of Anderson following his Equation (19) in [21].]

A Quest for a Quantum Description

At the foundation of all forms (situations, states, phenomenologies) and processes (changes, developments, steady existence) that constitute our daily life lies Quantum Mechanics (QM), mostly expressed in some or other form of the Schrödinger equation, erstwhile involving a Hamiltonian and some boundary initial conditions. In most complex issues where the QM path is not feasible, Thermodynamics (Td) or Statistical Mechanics comes to the rescue and one must hope that they (QM and Td) are compatible, as seems to be the case. The merging of the two, essentially in the direction of QM - >Td, has become a major recent objective of research, going under the name of Eigenstate Thermalization Hypothesis [22] [23].

Life (and more precisely, biological processes), though an extraordinary and unique phenomenon, ought not to be an exception to a derivation of its thermodynamics from quantum theory, as has been the case in e.g., light production or lasing. By my understanding, a quantitatively specific description of life starting at the QM level does not exist, not even within the broad insights provided by Schrödinger [19], Bernal [24], Prigogine [25], Dyson [26] and Ruelle [27], among others.

In the following, the subject will be self-replication (SR) in biological systems, a process which is both ubiquitous and perennial. The systems in view range in their shape and size from animals (humans included) through cells to biological micro-molecules; from a Physics viewpoint every single entity in a particular system is characterized by its momentary state, inclusive of its eigen-state, orientation and location. In the following schematic and maximally simplified treatment all these varied systems are represented in one single model and all their properties are subsumed under a single yes-no alternative. (A classical, non-quantal description might lead to qualitatively similar results, but without the sharpness consequent upon quantization, e.g., of spin alignment.) Of late, SR was treated by J. England [28] [29] from a thermodynamic viewpoint. Though Ruelle [30] has formalized that work in a quantum setting, the subject still awaits a microscopic model, like the one proposed here.

The conceptual innovation of this work lies in that, contrasting to the currently prevalent understanding of replicative and other processes in presently existing living systems, as due to the background presence of enzymes that lower and raise barriers to initiate and perpetuate modifications (**Figure 3** in [28] and P. Gaspard's remark in [30]), but whose dynamical variables are absent from the formalism, these are here included in an essential, though only schematic way. It should be emphasized that this work aims at providing a descriptive account of

how SR emerges in a quantum mechanical setting, rather than why the settings occurs in systems that exhibit SR. Specifics are in section 4.1.

The article starts in section 2 with a list of the *dramatic personae* which enumerates the entities that take part in a real self replication event, a list that is followed by another, section 2.1, in which each biological component is schematically represented by a qubit (half-spin). The enumeration of components matches, but is more specific than those described by Ruelle [30]. (e.g., his "X" are here sub-listed as T, R, $L/(T, R)$.) In subsection 3 the present approach is placed in a perspective of standard scenarios of enzymatically activated biologocical activities, pinpointing how the former is complementary to the latter.

The model Hamiltonian is given in section 4, followed by a curt but important derivation of the "control" term in subsection 4.1. The entropic state of the system is given in section 5, both before (subsection 5.1) and at the conclusion (subsection 5.2), of the replication process. The numerical results are displayed in section 6 with the simple **Figure 4**.

As a side line, this work points tentatively, and on the basis of the results, at a partial answer to the quintessential question "what discriminates between animate and non-animate matter?" as contained in section 6.1. (It should be stressed that the criteria derived from this work are not in opposition to general characterisations of life, [19]-[26], but give them here an expression within a basic, Hamiltonian formalism.) Subsection 6.2 elucidates the energy scales used, followed by a Conclusion section 7. The Supplementary Information (SI) informs how the tracing in a highly entangled system is to be performed. The theorems there may have a wide application.

2. The Biological Components

1) The template (T), which duplicates and maintains its state during SR.

2) The library (L) of available molecules, which is composed of

a) the template's counterparts, the reactants (designated $r_1, r_2, \cdots$), *i.e.*, those molecules that are gathered up by T from just anywhere in the library ultimately to be the replicate "R", and

b) those that are unselected, but may play some role (e.g., as enzymes) in SR. These do not replicate (by the "Central Dogma" of biology).

3) The broader environment, which adjusts in the course of replication and constitutes a thermal bath supplying the needed free energy [7].

2.1. Representation

In our formalism, these complex structures are condensed into single qubits (1/2-spins) and their manifold intrinsic characterizations take the simplified form of just two alternatives, "up" and "down". To reproduce the roles that 1) - 3) play in reality, as above, we construct a Hamiltonian in which there are (as "degrees of freedom"):

1) A "template" qubit, whose state-stabilization is ensured by having a self-Hamiltonian of a Zeeman term form $-e_T\sigma_z^T$ with a very large energy pre-factor ($e_T \gg 1$, in our energy units, σ's here and in the sequel being Pauli spin-matrices).

2a) A *single* potential replicate (R) qubit with Zeeman energy ≈ 1, but also having an additional interaction term with the template-qubit of the form $-W\sigma_z^T\sigma_z^R$, in which $W \gg 1$. W serves as the control parameter, or "control" (for brief), in that it regulates the transition across the SR divide. The derivation of W by second order perturbation is the focal point in the theoretical development.

2b) Additional qubits ($N-2$ in number), which, together with the former two, interact through Curie-Weiss type x couplings $\sigma_x^i \cdot \sigma_x^j, (i, j = 1, \cdots, N)$, with varying strengths, all of the order of unity. Their weights in the low-lying wave functions are minimally affected by replication.

3) A thermal bath, in weak interaction with the former, bringing about thermalization and perturbationally enhancing the replication (alignment).

3. Scenarios for SR

This section examines the relation of the present quantum state formalism in an SR process to other scenarios in which SR arises as an enzyme coordinated barrier jumping event. Several theories for barrier jumping in enzymatic actions are described in [31], which also amplifies the common formulation of the process along a single reaction coordinate mode by the addition of a "promoting" vibrational mode to form a two dimensional landscape of the potential energy surface. Interestingly, a "promoting mode" of opposite symmetry to accepting modes entered previously the theory of vibronic (vibrational-electronic) decay in large molecules [32].

The following figure (**Figure 1**) serves to visualise the complementary roles played by the two schemata for SR as transitions between two parabolic Potential Energy Surfaces (PES), whose profiles are drawn along a single reaction coordinate. The simple parabolic depiction of the biological entities does not do justice to the complexity and multiplicity of sub-conformational wells in real systems, but serves as a base. In **Figure 1(a)**, PES are drawn on the left (in black) for the pre-SR configuration, template T and pre-replicated reactants $r_1 + r_2 + \cdots$, and on the right (in red) for the post-SR configuration, template T and the replicate R in which the reactants have merged, with a separation barrier in-between. To initiate a left-to-right transition, the barrier is transiently lowered, shown by the short curly line and a promoting coupling between the configurations (not shown) is brought into play. This summarizes the barrier jumping scenario of SR, in which the quantum states involved both in the ascent to the transition state and in the descent from it are not specified.

In the adjacent **Figure 1(b)**, illustrative of the present, quantum state scheme, PES are plotted, for the situations in which the Hamiltonian is without a control term ($W = 0$, upper drawing) and one with a large control ($\gg 1$, lower drawing).

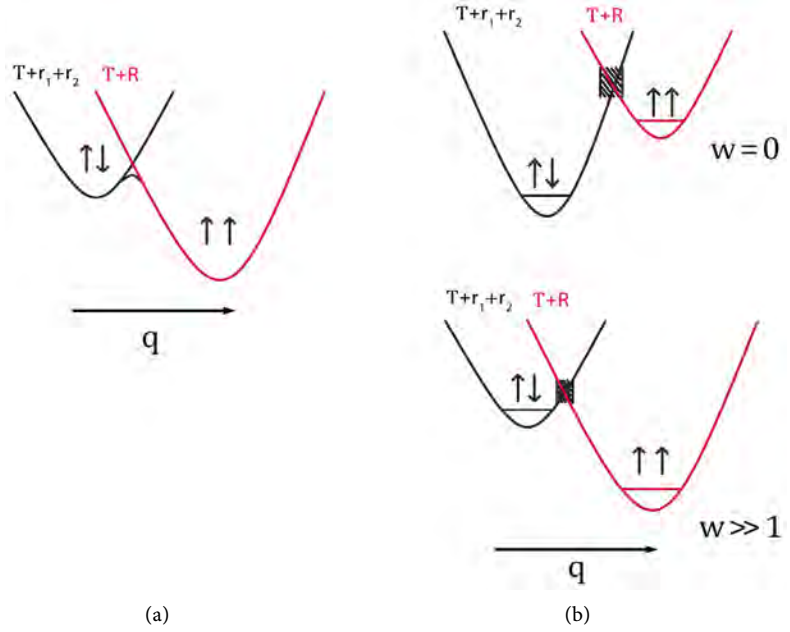

(a) (b)

Figure 1. Alternative scenarios for SR. (a) A barrier jumping mechanism. Potential energy surfaces (PES, in arbitrary units) before self-replication for the molecular components in a $T + r_1 + r_2 + \cdots$ configuration (black) and for the replicated configuration T + R (red) against a reaction coordinate (in arbitrary units). The curved line represents a temporarily lowered barrier, across which the transition takes place. (b) Quantum level formalism. The lowest levels are schematically indicated by short horizontal lines at the nadirs of the lower PES parabolae plotted against a reaction coordinate. The PES drawn by dashed and full lines are for different Hamiltonian ($W = 0$ and $W \gg 1$) and in each case they are shown schematically for the two configurations ($T + r_1 + r_2 + \cdots$ in black and T + R in red). The identification of alignment and anti-alignment in the spin model with the respective red and black PES are shown by vertical arrows. Events in the shaded region are not part of this formalism.

For each Hamiltonian alternative configurations ($T + r_1 + r_2 + \cdots$) and (T + R) exists (and are drawn in their respective colouring, as before), but their low energy states (indicated by the short horizontal curves at the bottoms of the parabolae) change radically. (The two alternative configurations are formalized in our two spin model by $\uparrow\downarrow$ and $\uparrow\uparrow$, respectively, also shown in the drawings.) The source of the energy change is the increase of the control term coefficient W in the Hamiltonian from 0 to a large value. (The physical cause of this change is not clear; it is presumed to have an enzymatic source.) Whereas at low temperatures the resultant configuration is both determined and described by the ground state, the interim quantum states are not part in the theory. Their exclusion from the theory is indicated by the shaded regions in the figure at barrier heights: the events in this region taking place during SR are better viewed within the barrier jumping scenario.

The control W, which is thus the pivotal source of the present complementary scheme, is derived by a straightforward quantum mechanical procedure in subsection 4.1.

4. Formalism

The foregoing processes are entirely rooted in the following Hamiltonian (written in arbitrary energy units)

$$H = H(N) + H_{bath} + \delta H_{N-bath} \tag{1}$$

in which the first term for N interacting spins (described immediately below) is fully treated, the second term, the bath Hamiltonian is not required for our considerations , while the third, interaction term is dealt with perturbationally in the following subsection 4.1. Within this model of N fully interacting 1/2-spins (qubits), the spins labelled $1,\cdots,N-2$ are identified with the background items 2b' in the above enumeration, (these do not replicate and are not directly subject to SR while being part of the "library"); next, a spin labelled $N-1$ which is the template ("T", 1') in the above and, finally, labelled N (and designated "R" for "replicate", 2a') is the spin that is being converted in SR to become the facsimile of the template. (The peculiar ordering of the labels aims at a simplified formulation of the "reservoir tracing", which is the concern of the Supplementary Information.) The following Hamiltonian applies to this spin system:

$$H(N) = -\sum_{i=1,\cdots,N} h_i \sigma_z^i - \sum_{i,j=1,\cdots,N} g_{i,j} \sigma_x^i \sigma_x^j \tag{2}$$

The Zeeman energy parameters differ in their magnitudes, as follows:

$$i = 1,\cdots,N-2 : h_i = O(1);\ i = N-1 : h_T \gg 1;\ \ i = N : h_R = O(1) \tag{3}$$

For the inter-spin coupling we have chosen

$$g_{ij} = O(1)\ \ (i, j = 1,\cdots,N) \tag{4}$$

Further details on the chosen value of the coupling coefficients are found in [33]. These are not here reproduced, as these details are not essential to the following for which the important features in the Hamiltonian are the template binding term $-h_T \sigma_z^T$ and a correction term hereby derived.

Control

For δH_{N-bath} we postulate a bilinear form:

$$\delta H = \sum_b \left(k_{bT} \sigma^b * \sigma^T + k_{bR} \sigma^b * \sigma^R \right) \tag{5}$$

with T and R labelling the template and replicate spin-entities and b indexing the bath qubits. * denotes vectorial inner product. Calculating its perturbational effect on the energy of the *combined* T-R-bath wave-function Ψ, one may assume that due to the random nature of the bath the first order diagonal perturbational correction $\langle \Psi | \delta H | \Psi \rangle$ vanishes. Regarding the second order energy correction, we first of all note that for low lying states the energy correction is predominantly negative. Next we perform a number of manipulations (approximations) that will end up by supplying an addition to the Hamiltonian $H(N)$ above of the form $-W' \sigma_z^T \sigma_z^R$, with W' large and negative.

$$\delta^{(2)} = \Sigma_{exc} \frac{\left|\left\langle \Psi \left| \delta H \right| \Psi_{exc} \right\rangle\right|^2}{E - E_{exc}} \tag{6}$$

$$\approx -\left|\delta E\right|^{-1} \Sigma_{exc} \left(\left\langle \Psi \left| \delta H \right| \Psi_{exc} \right\rangle\right)^2 \tag{7}$$

$$\approx -\left|\delta E\right|^{-1} \left\langle \Psi \left| \left(\delta H\right)^2 \right| \Psi \right\rangle \tag{8}$$

$$\begin{aligned} &= -\left|\delta E\right|^{-1} \Sigma_b \left\langle \left\langle \Psi \right| \left[k_{bT} \sigma^b * \sigma^T \right]^2 + \left[k_{bR} \sigma^b * \sigma^R \right]^2 \right. \\ &\left. + 2 k_{bT} k_{bR} \sigma^b * \sigma^T * \sigma^b * \sigma^R \left| \Psi \right\rangle \right\rangle \end{aligned} \tag{9}$$

In passing from the first to the second line all energy denominators involving excitational energies E_{exc} were approximatively replaced by a constant and negative mean value, thus enabling by the closure property to reach the next stage, in which appears the expectation value of $\left(\delta H\right)^2$. Opening this, we are led to a summation over bath entities *b*. At this stage, cross-terms in the bath indices were deemed to vanish by the randomness of phases in the bath spins. Subsequently, after opening up $\left(\delta H\right)^2$ in line four, the two squared terms contribute only constants to the energy and may be ignored. We are thus left with the cross term coupling target and replicate spins bi-linearly. Assuming identical signs for the coupling coefficients k_{bT} and k_{bR}, each term in the last expectation sum contributes negatively. Adopting the so named "Effective Hamiltonian" procedure in electron spin resonance (ESR) theory, the operator between the bra-kets can be appended to the Hamiltonian $H\left(N\right)$ in Equation (2) as $-W'\sigma_z^T \cdot \sigma_z^R$ with W' given by

$$W' = \frac{2}{\left|\delta E\right|} \Sigma_b k_{bT} k_{bR} > 0 \tag{10}$$

The magnitude of W' is a matter of further investigation and modelling of the bath, but it may be noted that it is a sum of many terms, in principle numbering the molecular contents of the bath. There may be analogous terms, involving *x* and *y*-spin components which are non-diagonal and presumably play a role in the energy exchange between the bath and the T-R system. They have no role in the model.

Summarizing the foregoings, we have identified within the T-R-bath-system Hamiltonian a potential source for the strongly negative bilinear coupling of the form

$$-W\sigma_z^T \cdot \sigma_z^R \tag{11}$$

in which $W = W' + g_{TR}$ is the control parameter for self-replication.

The above approximative procedure of eliminating the bath variables due to their random (and uncorrelated) phases appears to be justified at the present level of treatment, in which the bath degrees of freedom are not dynamic (*i.e.* not subject to equations of motion; alternative justifications rooted in the sheer size of the number of bath coordinates were also given). [In a more elaborate treatment inclusive of bath dynamics the foregoing manipulation of $\left(\delta H\right)^2$

would have been done in reverse: by tracing over the N-variables (the total system *minus* the bath) and obtaining an "Effective Hamiltonian" representing interaction within the bath coordinates, inducing correlations and entropy increase, for which predictions have already been made in [34] [35]. By their estimate, this occurs mainly well after the SR process, thus allowing one to treat the process of SR itself at the level here adopted.]

5. Stages of Replication

In this *conceptual* stages are meant, as in a "gedanken experiment", not chronological ones. For the latter, the states of bifurcation, appearing in **Figure 4** as a diagonal line, may well be relevant, representing states of meta-stability.

5.1. Pre-SR

The control is off, $W = 0$, and the thermalisation with surrounding is as yet absent. So we may take the template spin N to be "up", and the library spins, excepting the potentially replicate spin $N-1$, to be in any arbitrary combination of up and down states. (For simplicity and definiteness we take them all to be in their up states.). The replicate spin is in a mixed state of up and down states, at equal shares. Thus, the whole system is in a mixed state, with a density matrix having 1/2 on the diagonal and 0 on the off-diagonals. The entropy of the whole system excluding the bath is at this stage

$$S_{preSR} = \log 2 \tag{12}$$

5.2. Post-SR

Having turned on the control to its value of W, which in many cases of reality is presumed to be the effect of enzyme activities, the eigenvalues and eigenstates of the whole system are those given by the Schrödinger equation with the Hamiltonian H in section 4. Postulating a thermal bath temperature much lower than the Zeeman energy of the template, when the thermal interaction with bath is turned on, we shall find the system to be in a state in which the template spin is fully up and, with the control W that favours a T-R alignments switched on, the replicate is also oriented towards the up state. Thus in the low lying, occupied states, the replicate abandons (in a statistical sense) the previous mixed state and resides with a probability close to unity in the up state. A precise measure of the probability is the Reduced Density Matrix (RDM) for the TO sub-system, obtained by tracing over the $N-2$ remaining library states. This yields, as the control W is strengthened, values approaching one and zero, respectively, for the probabilities of the pair T-R being in the (*up up*) and (*up down*) states. Since the eigenstates are highly, 2^N-fold entangled, the tracing is not trivial and, in order not to interrupt the description of the results, the derivation of the RDM matrix-elements $\rho_{up\,up,up\,up}(\approx 1)$, $\rho_{up\,down\;up\,down}(\approx 0)$, $\rho_{up\,up,up\,down}(=0)$, $\rho_{down\,up,up\,down}(=0)$ is explained in the supplementary information (SI). Its theorems may have wider applications outside the present spin manifold.

It needs to be stressed that the "alignment" found by the spin-formalism does not proxy for orientational alignment or spatial contiguity, but only a correspondence in the (two-dimensional) Hilbert spaces of the spins. Thus, the two organs represented by T and R may be spatially quite detached from each other and be reacting independently for any eventual external stimulations. Such reactions are outside the scope of this paper.

Observationally more accessible than the probabilities is the entropy (here, the post-SR reduced entropy of the TR sub-system and denoted by S), since the entropy *reduction* in TO must be compensated over by an increase of entropy in the surrounding, which is manifest by its heat gain. Essentially, this is the basis of the "Theory of Dissipative Structures" propounded by Prigogine [25], elsewhere expressed by the requirement that for the functioning of living systems free energy must be externally supplied to them [19] [26].

In the following plot (**Figure 2**) we plot the post-SR entropy for the TR sub-system (full lines). To obtain this, we first calculate the reduced occupation probabilities RP_i of the four possibilities ($i = \uparrow\uparrow, \uparrow\downarrow, \downarrow\uparrow, \downarrow\downarrow$) for the TR spins by tracing the computed occupation probabilities over the states of the other spin probabilities and then calculate the entropy as,

$$S, entropy = -\sum_{i=1,2,3,4} RP_i \log RP_i \tag{13}$$

From the figure it is apparent that as the control W increases the TR entropy decreases, approaching the $S = 0$ limit appropriate to a pure state (that of thermodynamically full alignment) for large W. Following Nigmatullin and Prokopenko [4] we next compute a quantity, there named "Efficiency", η of the SR as the change of entropy relative to the change of control. With our dimensionless parameters this reads as

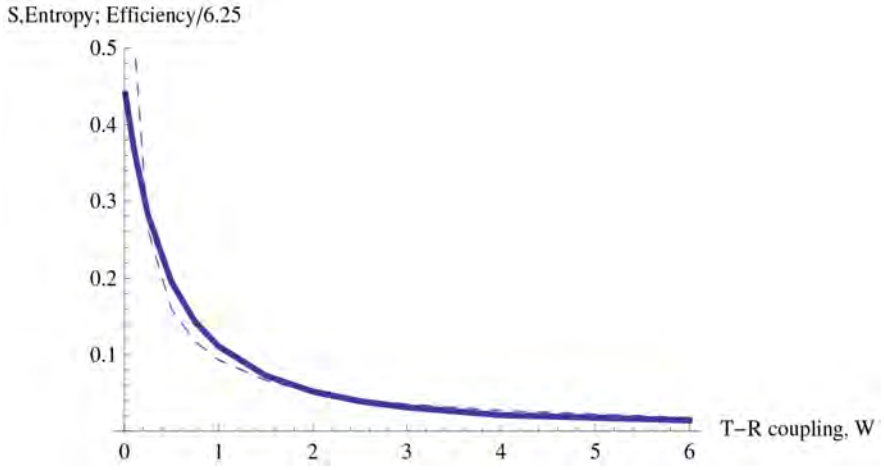

Figure 2. Full line: Post-SR reduced entropy S of the aligned template-replicate spin-pair, as function of the alignment-inducing coupling strength (W, energy units). The asymptotic $S = 0$ signifies full alignment (both spins up). Other parameters as in the text; the curve is insensitive to variations in the large value of the template stabilization constant $h_T > 6$. Broken line: Efficiency (defined in the text Equation (14), downscaled by 6.25).

$$\eta = \frac{S_{preSR} - S}{W} \tag{14}$$

In the figure the efficiency (drawn by broken lines) is plotted; however it is downscaled by a factor of 0.16, and this so as to bring it into (near) coincidence with the entropy S plotted by full lines. Postulating an exact coincidence for lrge values of W (which are here of interest), one arrives at the following empirical relation for the post-SR entropy:

$$S = S_{preSR} / (1 + 6.25W) \tag{15}$$

The generality of this relation is not obvious, but it represents a predictive achievement of the theory, to be tested experimentally. The terms "Efficiency" and "work" are used here due to their previous usage in [4], but in the present context they do not have the usual connotations. (Thus, here the "Efficiency" may exceed 1.)

The decrease of T-R entropy, signifying an enhancement of order must be balanced by an increase of entropy exterior to T-R, as required by general thermodynamic principles and ingrained in Prigogine's theory of "dissipative structures". Where does this increase occur? Remarkably, not in the rest of the spin-library, but outside it, in the thermal bath, in line with the general considerations of [34] [35]. This result is shown in the adjacent **Figure 3**, in which a slow but steady *decrease* of the combined reduced entropy of the exterior library spins is evident.

6. Replicativity

The numerical interplay between the control parameter W of the bilinear T-R term and the "binding energy", linear, Zeeman term strength parameter h_R of the replicate is displayed in **Figure 4**. In this the reduced density of the replicate is contour-plotted with W the abscissa and h_R the ordinate. The replicate density

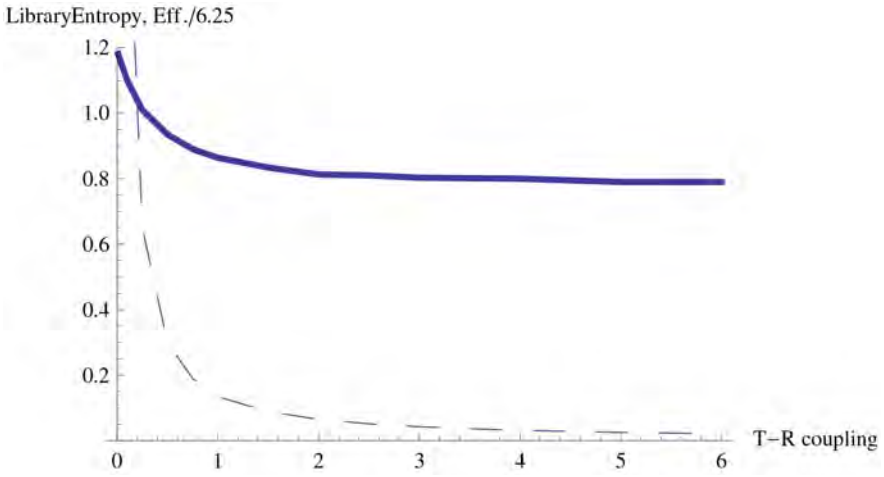

Figure 3. Full line: Combined post-SR reduced entropy of the rest of the spins in the Library, as function of the alignment-inducing coupling strength W.). Broken line: Efficiency (defined in the text, Equation (14), downscaled by 6.25).

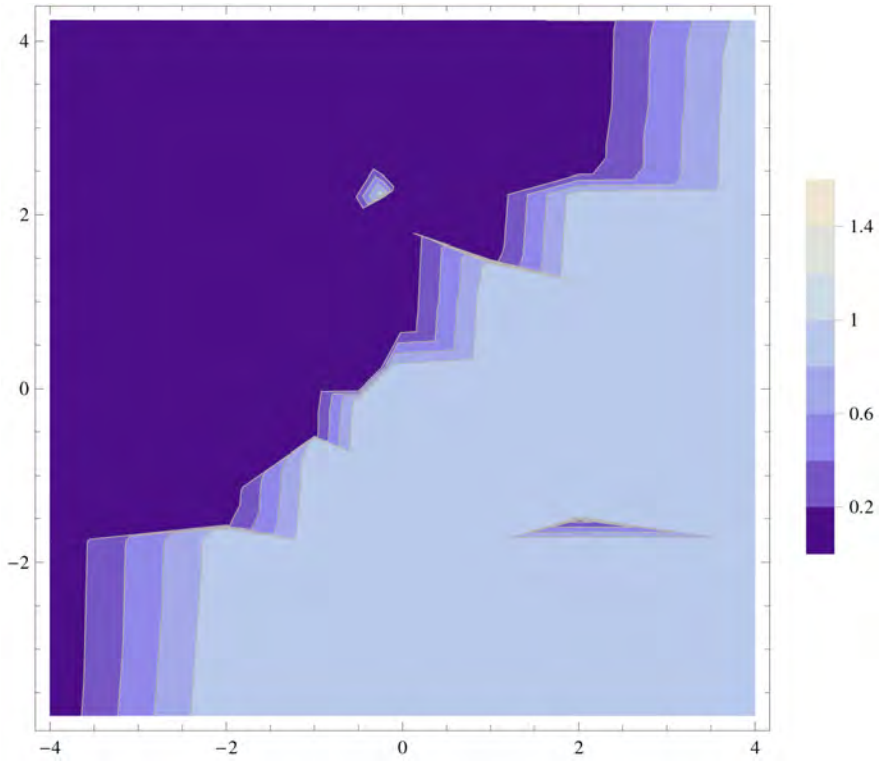

Figure 4. Contour plot depicting the reduced density (occupation probability) for the upper state of the replicate with the control (W) the abscissa and the replicate self-energy h_R the ordinate (both in our energy units). Inside the light blue region the upper state occupation probability approaches 1 (alignment with the template); in the dark blue region it tends to zero (anti-alignment). (The colour bar is relevant only between 0 and 1. The MATHEMATICA program for the figure is available upon request to the author).

is strongly demarcated, with the light blue region (in the right-lower part) representing alignment (replicating capability) between R and T and dark blue region (in the left-upper part) indicating anti-alignment, in the lowest energy state. From the graph, formally for the coefficient W entering the Hamiltonian as $-W\sigma_z^T\sigma_z^R$,

$$W > h_R \tag{16}$$

is the requirement for alignment, a criterion that is clearly favoring a strongly *attractive* control. Below this line the upper state density of the replicate tends to be unity alike to the template, while above the line it tends to vanish. The diagonal is a bifurcation line between the aligning and anti-aligning tendency of the ground state and on it the two lowest lying states with opposing alignment tendencies are energetically co-degenerate, implying an entropy increase. (The zig-zag nature of this line is a numerical artefact.) In the immediate vicinity of the line, the reduced replicate density is not yet close to 1 or 0, this is only the case further inside the respective regions. Speculatively, one may associate the bifurcation line with an inherent instability ("criticality" in Statistical Physics terminology), encountered in some, and perhaps several, biological systems.

The relatively sharp transition between alignment and anti-alignment is a quantum effect; in a classical description the control term would only gradually affect the statistic distributions of the spin orientation. Whereas the alignment changes dramatically across SR, the weights (RDM values) of the constituents in 2b' vary only minimally by about 5 percent, a property in line with their presumed enzymatic status.

6.1. Animate vs. Non-Animate

Figure 4 suggests, in the context of SR and the limitation of the two spin model, the following criteria as desiderata for the above dichotomy (not excluding further distinctions). The upper right quadrant of the figure is of interest (the rest having been shown only for completeness.) This shows that for SR to occur (*i.e.*, to be below the diagonal line) the control parameter W, promoting the alignment of the replicate with the template, must exceed the positive value of the replicate's self energy parameter (which favors non-alignment). In terms of the earlier description of the model in this paper, this requires a strong (bilinear) interaction between T-R and the surroundings, as also a weak R self-energy. The latter may be understood as a relative propensity of the replication candidate for changes (of structure, form, isomerisation, function, etc.), contrasting with non-animate entities that are as a rule fixated relative to their properties. In a terminology of [28] h_R is the "durability" of the replicate and, in line with what is found in that paper, its decrease (that is, moving vertically downwards in the figure) favors SR. Changes in the "durability" of the template do not substantially alter the figure. Clearly, not every system satisfying the above criteria will be "biological": in particular, they do not make allowance for the multiply layered sub-conformations [36], belonging to a particular conformation, making the latter a "mixed" rather than a "pure" quantum state (as a single spin state). Yet they provide a direction to which the present SR analysis points.

It may be objected (by regard to the lower half of the figure), that alignment arises also from a negative replica self-energy ($h_R < 0$) irrespective of the control's W strength. However, here the alignment is not due to an SR process, but to the statistical preponderance of the low energy state for the replicate, prior to the SR process.

6.2. Neglect of Excited States

At this point it is appropriate to examine the validity of the assumption that the system resides exclusively in its ground state, equivalent to the assumption of the scaled temperature kT low on the relevant energy scale. Our results show that in the parameter regime of strong replicativity, the second lowest level lies at cca. 0.3 in our energy units above the ground level. The stability of the template (meaning that calculationally it stays after the interactions in its low energy state) is due to its large Zeeman term energy-spread $2h_T$, which obtains at the energy value of 10 in our units (though most of the calculations were made with

a larger energy spread of 48). We may associate the stability with the actual, real life lifetimes of biological entities. These vary over several orders of magnitude; a lifetime at the short end is that of red blood cells τ_{RB}, namely cca. 10 days, or about 10^7 seconds. Assuming a Marcus-type decay or disintegration process with an attempt frequency $\nu = 10^{14}\mathrm{s}^{-1}$ [19], one may write

$$\tau_{RB} = \nu^{-1}\mathrm{e}^{2h_T/kT} \tag{17}$$

which leads to $kT = \frac{10}{48.3} < 0.3$ providing some justification for the neglect of higher lying states.

7. Conclusions

The process of living systems with regard to their self-reproductive capacity has here been given a quantum description, differing from (but not replacing) those current descriptions which present them as processes in a thermodynamically non-equilibrium setting. Admittedly, the actual complexity of biological reality has here been drastically reduced by representation of the manifold components through a single spin or qubit and the multiple properties by a single spin direction. It behoves us (and perhaps others) to extend the treatment to models comprising more entities and a variety of properties. A candidate for future treatment might be the self-assembly of a triatomic molecule, acting in some configuration as a template and inducing the assembly of a chosen trio of atoms selected from a large reservoir of atoms.

It may be objected, though, that by identifying the post-SR state with the ground state due to equilibration, thermalization creeps in, somehow which is external to the strictly Hamiltonian formalism of this work. However, according to the Eigenstate Thermalization Hypothesis in some of its formulations [22] [23], the expectation values of the spin alignment (a local observable) will occur autonomously, without thermal contact with an external heat-bath.

Acknowledgements

I thank helpful suggestions by Professors I. Bersuker, E. Eisenberg, J. P. Klinman and V. Polinger. The help of Prof. A. Yahalom in writing for our joint paper [33] a Mathematica program of the spin-spin Hamiltonian, and here used, and the technical help of N. and T. Kayser are acknowledged.

Data Availability

The data that support the findings of this study are available from the corresponding author upon reasonable request.

Conflicts of Interest

The author declares no conflicts of interest regarding the publication of this paper.

References

[1] Haken, H. (1983) Synergetics. An Introduction: Nonequilibrium Phase Transitions and Self-Organization in Physics, Chemistry and Biology. 3rd Edition, Springer Verlag, Berlin.

[2] Von Neumann, J. (1966) The Theory of Self-Reproducing Automata. University of Illinois Press, Urbana.

[3] Freitas, M. and Merkle, R. (2004) Kinematic Self-Replicating Machines. Landes Bioscience, Austin.

[4] Nigmatullin, R. and Prokopenko, M. (2020) Thermodynamic Efficiency of Interactions in Self-Organizing Systems.

[5] Cougnon, F.B.L. and Sanders, J.K. (2012) Evolution of Dynamic Combinatorial Chemistry. *Accounts of Chemical Research*, **45**, 2211-2221. https://doi.org/10.1021/ar200240m

[6] Moulin, E. and Giuseponne, N. (2011) Dynamic Combinatorial Self Replicating Systems. *Topics in Current Chemistry*, **322**, 87-105. https://doi.org/10.1007/128_2011_198

[7] Alberts, B., Johnson, A., Lewis, J., *et al.* (2002) Molecular Biology of the Cell. Garland Science, New York.

[8] Carnall, J.M.A., Waudby, C.A., Belenguer, A.M., Stuart, M.C.A. and Peyaralus, J.J.-P. (2010) Mechanosensitive Self-Replication Driven by Self-Organization. *Science*, **327**, 1502-1506. https://doi.org/10.1126/science.1182767

[9] Camazin, S., Deneubourg, J.-L., Franks, N.R., *et al.* (2001) Self-Organization in Biological Systems. Princeton University Press, Princeton. https://doi.org/10.1515/9780691212920

[10] Karsenti, E. (2008) Self-Organization in Cell Biology: A Brief History. *Nature Reviews Molecular Cell Biology*, **9**, 255-262. https://doi.org/10.1038/nrm2357

[11] Clixby, G. and Twyman, L. (2016) Self-Replicating Systems. *Organic & Biomolecular Chemistry*, **14**, 4170-4184. https://doi.org/10.1039/C6OB00280C

[12] Le Vay, K., Weise, L.I., Libicher, K., Mascarenhas, J. and Mutschler, H. (2019) Templated Self-Replication in Biomimetic Systems. *Advanced Biosystems*, **3**, Article ID: 1800313. https://doi.org/10.1002/adbi.201800313

[13] Zelinski, W.S. and Orgel, L.E. (1987) Autocatalytic Synthesis of a Tetranucleotide Analogue. *Nature*, **327**, 346-347. https://doi.org/10.1038/327346a0

[14] Feng, Q., Park, T.K. and Rebek, J. (1992) Cross-Over Reaction between Synthetic Replication Yield Active and Reactive Recombinants. *Science*, **256**, 1179-1180. https://doi.org/10.1126/science.256.5060.1179

[15] Luther, A., Brandsch, R. and von Kiederowski, G. (1998) Surface Promoted Replication and Exponential Amplification on DNA Analogues. *Nature*, **396**, 245-248. https://doi.org/10.1038/24343

[16] Szosztak, J.W. (2012) The Eightfold Path to Non-Enzymatic RNA Replication. *Journal of Systems Chemistry*, **3**, Article No. 2. https://doi.org/10.1186/1759-2208-3-2

[17] Liu, Y. and Sumpter, D.J.T. (2018) Mathematical Modeling Reveals Spontaneous Emergence of Self-Replication in Chemical Reaction Systems. *Journal of Biological Chemistry*, **293**, 18854-18863.

[18] Hordijk, W., Steel, M. and Kauffman, S. (2012) The Structure of Autocatalytic Sets: Evolvability, Enablement, and Emergence. *Acta Biotheoretica*, **60**, 379-392.

https://doi.org/10.1007/s10441-012-9165-1

[19] Schrödinger, E. (1944) What Is Life? The Physical Aspect of Living Cell. University Press, Cambridge.

[20] Kramers, H.A. (1934) L'interaction entre les atomes magnétogénes dans un cristal paramagnétique. *Physica*, **1**, 182-192. https://doi.org/10.1016/S0031-8914(34)90023-9

[21] Anderson, P.W. (1950) Antiferromagnetism. Theory of Superexchange Interaction. *Physical Review*, **79**, 350-358. https://doi.org/10.1103/PhysRev.79.350

[22] Srednicki, M. (1994) Chaos and Quantum Thermalization. *Physical Review E*, **50**, 888-892. https://doi.org/10.1103/PhysRevE.50.888

[23] Deutsch, J.M. (1991) Eigenstate Thermalisation Hypothesis. *Physical Review A*, **43**, 2046-2049.

[24] Bernal, J.D. (1951) The Physical Base of Life. Routledge and Kegan Paul, London.

[25] Prigogine, I. (1975) Dissipative Structures, Dynamics and Entropy. *International Journal of Quantum Chemistry*, **9**, 443-456. https://doi.org/10.1002/qua.560090854

[26] Dyson, F. (1980) Origins of Life. Cambridge University Press, Cambridge.

[27] Ruelle, D. (2017) The Origin of Life Seen from the Point of View of Non-Equilibrium Statistical Mechanics.

[28] England, J.L. (2015) Dissipative Adaptation in Driven Self-Assembly. *Nature Nanotechnology*, **10**, 919-923. https://doi.org/10.1038/nnano.2015.250

[29] England, J.L. (2013) Statistical Physics of Self-Replication. *The Journal of Chemical Physics*, **139**, 1219-1223. https://doi.org/10.1063/1.4818538

[30] Ruelle, D. (2015) Biology and Nonequilibrium: Remarks on a Paper by J. England, with a Remark by P. Gaspard. *European Physics Journal Special Topics*, **224**, 935-945. https://doi.org/10.1140/epjst/e2015-02437-4

[31] Duboniou, D., Caratzoulas, S., Kalyanaraman, C., Mincer, J.S. and Schwartz, S.D. (2009) Barrier Passage and Protein Dynamics in Enzymatically Catalyzed Reactions. *European Journal of Biochemistry*, **269**, 3103-3112. https://doi.org/10.1046/j.1432-1033.2002.03021.x

[32] Englman, R. and Jortner, J. (1970) The Energy Gap Law for Radiationless Transitions in Large Molecules. *Molecular Physics*, **18**, 145-164. https://doi.org/10.1080/00268977000100171

[33] Englman, R. and Yahalom, A. (2015) Open Systems' Density Matrix Properties in a Time Coarsened Formalism. *Foundations of Physics*, **45**, 673-690. https://doi.org/10.1007/s10701-015-9894-5

[34] Ptaszyncki, K. and Esposito, M. (2019) Entropy Production in Open Systems: The Predominant Role of Intra-Environmental Correlations. *Physical Review Letters*, **123**, Article ID: 200603. https://doi.org/10.1103/PhysRevLett.123.200603

[35] Ptaszyncki, K. and Esposito, M. (2020) Post-Thermalization via Information Stretching in Open Systems.

[36] Ansari, A., Berendsen, J., Browne, S.F., Frauenfelder, H., *et al.* (1985) Protein States and Protein Quakes. *Proceedings of the National Academy of Sciences*, **82**, 5000-5004.

Supplementary Information

Tracing in Binary and "Y-Nary" Digital Representations

In a previous publication [33] a convenient labelling of the multiple 1/2-spin states was achieved by replacing the ordinary, decimal numbering (in which, e.g., 2^5 is written as 32) with a binary representation, in which the same number is written as [10000] or possibly [000010000], etc. In this representation, the state of the r-spin is conveniently registered by having 0 or 1 at the r-th position from the right for, respectively the down- or up-state of the state. (While not relevant to the present work we, remark, that for entities or degrees of motion, that have Y rather than two alternative states, with Y being any arbitrary and finite integer, the same idea applies and the combined state would conveniently be represented by an Y-nary representation. Thus, for the not uncommon duodecimal representation, each degree of freedom would have entries at each position any one of the figures $1,2,\cdots,10,X,Y$. That this is not the end of the story, arises from the fact that in most (if not all) programming languages a summation or repeated operation command refers to the decimal representation and this necessitates a shunting between the representations.)

Here we recall that "tracing" is used in the statistical interpretation of quantum mechanics to obtain expectation values for a local operator (meaning one that operates on only one or a few degrees of motion), while summing over all states in the other degrees of motion. Insomuch as tracing also involves a summation [command], it is of interest to have at one's disposal a formula that carries out the tracing for states written in the binary (or Y-nary) representations. The following rule is given for the tracing over a single degree of motion's (namely, the r'th spin's) density of state (also known as the reduced density of state), but other traces follow from this. Astonishingly, the rule is very simple!

Eigen-solutions of the many-spin Hamiltonian matrix in Equation (2) of the text are of the form

$$\left|J\right\rangle=\sum_{\mathbf{n}}C_{\mathbf{n}}^{J}\left|\mathbf{n}\right\rangle,\mathbf{0}=\ ,\cdots,2^{N}-1 \tag{18}$$

where $\mathbf{n}$ runs over the 2^N combinations of $(0,1)$ (in that order).

Theorem 1

$$\begin{aligned}&Tr^{r}\left|0\right\rangle\left\langle 0\right|^{r}=\sum_{J'}\left|C_{\mathbf{n}}^{J'}\right|^{2},J'=J\ \text{ if }J\bmod 2^{r}=\left(0,\cdots,2^{r-1}-1\right)\\&Tr^{r}\left|1\right\rangle\left\langle 1\right|^{r}=\sum_{J''}\left|C_{\mathbf{n}}^{J''}\right|^{2},J''=J\ \text{ if }J\bmod 2^{r}=\left(2^{r-1},\cdots,2^{r}-1\right)\end{aligned} \tag{19}$$

Traces for other local operators than the density operator are treated analogously, with local expectation values inserted in the sums of Equation (19).

We next formulate the problem in more general terms, as an algorithmic exercise, and give a solution in Theorem 2.

N and Y are finite integers. Expressions for the numbers $J=0,\cdots,Y^{N}-1$ in a Y-nary system of digits, in a correspondence with a binary or decimal system, can be written as

$$J=\{I_N\ I_{N-1}\cdots I_r\cdots I_1\},\ I_r=0,\cdots,(Y-1),\ \text{for all}\ r=1,\cdots,N \tag{20}$$

(please note that $r=1$ is rightmost and $r=N$ is leftmost). (Example with $N=4$, $Y=3$: $11=\{0102\}$.) The problem is **to seek a rule** as to which J's to include in the trace-sum for a given $I_r=X$, *i.e.* which J's contain X at r position, with whatever entries at other positions.

Theorem 2

(Solution of the problem, expressed as a constructive procedure.)

For position $r\ (=\cdots,N)$ arrange all $J\left(0,\cdots,Y^N-1\right)$'s in bunches of size Y^{r-1} numbered $1,\cdots,Y^{N-r+1}$ The trace for any $I_r=(0,\cdots,Y-1)$ is then over all J values, starting at the I_r+1'th bunch and continuing to other bunches skipping over them $Y-1$-times. (E.g., for $Y=3, I_r=4$ include all J's in the fifth, eights, etc. bunch)

Proof

When I_r first appears $J=I_r*Y^{r-1}$ (thus in the binary system $\{01000\}=8=1*2^{4-1}$) and likewise, when I_r+1 first replaces I_r, $J=(I_r+1)*Y^{r-1}$, the difference is Y^{r-1} and this is the length of the bunch between them, such that I_r is at position r. This is also the bunch length, when there are non-zero digits to the left of r and then one meets again I_r after $Y-1$ bunches, those in which the digit at position r differs from I_r.

Illustration: In the binary system at position $r=1$ even and odd digits alternate, while at the last position $r=N$ the first half of 2^N J's have 0's and the second half has 1's.

Corollary

In many appplications, the number of states differ for different degrees of motion, e.g., in a discretization of radial and angular degrees of motion. Then the bunch length at the r'th position is $Y_{r-1}Y_{r-2}\cdots Y_1$, with skipping J's Y_r-1 times over.

Scientific Research Publishing

Open Journal of Biophysics, 2021, 11, 177-204
https://www.scirp.org/journal/ojbiphy
ISSN Online: 2164-5396
ISSN Print: 2164-5388

Internal Electrical Noises of BioFET Sensors Based on Various Architectures

Lusine Gasparyan[1,2], Ferdinand Gasparyan[1], Vahan Simonyan[2]

[1]Yerevan State University, Yerevan, Armenia
[2]DNA-HIVE LLC, Rockville, MD, USA
Email: fgaspar@ysu.am

How to cite this paper: Gasparyan, L., Gasparyan, F. and Simonyan, V. (2021) Internal Electrical Noises of BioFET Sensors Based on Various Architectures. *Open Journal of Biophysics*, **11**, 177-204.
https://doi.org/10.4236/ojbiphy.2021.112006

Received: February 1, 2021
Accepted: March 26, 2021
Published: March 29, 2021

Abstract

The results of a comparative literature analysis of internal electrical noises and signal-to-noise ratio for nanoscale BioFET (biological field-effect transistor) and DNA (deoxyribonucleic acid) sensors based on different architectures MIS (metal-insulator-semiconductor), EIS (electrolyte-insulator-semiconductor) and ISFET (ion-selective field-effect transistor) are presented. Main types, models and mechanisms of internal noises of bio- & chemical field-effect based sensors are analyzed, summarized and presented. For the first time, corresponding detail electrical equivalent circuits were built to calculate the spectral densities of noises generated in the active part of a solid (semiconductor, dielectric) and in an aqueous solution for MIS, EIS and ISFET structures based sensors. Complete expressions are obtained for the rms (root mean square) value of the noise current (or voltage), as well as the noise spectral densities for the architectures under study. The miniaturization of biosensors leads to a decrease in the level of the useful signal-current. For successful operation of the sensor, it is necessary to ensure a high value of the SNR (signal-to-noise ratio). In case of weak useful signals, it is necessary to reduce the level of internal electrical noise. This work is devoted to a detailed study of the types and mechanisms of internal electrical noises in specific biosensor architectures.

Keywords

Noise, Sensor, BioFET, Signal-to-Noise Ratio

1. Introduction

The field-effect transistor-based biosensors (BioFETs) [ion sensitive field effect transistors (ISFET), electrolyte-insulator-semiconductor (EIS) structures, its

modifications] are a potential candidate for future bioassay applications due to its low cost, fast response, high sensitivity and small sensing size. The pH-sensitive ISFETs are very important sensors for *in vivo* continuous monitoring application of physiological and environmental system. The accuracy of ISFET output measurement is greatly affected by the presences of internal noise, drift and slow response of the device. Although the noise analysis of BioFETs so far performed in different literature relates only to sources originated from FET structure which is almost constant for a particular device, the pH-dependent electrochemical noise has not been substantially explored and analyzed in detail. Reliable ways of DNA sequencing by ionic and tunneling current require low-noise and high-speed measurements of current in aqueous environments [1] [2] [3]. In nanopore experiments that involve ionic and/or tunnel current detection, several sources of noise need to be recognized and reduced. In addition, when a voltage is applied across the nanopore, a steep increase in low-frequency (LF) noise is observed. This region of the noise spectrum is called $1/f$ -noise, which is due to transient factors that influence the current flux (e.g., surface charge fluctuations, hydrophobic pockets on the pore surface, etc.) [4] [5] [6] [7]. Fluctuations of the environment parameters, such as ions and DNA molecules motion, introduce important scattering processes that may affect the viability of this approach to sequencing. A simple model that captures the role of this complex environment in electronic dephasing and its ability to remove charge carriers from current-carrying states is analyzed in [8]. It is finding that these effects do not strongly influence the current distributions due to the off-resonant nature of tunneling through the nucleotides. This result is expected to be a common feature of transport in molecular compounds. In particular, only large scattering strengths, as compared to the energetic gap between the molecular states and the Fermi level, significantly alter the form of the current distributions. Since this gap itself is quite large, the current distributions remain protected from this type of noise, further supporting the possibility of using transverse electronic transport measurements for DNA sequencing.

Previous works showed the four DNA nucleotides possess statistically distinguishable electronic signatures [9] [10] in the form of current distributions when accounting for structural distortions and partial control of the DNA dynamics (*i.e.*, by a transverse field) [2] [9] [10] [11] [12] [13]. These results indicate DNA sequencing is, in principle, possible via transverse current measurements. However, such studies have neglected scattering processes, such as fluctuations of the environment, which introduce current noise, and may thus affect the ability to distinguish the bases. It is clear that the noise of the force signal connected with the orientation of the bases in the pore on the passing current will be added, and the current signal will be distorted. The environment is composed of ionic and water fluctuations and other excitations that may drastically affect the electron dynamics, and thus the current and noise [14]. The complexity of the problem considered by Krems with coauthors, both in the number of atoms involved and

the type of scattering processes to take into account [8].

A solid-state nanopore platform with a low noise level and sufficient sensitivity to discriminate ssDNA homopolymers of poly-A40 and poly-T40 using ionic current blockade sensing are proposed and demonstrated in [15]. The key features of this platform are:

1) highly insulating dielectric substrates that are used to mitigate the effect of parasitic capacitance elements, which decrease the ionic current root mean square (rms) noise level to sub-10 pA and

2) ultra-thin silicon nitride membranes with a physical thickness of 5 nm (an effective thickness of 2.4 nm estimated from the ionic current) are used to maximize the SNR and the spatial depth resolution.

The reliable formation of small nanopores (<2 nm in diameter), fabrication of an extremely thin sensing zone with a thickness comparable to the spacing of each nucleotide, decrease of the noise level, and control of the translocation speed that would guarantee sufficient time to sense each nucleotide are the few challenges that limit the performance of solid-state nanopores. Among these issues, the excess noise level in solid-state nanopores (a few tens of pA to 100 pA, 10 times larger than that of protein counterparts [17] [18] [19] [20]) has been one of the key issues responsible for the degraded signal-to-noise ratio (SNR) and temporal and spatial resolution. In particular, the elevated parasitic capacitance generates a high level of dielectric noise that prevents sampling at high bandwidths. A novel solid-state nanopore platform with a sub-10 pA noise level by fabricating a SiN_x membrane directly on top of highly dielectric substrates proposed in [15]. It is demonstrated that high-frequency noise signals can be significantly reduced by replacing the commonly used Si substrate with an insulating one. Nanopore fabrication method presented in [16] consistently produces nanopores with low $1/f$ -noise levels (see **Figure 1**), comparable to fully wetted transmission electron microscopy (TEM)-drilled nanopores.

In [21] noise was calculated from the current versus time curves recorded in the solvent at 50 kHz sampling rates with 100 kHz low-pass filtering. The noise spectra showed linear components at the frequency above 10^2 Hz. This feature is

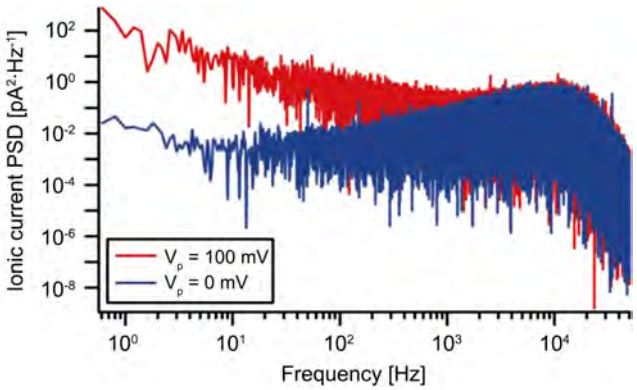

Figure 1. Power spectra density (PSD) of the ionic current at pore voltage of 0 and 100 mV. Root mean square noise of 40 pA is usually achieved at Vp = 0. Adapted from [16].

naturally interpreted as stemming from the voltage noise in the current amplifier coupled to the net capacitance of the mechanically controllable break junction (MCBJ) system. Morikawa reported also a use of insulator-protected nanoprobes for achieving 7.6 pA rms noise at 50 kHz sampling rates in an electrolyte solution [22]. Dielectric-covered MCBJ to create a pair of nano-exposed insulator/Au coaxial electrodes closely separated by 1 nm were utilized. It is observed insulator layer thickness dependent noise levels, which was attributed to decreased capacitance through replacing capacitive electric double layers by the low-k dielectrics.

The LF pH-dependent electrochemical noises that originate from the ionic conductance of the electrode-electrolyte-FET structure of the device and that the noise depends on the concentration of the electrolyte and $1/f$ in nature are investigated in [23]. The statistical and frequency analysis of this electrochemical noise of a commercial ISFET sensor, under room temperature has been performed for six different pH values ranging from pH2 to pH9.2. It is also proposed a concentration dependent a/f and b/f^2 model of the noise with different values of the coefficients *a* and *b*.

In [24] the small-signal and noise modeling of BioFET sensors implemented with EIS structures is studied, with emphasis on design guidelines for low-noise performance. In doing so, a modified form of the general charge sheet MOSFET model that better fits the EIS structure is used. It is discussed how if the reference electrode and the insulator-electrolyte generate no noise associated with charge transport, then the main noise mechanisms are the resistive losses of the electrolyte and the LF noise of the FET. It is found that for realistic sensor geometries and high electrolyte concentrations, the noise from the FET dominates the thermal noise from the electrolyte resistance, and the optimal biasing point for the FET for minimum noise is found to be around moderate inversion.

Syu with coauthors discusses how BioFET sensor can be designed by CMOS platform and the integration with sample processing and data processing apparatus for clinical sample testing [25]. This technology by clinical application is categorized, and a brief summary and comparison for BioFET sensor solutions are provided to each clinical problem. Because most of biomolecules carry electrostatic charges and bioactivities involve electrical potential changes. Noise contribution of commercial ISFETs, as well as of new designed pH-sensors, is studied and measured. Selected CMOS technology offers lower noise properties for designed ISFETs compared to commercial device, which is an advantage.

With the increased use of ISFET as a commercial micro- and nano-BioFET sensor for accurate biomedical measurements, noise factors will determine the performance limits of the system. The total noise comes from the ISFET sensor itself, as well as from the read-out circuit. The important noise components are present in a MOS transistor. The first one is the thermal noise, and the other $1/f$ -noise.

The study of noise in BioFETs is important for the reason that any source of

noise present in the sensor will impose a fundamental limit on the resolution and accuracy of the measurements and, hence, sensitivity of BioFETs limited by the sensor noise. In BioFET sensors presents several intrinsic and extrinsic rms noise sources [26]:

1) Intrinsic noise $\overline{i_{d1}^2}$ generated by the electronic device itself ($1/f$ -noise, channel thermal noise, source and drain diffusion resistance thermal noises, substrate resistance noise, shot noise).

2) Extrinsic electrochemical noise $\overline{i_{d2}^2}$ generated by ion-membrane interactions, in the solution and at the reference electrode.

3) Extrinsic noise source $\overline{i_{d3}^2}$ coming from biasing elements (power supplies, reference electrode biasing, external biasing resistances). These noise sources can generally be filtered.

The BioFET total noise spectrum can be presented as

$$\overline{i_{nd}^2} = \overline{i_{d1}^2} + \overline{i_{d2}^2}. \quad (1)$$

Extrinsic electrochemical noise has been modeled in [27]. Another noise analytical model was introduced in [28] based on site-binding model [29] electrochemical equilibrium equations and kinetic reaction rate expressions. The model described charge distributions in the electrolyte-oxide interfacial region and the manner in which ions are transferred between them.

The trend towards miniaturization of biosensors leads to a decrease in the level of the useful signal current. A high signal-to-noise ratio must be ensured for the sensor to work successfully. In case of weak wanted signals, it is necessary to reduce the level of internal electrical noise. As follows from the analysis of literature data, many types of internal electrical noises with different generation mechanisms and with different frequency behavior arise in biosensors. To improve the performance of sensors and increase the SNR value, it is necessary to study in detail the mechanisms of these noises and identify their effect on the operation of the sensors.

This work is devoted to a detailed study of the types and mechanisms of internal electrical noises, especially low-frequency noise, in specific biosensor architectures. For this purpose, the corresponding electrical equivalent circuits will be constructed and expressions for the rms noise value will be obtained.

Note that BioFETs several structures (ISFET, EIS, etc.) tend to be operated at low frequencies, where $1/f$ -noise is dominated, therefore, our main attention in the next parts of the paper will be focus mainly on low frequency noise.

2. Definition and Specification of Internal Current Noises

Main types of semiconductor based BioFET sensors operated using peculiarities of field-effect, especially properties of depletion layer near the interface of semiconductor-insulator. Those are field-effect biosensors: MIS, EIS and ISFET structures.

Electrical noises both in solids and in aqueous solutions have been well studied. Despite this, when considering specific biosensor architectures, it becomes

necessary to take into account some specific factors that are usually not taken into account in well-known formulas for noise. These factors are associated with miniaturization (size effects), with the generation of complex physical processes at the interfaces and surfaces of specific materials, etc. In this section, for a complete understanding of the problem, in addition to the already known formulas, we will also present expressions obtained and modernized by us for specific designs of sensors operating in different modes and frequency ranges.

Obvious that sensitivity, selectivity and detectivity of electronic devices determined in general by the internal electrical noise's types, its level and frequency behavior, and consequently by the SNR [30]. Voltage (or current) noise spectral density (NSD) S_V (or S_i) usually are presented by the rms value of the fluctuating voltage, $\overline{V^2}$, or by the fluctuating current $\overline{i^2}$ [31]:

$$\overline{V^2} = S_V \Delta f \ , \ \overline{i^2} = S_i \Delta f \ . \tag{2}$$

Here Δf is the elementary frequency bandwidth. Usually one assumes $\Delta f = 1$ Hz.

Equivalent schematic analogy of a noisy resistor presented in **Figure 2** for the case of equivalent voltage noise source (**Figure 2(a)**) and equivalent current noise source (**Figure 2(b)**).

Below we will shortly characterize the NSD and sources of the main types of noises in metals, semiconductors, dielectrics, bio liquids and electrolyte mediums.

The detailed analysis shows that main types of noises in bio- and chemical sensors can be classified as follows [24] [32] [33] [34] [35] [36].

2.1. Main Types of Noises in Bio- & Chemical FET Based Sensors

1) Noise generated in solid state region:

- Thermal noise;
- Generation-recombination (g-r) noise in the space charge region at the substrate-channel interface;
- $1/f$ and g-r noises generated due to trapping and detrapping on the semiconductor/insulator interface;
- Hooge's bulk $1/f$ -noise;
- Channel $1/f$ -noise.

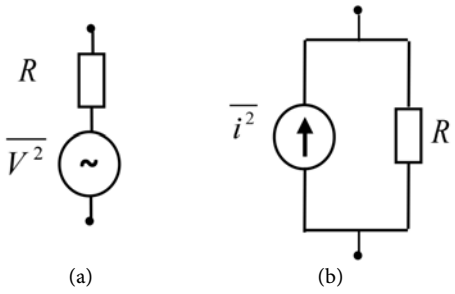

Figure 2. Equivalent schematic analogy of a noisy resistor *R*.

2) Electrochemical noise associated with the ion/membrane interactions:

- Thermal noise;
- Shot or Schottky noise;
- $1/f$ -noise in corrosive interfaces;
- Spurious noise.

3) Noise generated in the solution and at the reference electrode as well as noise resulting from the fluctuations of the biasing elements:

- Bulkthermal noise;
- Diffusion layer thermal noise;
- Biological noise.

Thermal noise is the electronic noise generated by the thermal motion of the charge carriers (electrons in conductors, electrons and holes in semiconductors, ions in aqueous solution, bio liquids, electrolytes and dielectrics) inside an electrical conductor at equilibrium, which happens regardless of any applied voltage. Thermal noise is present in all electrical circuits, and in sensitive electronic equipment such as sensors can drown out weak signals, and can be the limiting factor on sensitivity of electrical devices. In an ideal resistor it is approximately white, meaning that the power spectral density is nearly constant throughout the frequency spectrum [31]:

$$S_V^T = 4kTR \quad \text{or} \quad S_i^T = 4kTG\,, \tag{3}$$

where T is the thermodynamic temperature, R is the resistance and G is the conductance of the sample.

Those frequency independent noise spectra represent a simplification. An accurate calculation based on a quantum mechanics model gives

$$S_V^T(f) = 4Rhf\left(\frac{1}{2} + \frac{1}{e^{hf/kT} - 1}\right),$$

so that Equation (3) is basically only valid for $hf \ll kT$, *i.e.* for "low" frequencies and high temperatures (h is the Plank's constant). However, the quantum noise for $hf \gg kT$ has to be considered basically only for frequencies very much higher than in radio frequency and microwave application of concentration of non-equilibrium carriers during the random g-r and trapping-detrapping processes as on the interface impurity states and site bindings, as a result of the bulk random g-r processes.

Generation-recombination noise. NSD of the g-r noise determined by the following expression:

$$S_V^{g-r} = \frac{S_0}{1 + (\omega\tau)^2}.$$

Here S_0 is the some constant depending on the semiconductor bulk and surface properties, $\omega = 2\pi f$ is the cyclic frequency, τ is the time constant (for bulk semiconductors usually fluctuating minority carriers' life time). Generation-recombination noises spectra are described by the Lorentzians.

Biological noise conditioned by the random fluctuation of the number of captured particles/molecules in acqeous solution. Biological processes, such as protein synthesis or trafficking, undergo random fluctuations, "noise", that are often detrimental to reliable information transfer, but can also constitute opportunities for more efficient cellular computations.

Cellular noise is often investigated in the framework of intrinsic and extrinsic noise. Intrinsic noise refers to variation in identically-regulated quantities within a single cell: for example, the intra-cell variation in expression levels of two identically-controlled genes. Extrinsic noise refers to variation in identically-regulated quantities between different cells: for example, the cell-to-cell variation in expression of a given gene. The main source of stochastic variability on the cellular level is the intrinsic thermal fluctuations of biochemical reactions driving gene expression, signaling, cell cycle, motility, etc. These reactions occur through random collisions and transient binding of various molecular species within a single cell. Cellular noise is random variability in quantities arising in cellular biology. For example, cells which are genetically identical, even within the same tissue, are often observed to have different expression levels of proteins, different sizes and structures. These apparently random differences can have important biological and medical consequences [37] [38] [39]. Cellular noise was originally, and is still often, examined in the context of gene expression levels either the concentration or copy number of the products of genes within and between cells. As gene expression levels are responsible for many fundamental properties in cellular biology, including cells' physical appearance, behaviour in response to stimuli, and ability to process information and control internal processes, the presence of noise in gene expression has profound implications for many processes in cellular biology. For biological noise in [34] predicted a Lorentzian NSD (like g-r noise) with amplitude proportional to the number of particles/molecules in the solution.

Shot noise. Shot noise is a form of noise that arises because of the discrete nature of the charges carried by charge carriers, electrons, holes or ions. When looking at what is shot noise, it can be seen that it is particularly obvious when current levels are low. This is because the statistical nature of the current flow together with the discrete charge levels is more apparent. The continuous flow of these discrete pulses gives rise to almost white noise. There is a cut-off frequency which is governed by the time it takes for the electron or other charge carrier to travel through the conductor. This noise depends on the current flowing and is independent of temperature. The current through the space charge areas of a semiconductor junction (source-channel or drain-channel in BioFET sensors) are composed of many individual current impulses, due to the transport of individual charge carriers. Since this motion of carriers is statistical, we always have, besides the expected dc current I, also an ac noise component. With the assumption of individual, rectangular current impulses of the width τ for every charge component, we can calculate an NSD as following:

$$S_i^{S-N} = 2eI \times \frac{\sin^2(\pi f \tau)}{(\pi f \tau)^2}.$$

For low frequencies, there is $\sin(x)/x \propto 1$ and we get the commonly used expression for the shot noise

$$S_i^{S-N} = 2eI. \quad (4)$$

Spurious noise. To discuss digitally-based noise, we need to modify the traditional definition of noise. "Noise is almost always defined as being random, while digitally-based "noise" is deterministic, that is, it can be computed mathematically" [40]. It can be argued that this noise sources are, in fact, all spurious signals, determined by the repetition rate, rise/fall time, amplitude and waveform shape of the electronic signal at various points in the digital circuit. However, the number of these discrete spurious signals is sufficiently large that the net effect is much like random noise, not just a collection of well-defined spurs.

Usually the time constants involved in the detection of biological and chemical species in bio-liquid or electrolyte medium via field effect are relatively large. Therefore, it would be expected that LF (or flicker) noise is more critical than other types of noises in FET based bio- and chemical sensors.

Heerema with coauthors present an extensive study of the $1/f$ -noise in the ionic current through graphene nanopores and compare it to noise levels in silicon nitride pore currents [41]. They find that the $1/f$ -noise magnitude typically two orders of magnitude higher than for silicon nitride pores. This significantly lowers the SNR ratio in DNA translocation experiments. From examining the noise for pores of different diameters and at various salt concentrations, authors find that in contrast to silicon nitride pores, the $1/f$ -noise in graphene pores does not follow Hooge's relation. From studying the dependence on the buffer pH, they also show that the increased noise cannot be explained by charge fluctuations of chemical groups on the pore rim.

Low frequency noise conditioned by the random fluctuations of concentration or mobility of non-equilibrium carriers, ions and charged molecules in aqueous solution, by the trapping-detrapping processes on the free energetic states on the interface surface, as well as by the electron-phonon interactions in the bulk of semiconductor, and by the fluctuation of electron's and phonon's distribution functions. For the BioFET sensors LF NSD can be determined by the Hooge's model, McWhorter or correlated number-mobility fluctuation model and charge fluctuation model.

The main mechanisms of the formation of $1/f$ -noise in semiconductors (active part of FETs) presented in [27] [34] [42]-[55]. The basic $1/f$ -noise theories and models have been proposed to explain the phenomenon in FET based devices: the carrier density or number fluctuation model introduced by McWhorter [56], the carriers mobility fluctuation model proposed by Hooge empirical relation [57], electron-phonon interaction model [51] [53] [54] [58]

and charge fluctuation model [58] [59] proposed by us.

1) Hooge model [45] [46] [47] [48] [54] [60].

In his paper [45] Hooge proposed that $1/f$ -noise is essentially a bulk phenomenon. Working with metal films he championed an empirical relation for $1/f$ -noise in terms of resistance fluctuations, where the spectral density of the resistance is [60]:

$$R_n^2 = \frac{\alpha_H}{N}\frac{R^2}{f}.$$

Here N is the total number of free carriers in the bulk, and α_H is known as "Hooge's constant" an empirical parameter. This equation fits his data for metal films very well. In [61] Vandamme developed Hooge's theory for MOSFET devices, starting from the lattice scattering theory presented in [62], calculating

$$I_n^2 = \frac{\mu_0}{\mu_{eff}}\left(\frac{\mu_0}{\mu_l}\right)^2 \frac{q\alpha_H I_D^2}{wl\left(V_{GS}-V_{th}\right)}\frac{1}{f}, \tag{5}$$

where μ_0 is the low-field mobility of the carriers, μ_l is the mobility if only lattice scattering exists,

$$\mu_{eff} = \frac{\mu_0}{1+\theta\left(V_{GS}-V_{th}\right)},$$

θ is the mobility attenuation factor, V_{GS} and V_{th} are gate-source and threshold voltages. Again, significant bias dependences can be explained by changes in the assorted mobility parameters.

For modeling $S_i(f)$ dependencies barely will be useful Hooge's universal formula of current noises for materials and structures with macroscopically homogeneous current density [45]:

$$S_i(f) = \frac{\alpha_H I^2}{N_{tot} f^{\gamma}}, \tag{6}$$

where Hooge's parameter α_H for semiconductors typically $\alpha_H \approx 2\times 10^{-3}$ [42] [44] [46] [47] [48] [54], N_{tot} is the total number of electrons in the sample (means the total number of moving carriers in the sample), I is the current, magnitude of γ close to 1. Unfortunately, Hooge's formula does not give opportunity to take into account the processes take place in the bio-liquid or electrolyte medium of the BioFET sensors on the base of bare EIS and ISFET structures [63] [64].

2) McWhorter's or Correlated Number-Mobility Fluctuation Model

McWhorter, working with germanium filaments at MIT Lincoln Laboratory in 1957 proposed that flicker noise is primarily a surface effect [56]. He cites a number of experiments that showed that the $1/f$ -noise in germanium is dependent on the ambient atmosphere of the filament. He writes, "*recent results now leave little doubt that the noise is predominantly, if not entirely, a surface phenomenon*." Thus, the McWhorter number fluctuation (Δn) theory states that flicker noise is generated by fluctuations in the number of carriers due to

charge trapping in surface states. McWhorter obtained the necessary $1/f$ -spectrum by assuming that the time constant τ of the surface states varied with a $1/\tau$ distribution. Christensson *et al.* [65] [66] were the first to apply the McWhorter theory to MOSFETs, using the assumption that the necessary time constants are caused by the tunneling of carriers from the channel into traps located inside the oxide.

In the correlated number-mobility fluctuation theory NSD of the flat-band voltage fluctuation can be described as [27]

$$S_{V,FB}(f)=\frac{e^2kTN_t}{wl\beta C^2}\frac{1}{f}. \tag{7}$$

Here, w and l are width and length of the insulator gate, $\beta=\frac{2}{\hbar}\sqrt{2m^*\Phi_B}$ is the McWhorter's or tunneling parameter (m^* is the effective mass of electrons, Φ_B is the tunneling barrier height seen by electron at the interface), N_t is the oxide equivalent trap density in $eV^{-1}cm^{-3}$, C is the cumulative capacitance.

The McWhorter's model attributes the origin of $1/f$ -noise to the random fluctuation on the number of carriers in the channel due to fluctuations in the surface potential[1]. The fluctuations are caused by rapping and detrapping of carriers by energetic traps located near the Si-SiO_2 interface [67] [68]. In the saturation regimes the drain current NSD is calculated as:

$$S_{id}(f)=\frac{K_F I_{ds}}{C_{ox}L^2}\frac{1}{f}.$$

where K_F is a quality independent on bias but dependent on sensor fabrication process.

The Hooge's empirical model attributed $1/f$ -noise to carriers' mobility fluctuations, due to carrier interactions with crystal lattice fluctuations [45] [57]. At saturation

$$S_{id}(f)=\frac{\alpha_H q\mu_f I_{ds}\left(V_{gs}-V_{th}\right)}{L^2}\frac{1}{f},$$

where α_H is Hooge $1/f$ -noise parameter (Hooge's parameter), μ_f is carriers' effective mobility.

For low noise applications the level of thermal and $1/f$ -noises must be sufficiently low.

Based on the number fluctuation noise model [44] the calculations of the $1/f$ -noise spectra for ISFET has been presented in [69]. At saturation

$$S_{id(f)}=\frac{q^2\mu N_{ot}I_{dsat}}{C_{ox}L^2}\frac{1}{f},$$

and at sub-threshold

$$S_{id(f)}=\frac{q^4N_{ot}I_{ds}^2C_{inv}^2}{\left(C_{ox}+C_D\right)^4(kT)^2WL}\frac{1}{f}.$$

[1]In further we will show that for DNA sensors the fluctuations in the surface potential is depend on DNA molecules concentration.

Here C_{inv}, C_{ox} and C_D are the inversion, oxide and depletion layers capacitances per unit area, N_{ot} is the effective oxide traps density per unit area.

Problems of minimization of ISFET noises and results of LF noise measurements are detailed discussed in [70].

3) Charge Fluctuation Model

We can consider $1/f$ -noise source, $\overline{V^2}$, via fluctuation of the oxide traps (free bonds of proton donors O^- and proton acceptors OH_2^+, **Figure 2** in [13]) charge density. The charge density of occupied traps Q_t can be described as:

$$Q_t = \frac{eN_{ot}}{wl}, \tag{8}$$

where N_{ot} is the number of occupied traps. Then the NSD of the charge fluctuation of occupied traps is:

$$S_Q(f) = \left(\frac{e}{wl}\right)^2 S_{N_{ot}}(f). \tag{9}$$

Spectral density of the number fluctuations of occupied traps can be determined as [44]:

$$S_{N_{ot}}(f) = \frac{wlN}{f}. \tag{10}$$

The voltage-fluctuation noise spectral density can be calculated using the expression:

$$S_V(f) = \frac{S_Q(f)}{C_{ef}^2} = \frac{e^2 N}{wlC_{ef}^2}\frac{1}{f}. \tag{11}$$

In expressions (10) and (11) N is the equivalent density of traps per unit area at the SiO_2/electrolyte interface, $C_{ef} = \frac{C_i C_d}{C_i + C_d}$, C_i is the capacitance of the insulator (oxide) layer and C_d is the capacitance of the semiconductor depletion layer.

2.2. Signal-to-Noise Ratio (SNR)

SNR is a measure for comparison of the level of a desired signal to the level of background noise. SNR is defined as the ratio of signal power P_S to the noise power P_N. For linear devices SNR can be calculated from expressions:

$$\text{SNR} = \frac{P_S}{P_N} = \frac{I_S}{I_N} = \frac{I_S}{\sqrt{S_i \Delta f}} \tag{12a}$$

$$= \frac{V_S}{V_N} = \frac{I_S R_{tot}}{\sqrt{S_V \Delta f}}. \tag{12b}$$

Here $I_S(V_S)$ and $I_N(V_N)$ are useful signal current (voltage) and noise equivalent current (voltage), correspondingly, R_{tot} is the total resistance of the sample.

In review [70] different FET structures and detection principles are discussed,

including label-free and indirect detection mechanisms. The fundamental detection principle governing every potentiometric sensor is introduced, and different state-of-the-art FET sensor structures are reviewed. This is followed by an analysis of electrolyte interfaces and their influence on sensor operation. The successful detection of biomolecules by a BioFET is dictated by the sensor's intrinsic SNR. The detection limit of a traditional BioFET is fundamentally limited by biomolecule diffusion, charge screening, linear charge to surface-potential transduction, and flicker noise ($1/f$ -noise). In [71] authors demonstrate that t transistor technology called Negative Capacitor Field Effect Transistor (NCFET) offers nonlinear charge transduction and suppression of flicker noise to dramatically improve the SNR over classical Boltzmann sensors. The SNR improvement by interpreting the experimental results associated with the signal and noise characteristics of 2D MoS_2-based transistors quantify. The combined sensitivity enhancement and noise rejection guarantee a high SNR of the NCBioFET, making this device a promising candidate for realizing advanced integrated nano-biosensors. Most importantly, NCFETs can improve the SNR compared to traditional MOSFETs by reducing the LF flicker noise related to carrier number fluctuations. The results of the analysis show that despite the fundamental limits of charged-based BioFETs, the NCBioFET can improve the limits of label-free detection of biomolecules.

McAndrew with coauthors shows how correlated noise can be implemented in Verilog-A, and presents a new and simple technique to simulate the noise correlation coefficient using only the standard Space noise analyses [72]. An analytic proof is given that the noise contributed by the distributed gate resistance of the MOSFET can be modeled by including a gate resistance of value $R_g/3$ in series with the gate capacitance. Analyses of series and parallel combinations of devices are done to derive fundamental geometric scaling relations for noise. It is shown that gate noise must be distributed between gate-source and gate-drain components by maintaining proper symmetry. In saturation the correlation coefficient between gate and drain noise currents is imaginary ($j\sqrt{5/32}$) [72]. For resistors (including both thermal and $1/f$ -noise components) [73]

$$S_i(f) = 4kTG + K_F \frac{I^2}{WL}\frac{1}{f}.$$

Numerical and analytical theory of signal and noise of double-gated pH-sensors was provided in [74]. Relatively high noise floor of ultra-scaled NW sensors limits the SNR and the corresponding pH resolution (ΔpH_{min}) of such devices. It is defined ΔpH_{min} as being the minimum change in pH above the noise floor that can be continuously (without signal averaging) detected by the FET-sensor. In this article, authors offer a comprehensive theoretical analysis of double-gated pH sensors, with emphasis on the "so-called" amplified Nernstian response and the SNR. Authors combine the classical theory of the MOSFET [75] and the site-binding model [29] [76] to calculate the signal amplification and the noise levels for DGFETs (Double Gate FET) in various biasing configu-

rations (*i.e.*, accumulation, depletion, and inversion). For the noise calculation in DGFET sensors, authors account for the noise sources from the top and bottom sides of Si body by assuming that the DGFET can be viewed as two independent MOSFETs with different oxide thicknesses and gate voltages.

In [77] the electrical characteristics and pH responses of a Si-nanonet ISFET with ultra-thin parylene-H as a gate sensing membrane was reported. From the LF noise characterization, the SNR was extracted as high as ~3400 A/A with the lowest noise equivalent pH value of ~0.002 pH. These excellent intrinsic electrical and pH sensing performances suggest that parylene-H can be promising as a sensing membrane in an ISFET-based biosensor platform. The pH sensitivity of the pH ISFETs in various buffer solutions and conducted LF noise analysis for potential development in bioassay applications is evaluated. The pH responses of the devices were evaluated in various pH buffer solutions. A high pH sensitivity of 48.1 ± 0.5 mV/pH with a device-to-device variation of ~6.1% was achieved. The LF noise measurements of pH ISFET were performed in pH = 7 buffer solution under various gate bias conditions. The noise spectrum S_{ID} shows a typical $1/f^{\alpha}$ behavior with the exponential slope $\alpha \propto 1$ in a 3-dec frequency bandwidth of $f_1 - f_2 = 1 - 1000$ Hz. The SNR was extracted based on the following equation [78]:

$$\mathrm{SNR} = \Delta I \Big/ \sqrt{\int_{f_1}^{f_2} S_{ID}(f)\,\mathrm{d}f},$$

where ΔI is the drain current change in the range of pH = 4 − 10. In range 1 − 1000 Hz $S_{ID}(f) \propto \left(10^{-20} \div 10^{-25}\right)$ A²/Hz ($V_g \propto 0.8 \div 1.2$ V), $\mathrm{SNR}_{\max} \propto 3000$ A/A at $V_g \propto 1.0$ V.

Our research in the field of mechanisms of LF noise in semiconductors, semiconductor devices and BioFET sensors is devoted to a number of works (e.g. [50] [53] [54] [58] [59] [62] [79] [80] [81] [82]).

The main sources of electron mobility fluctuations in semiconductors were analyzed in [54], the theory of $1/f$ -fluctuations of the lattice mobility of current carriers in homogeneous semiconductors, the problems of space confined and bulk temporal fluctuations of acoustic phonons and relationship between models of $1/f$ -noise in semiconductors are developed, analyzed and presented in [58]. Phonons interface percolation dynamics detailed investigated in [51]. Influence of long-wave acoustic longitudinal-phonon percolation dynamics on $1/f$ -type noise level is modeled for homogeneous, non-degenerated and bounded semiconductors. Phonons percolation from semiconductor media to environment regions via so called "refraction points" of phonons' wave vector phase space is modeled within framework of the bulk mechanism of electron lattice mobility fluctuation. On the base of this mechanism it is shown, that semiconductor surface is the source of suppression of $1/f$ -noise [83]. Phonon mechanism of equilibrium fluctuation of carrier's mobility and properties of $1/f$ -noise analyzed also in [53].

Brief overview of the basic tendencies of development of nanoscale (bio-)chemical

sensors is presented in [79]. Last years' experimental data and theoretical models for LF excess noises are summarized and analyzed; in particularly works in the field of sensors functionalized by the nanoparticles, nanotubes (NT) and nanowires (NW) are discussed. Nanoscale FETs electrolyte gate field-effect devices and capacitive EIS structures were discussed. Main mechanisms of excess noises formation, behavior and peculiarities of the NSD, and the Hooge parameter were analyzed. Role of the functionalization (with several nanoparticles, NTs and NWs) on the essential reduction of $1/f$ -noise level is discussed. On the base of the analyses of electrical, physical, bio-chemical and other characteristics of the nanoscale sensors based on the NTs and NWs do some conclusions [79]:

- Low-frequency noise spectral density generally expressed as

$$S_v = A\frac{V^{2+\beta}}{f^{\gamma}}.$$

- The noise amplitude (parameter A) reflects the sample quality and increases with decreasing device size and depends on many parameters of material, its structure, sizes, NTs bulk and surface physical and chemical conditions, from its fabrication method.

$$A \propto R, \quad A \propto \frac{1}{N}, \quad A \propto \frac{1}{L}.$$

  where R is the device resistance, N is the number of atoms or carriers in the system, L is the sample length ($N \propto L$). $A = 1\times 10^{-11} R$. Parameter A varies within 10^{-13} up to 4×10^{-4}.

- The size scaling is incorporated in Hooge's empirical law $A = \frac{\alpha_H}{N}$.
- In the linear regime $1/A \propto \left|V_g - V_{th}\right|$ if noise is due to mobility fluctuations and $1/A \propto \left|V_g - V_{th}\right|^2$ if noise is due to number fluctuations.
- Parameter $\beta = 0$ is expected for pure resistance fluctuation in ohmic conductors. The $\gamma \neq 1$ behavior is associated with nonlinear characteristics.
- Excess noise with a slope different from unity ($\gamma \neq 1$) can be explained by a superposition of a few Lorentzians.

In [58] charge fluctuation LF noise model is modifying for an EIS structure. Physical processes take part in the semiconductor, insulator and electrolyte medium responsible for LF charge fluctuation are discussed. The complete electrical noise equivalent scheme for EIS structure is designed. Dependencies of NSD from charge fluctuation connected with processes on the electrolyte-insulator, insulator-semiconductor interfaces and bulk semiconductor are determined. It is shown that in the bare EIS structure a number of binding sites of the insulator surface actively take part in the trapping-detrapping processes with the ions and molecules situated in the electrolyte. Usually these are very slow processes. The capacitance C_{ox} and captured charge will be slowly fluctuated. In the other hand capacitance of the semiconductor depletion region also depend on charge fluctuation of insulator-semiconductor and insulator-electrolyte interfaces and fluctuated with them via surface potential. Generally, noise determined by the

modulation of semiconductor depletion region capacitance and surface potential due to charge fluctuation at the insulator-electrolyte interface. Low-frequency noise in an EIS structure functionalized with a multilayer of polyamidoamine (PAMAM) dendrimer and single-walled carbon nanotubes (SWNT) is studied in [64]. The NSD exhibits $1/f^{\gamma}$ dependence with the power factor of $\gamma \approx 0.8$ and $\gamma = 0.8 \div 1.8$ for the bare and functionalized EIS sensor, respectively. The gate-voltage NSD was practically independent on pH value of the solution, and is increased with increasing the gate voltage or gate-leakage current. It has been revealed that functionalization of an EIS structure with the PAMAM/SWNTs multilayer leads to an essential reduction of $1/f$ -noise. To interpret the noise behavior in bare and functionalized EIS devices, a gate-current noise model for capacitive EIS structures based on an equivalent flat band-voltage fluctuations concept has been developed [64]. The experimentally observed gate-voltage dependence of the noise explained by the gate-voltage-dependent changes in the occupancy of the oxide trap levels resulting in a modulation of the conductivity of current paths or charge carriers passing through the EIS structure.

LF noise spectroscopy at nanoscale and noise reduction in BioFET sensors functionalized with carbon NT multilayers areee detailed analyzed in [80] [82]. Transport properties of Si NW double gated BioFET sensors were investigated involving noise spectroscopy and current-voltage characterization [81]. Transport and noise properties of NW FET structures were investigated as in sensor configuration in an aqueous solution with different pH values. Furthermore, it is studied channel length effects on the noise, and pH sensitivity (**Figure 3**). The magnitude of the pH sensitivity increases with the increase of channel length approaching the Nernst limit value of 59.5 mV/pH. It is demonstrated that dominant $1/f$ -noise can be screened by the generation-recombination plateau at certain pH of the solution. It is shown that the measured value of the slope of $1/f$ -dependence on the current channel length is 2.7 which is close to the theoretically predicted value of 3.

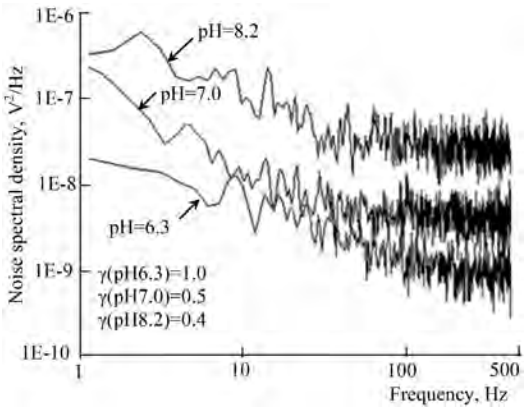

Figure 3. Noise spectra of NW double gated FET sensor, measured in different pH solutions Spectral dependence of LF noise for NW with length l = 10 μm measured at 300 K and several pH values: 6.3, 7.0, and 8.2 at the back gate voltage −5 V and front gate voltage −1 V. Adopted from [81].

3. Noises in BioFET Structures (MIS, EIS, ISFET)

In this section, for the first time, complete equivalent electrical circuits of some biosensors are constructed, taking into account the characteristics of a semiconductor, dielectric, aqueous solution, analyte and reference electrode. On the basis of these schemes, the spectral densities of the internal electrical noises (or rms values) were calculated. In these calculations, we used both well-known formulas (for example, for thermal noise) and formulas that we have modernized and obtained for specific investigated cases and operating modes. We also used the results of studies by other authors. These expressions and formulas can be found both in ours and in articles by other authors listed in the cited references.

For analyzing the noise properties, we need model equivalent electrical schemes of the elements of investigated structures. Below we will use the standard equivalent schematic analogy of a noisy resistor R consisting serial connected voltage generator via average square of the fluctuating voltage $\overline{V^2}$, or by the parallel connected current generator via average square of the fluctuating current $\overline{i^2}$ (**Figure 2(a)**, **Figure 2(b)**).

3.1. MIS Structures

On **Figure 4** the schematic picture of MIS structure is presented. Electrical and other characteristics of such type structures detailed are investigated [42] [48] [84] [85].

Electrical equivalent scheme for noises analyses for this case can be presented as the serial connection of semiconductor and insulator layers (see **Figure 5**). Each part has its bulk resistance (R_S and R_i, correspondingly for semiconductor and insulator layers) and parallel connected capacitances (C_d and C_i, correspondingly for semiconductor depletion layer and insulator), $\overline{V_S^2}$ and $\overline{V_i^2}$ are the noise sources for semiconductor and insulator, correspondingly, $\overline{V_{FB}^2}$ is the noise source conditioned by the flat-band voltage fluctuation. Total noise can be presented as the sum

$$\overline{V_{MIS}^2} = \overline{V_i^2} + \overline{V_S^2} + \overline{V_{FB}^2},$$

where

$$\overline{V_S^2} = 4kTR_{Sb} + \frac{4kTR_{Sd}}{1+\left(\omega R_{Sd}C_d\right)^2},\ \overline{V_i^2} = 4kTR_i,\ \overline{V_{FB}^2} = \frac{e^2kTN}{\gamma wlC_{ef}^2}\frac{1}{f},\ R_S = R_{Sb} + R_{Sd},$$

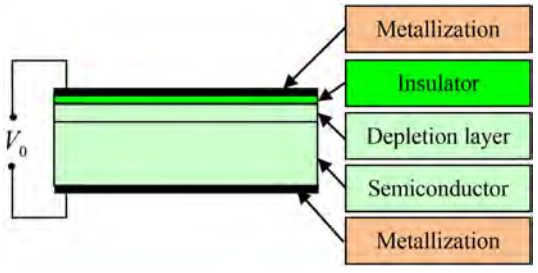

Figure 4. MIS structure (Al-pSi-SiO_2-Al).

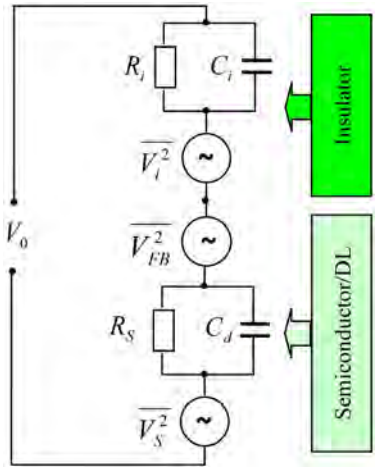

Figure 5. Electrical scheme for MIS noise analyses.

R_{Sb} and R_{Sd} are resistances of the bulk region and depletion layer of the semiconductor, correspondingly. Note that second term in right hand of $\overline{V_S^2}$ is the g-r part of the noises, conditioned by the g-r processes in the depletion region. The noise source $\overline{V_{FB}^2}$ characterizes fluctuation processes which take part on the interface of the depletion region and insulator. Thus

$$\overline{V_{MIS}^2} = 4kT\left(R_{Sb}+R_i\right)+\frac{e^2kTN_t}{\gamma wlC_{ef}^2}\frac{1}{f}+\frac{4kTR_{Sb}}{1+\left(\omega R_{Sd}C_d\right)^2}$$

$$\approx 4kTR_i+\frac{e^2kTN_t}{\gamma wlC_{ef}^2}\frac{1}{f}+\frac{4kTR_{Sb}}{1+\left(\omega R_{Sd}C_d\right)^2},$$

as $R_i \gg R_S$. Therefore, noises consist of the thermal, flicker and g-r components.

3.2. EIS Structures

Schematic picture of EIS structure and its electric equivalent scheme are presented in **Figure 6** and **Figure 7**. On the base of detailed analyses of several properties of EIS structures (see, e.g. [24] [27] [33] [36] [55] [86]), the electrical scheme for noises analyses for the case presence of DNA molecules (as a biomolecule) can be presented as on **Figure 9**. Main noise sources are conditioned by the flat-band voltage fluctuation, semiconductor bulk resistance fluctuation and electrolyte bulk resistance fluctuation. Comparable with the case of MIS structure, the following additional new sources of noises are presented on **Figure 7**:

$$\overline{V_{ch}^2}=\frac{e^2N}{AC_{ef}^2}\frac{1}{f};\ \overline{V_D^2}=4kTR_D;\ \overline{V_{RE}^2}=4kTR_{RE};\ \overline{V_b^2}=4kTR_b;\ \overline{V_{DNA}^2}=\frac{K_DV_D^\alpha}{f^b}.$$

Here $\overline{V_{ch}^2}$ is the spectral density of the charge fluctuation on the insulator-electrolyte interface [43], $\overline{V_D^2}$ is the spectral density of the thermal noise of charge transfer resistance fluctuations; R_D is the charge transfer resistance across electrolyte; $\overline{V_{RE}^2}$ is the spectral density of the thermal noise of the reference electrode resistance fluctuations; R_{RE} is the resistance of reference elec-

trode. $\overline{V_b^2}$ is the bulk electrolyte resistance (R_b) noise. The bulk electrolyte resistance can be approximated by the spreading resistance $R_b \approx \frac{1}{K}\sqrt{\frac{\pi}{wl}}$, K is the electrolyte conductivity [24]. The noise source $\overline{V_{DNA}^2}$ represents an anticipated noise source, V_D is the potential on the DNA layer, K_D some parameter, α and b is the some exponents. This is due to the random motion of the immobilized DNA probes within the electrolyte. This motion can couple to the semiconductor channel and cause random fluctuations in the carriers. It is expected that this noise source would depend on the potential across the DNA layer, since a higher potential could potentially further immobilize the probes and cause less noise [24].

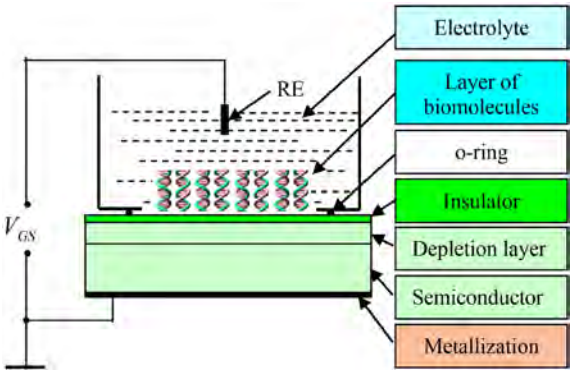

Figure 6. Schematic picture of EIS structure.

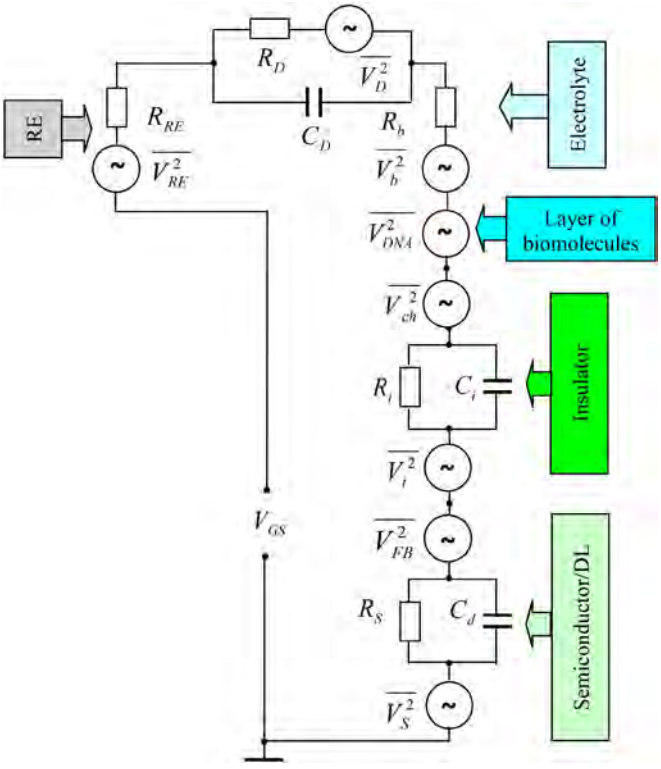

Figure 7. Electrical scheme for EIS noise analyses.

Therefore, for EIS structure we can write

$$\overline{V_{EIS}^2} = 4kT\left(R_{Sb} + R_i + R_b + R_D + R_{RE}\right) + \frac{K_D V_D^{\alpha}}{f^b} + \frac{e^2 N}{wlC_{ef}^2}\left(1 + \frac{kTN_t}{\gamma N}\right)\frac{1}{f} + \frac{4kTR_{Sb}}{1+\left(\omega R_{Sd} C_d\right)^2}.$$

Taking into account that

$$R_i \gg R_S + R_b + R_D + R_{RE},$$

for the NSD of the EIS biosensor we get

$$\overline{V_{EIS}^2} \approx 4kTR_i + \frac{K_D V_D^{\alpha}}{f^b} + \frac{e^2 N}{wlC_{ef}^2}\left(1 + \frac{kTN_t}{\beta N}\right)\frac{1}{f} + \frac{4kTR_{Sb}}{1+\left(\omega R_{Sd} C_d\right)^2}.$$

3.3. ISFET/MOSFET Structures

For the sensors on the base of such structures we have important difference. Schematic picture and electrical scheme of the ISFET/MOSFET structure presented on **Figure 8** and **Figure 9**, correspondingly. There we have two "current channels" [24] [33] [43] [44] [78] [79] [87] [88]: 1) vertical leakage current or equivalent voltage noise scheme (Metal-Semiconductor-Insulator-Electrolyte-RE, e.g. EIS, which electrical equivalent scheme presented on **Figure 7**), and 2) horizontal equivalent current noise scheme Source-Channel-Drain, (**Figure 9**, below).

Source-drain current noise can be successfully described by the Hooge's $1/f$ - noise, flat-band voltage fluctuation, semiconductor potential fluctuation and depletion region resistance fluctuation.

The NSD of the drain current noise in MOSFETs using also results of [24] can be presented as:

$$\overline{i_{DS}^2} = 4kT\mu_{ef}C_{ef}\frac{w}{l}\left(V'_{FB} + \varphi_{S0} - V_A - \varphi_{00} - \frac{\sqrt{2e\varepsilon_S N_D}}{C_i}\right) + \frac{e^2 kTN_t}{\gamma wlC_{ef}^2}\left(g_m + \alpha\mu_{ef}C_{ef}I_D\right)^2\frac{1}{f} + \frac{\omega\tau I_0^2}{1+\left(\omega\tau\right)^2}. \quad (13)$$

Here first term describes thermal, second term, flicker and third term, g-r part of the noise.

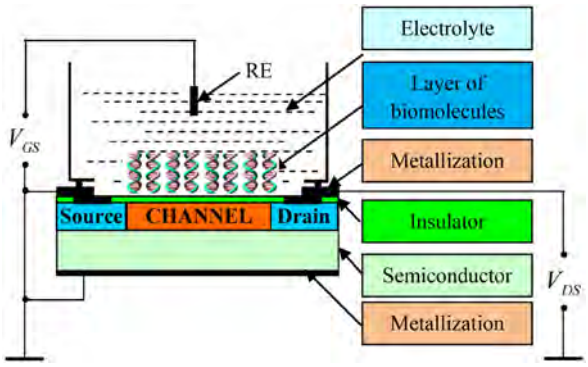

Figure 8. MOSFET/ISFET schematic picture.

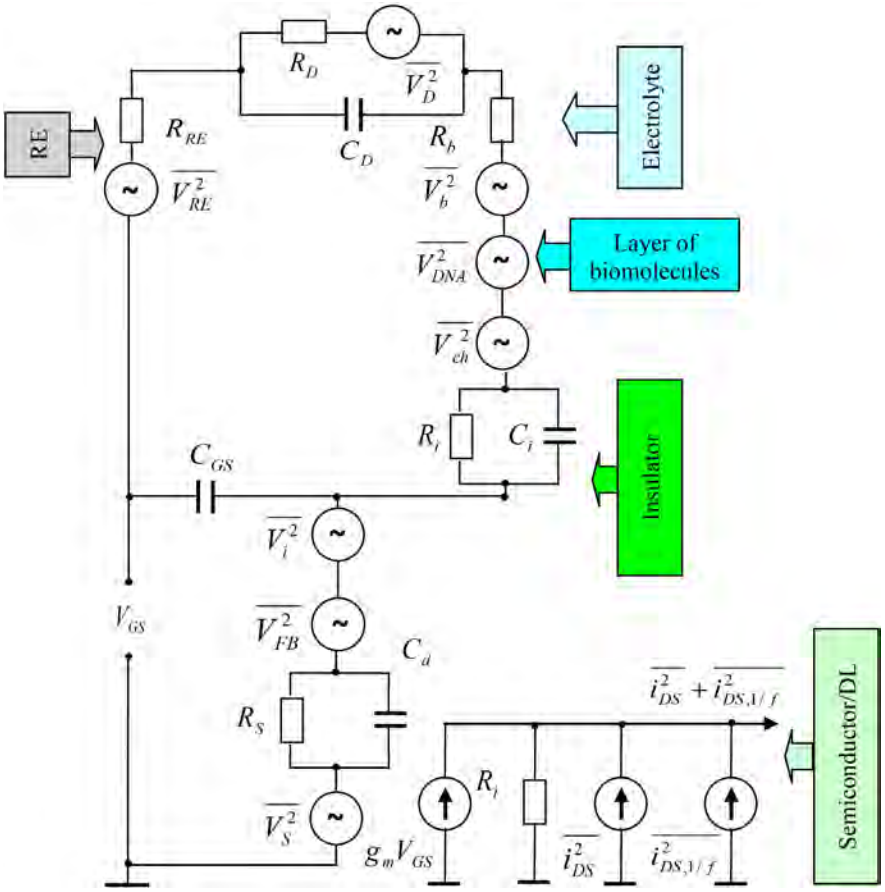

Figure 9. Electrical scheme for ISFET/MOSFET noise analyses (non faradaic electrode).

The NSD of the drain current noise in a load resistor R_L connected between source and drain in the linear regime approximated as [79] [88]:

$$\overline{i_{DS}^2} = \frac{\overline{i_{Ch}^2} + g_{Ch}^2 R_{DS}^2 \overline{i_{R_{dS}}^2}}{\left[1 + g_{Ch}\left(R_{dS} + R_L\right)\right]^2}. \tag{14}$$

According to Hooge's empirical mobility fluctuation model for elementary bandwidth $\Delta f = 1$ Hz

$$S_i(f) = \overline{i_{DS,1/f}^2} = \frac{e\alpha_H i_{DS}}{wlC_{ox}\left(V_{GS} - V_T\right)}\frac{1}{f} = \frac{e\alpha_H \mu_{ef} i_{DS} V_{DS}}{l^2}\frac{1}{f}. \tag{15}$$

In (12)-(13) α is Coulomb scattering coefficient; C_d is the capacitance of the diffusion layer; C_{ef} is the effective capacitance per unit area, consisting of the insulator and any functionalization layer; C_{dl} is the depletion layer capacitance; I_0 in (13) is the any parameter; R_L is the load resistor resistance; R_{Sd} is the resistance of semiconductor bulk and depletion layer; R_{dS} is the series resistances; $\overline{i_{Ch}^2}$ is the noise contribution from the channel with conductance g_{Ch}, $\overline{V_S^2}$ is the semiconductor bulk resistance voltage noise; $R_{ct} = \frac{kT}{Ze}\left|\frac{1}{i_T}\right|$ is the charge transfer resistance [34]; Z is the atomic number, i_T is the total redox

current; g_m is the transconductance; $\overline{V_{W1}^2} = 4kT\left(R_{ct} + R_{W1}\right)$; $\overline{V_{W2}^2} = 4kTR_{W2}$; R_{W1} and R_{W2} are the Warburg impedances [24]; $\overline{i_1^2} = 2Zei_T K(\omega)$ is the non-equilibrium noises source describe specific mass transfer effect at the electrolyte-electrode interface; $K(\omega)$ is the corresponding coefficient [33].

As we can see noise spectral density for all investigated cases consist three obligatory components: thermal, low-frequency and generation-recombination. Depending on the special experiment conditions either type of noises will be dominated in the appointed frequency interval. For example in EIS functionalized with PAMAM SWNT $1/f$ -noise dominates over thermal noise lower 10 Hz [63] [64], drain current NSD for the silicon-on-insulator (SOI) p-MOSFET biased back gate voltages $1/f$ -noise dominates in the region up to 500 Hz [79], for ISFETs at the buffer solutions pH7 and pH10 above a corner frequency ~1 Hz up to 400 Hz the measured spectra correspond to $1/f$ -noise and below this corner frequency the measured spectra correspond to $1/f^2$, in n- and p-channel dynamic-threshold MOSFETs on SOI substrate NSD has both quasi $1/f$ and Lorentzian spectra up to 10^4 Hz [89].

Author Contribution Information

All authors participated in the statement of the problem and discussion of the results. L. Gasparyan and F. Gasparyan conducted literature review. F. Gasparyan and V. Simonyan built equivalent circuits and participated in writing the text of the article.

Conflict of Interest

The authors declare no conflicts of interest regarding the publication of this paper.

References

[1] Gasparyan, L., Mazo, I., Simonyan, V. and Gasparyan, F. (2019) DNA Sequencing: Current State and Prospects of Development. *Open Journal of Biophysics*, **9**, 169-197. https://doi.org/10.4236/ojbiphy.2019.93013

[2] Gasparyan, L., Mazo, I., Gasparyan, F. and Simonyan, V. (2020) DNA Sequencing Modified Method through Effective Regulation of Its Translocation Speed in Aqueous Solution. *Open Journal of Biophysics*, **10**, 96-112. https://doi.org/10.4236/ojbiphy.2020.102009

[3] Gasparyan, L., Mazo, I., Simonyan, V. and Gasparyan, F. (2020) Noises and Signal-to-Noise Ratio of Nanosize EIS and ISFET Biosensors. *Open Journal of Biophysics*, **10**, 1-12. https://doi.org/10.4236/ojbiphy.2020.101001

[4] Hoogerheide, D.P., Garaj, S. and Golovchenko, J.A. (2009) Probing Surface Charge Fluctuations with Solid-State Nanopores. *Physical Review Letters*, **102**, 256804-256810. https://doi.org/10.1103/PhysRevLett.102.256804

[5] Pedone, D., Langecker, M., *et al.* (2010) Fabrication and Electrical Characterization of a Pore-Cavity-Pore Device. *Journal of Physics*: *Condensed Matter*, **22**, Article ID: 454115. https://doi.org/10.1088/0953-8984/22/45/454115

[6] Powell, M.R., Vlassiouk, I., Martens, C. and Siwy, Z.S. (2009) Nonequilibrium 1/f

Noise in Rectifying Nanopores. *Physical Review Letters*, **103**, Article ID: 248104. https://doi.org/10.1103/PhysRevLett.103.248104

[7] Smeets, R.M.M., Dekker, N.H. and Dekker, C. (2009) Low Frequency Noise in Solid-State Nanopores. *Nanotechnology*, **20**, Article ID: 095501. https://doi.org/10.1088/0957-4484/20/9/095501

[8] Krems, M., Zwolak, M., *et al.* (2009) Effect of Noise on DNA Sequencing via Transverse Electronic Transport. *Biophysical Journal*, **97**, 1990-1996. https://doi.org/10.1016/j.bpj.2009.06.055

[9] Lagerqvist, J., Zwolak, M. and Di Ventra, M. (2006) Fast DNA Sequencing via Transverse Electronic Transport. *Nano Letters*, **6**, 779-782. https://doi.org/10.1021/nl0601076

[10] Zwolak, M. and Di Ventra, M. (2005) Electronic Signature of DNA Nucleotides via Transverse Transport. *Nano Letters*, **5**, 421-424. https://doi.org/10.1021/nl048289w

[11] Lagerqvist, J., Zwolak, M. and Di Ventra, M. (2007) Influence of the Environment and Probes on Rapid DNA Sequencing via Transverse Electronic Transport. *Biophysical Journal*, **93**, 2384-2390. https://doi.org/10.1529/biophysj.106.102269

[12] Lagerqvist, J., Zwolak, M. and Ventra, M.D. (2007) Comment on Characterization of the Tunneling Conductance across DNA Bases. *Physical Review E*, **76**, Article ID: 013901. https://doi.org/10.1103/PhysRevE.76.013901

[13] Gasparyan, L., Mazo, I., Simonyan, V. and Gasparyan, F. (2019) ISFET Based DNA Sensor: Current-Voltage Characteristic and Sensitivity to DNA Molecules. *Open Journal of Biophysics*, **9**, 239-253. https://doi.org/10.4236/ojbiphy.2019.94017

[14] Ventra, M.D. (2008) Electrical Transport in Nanoscale Systems. Cambridge University Press, Cambridge, UK.

[15] Lee, M.-H., Kumar, A., Park, K.-B., Cho, S.-Y., *et al.* (2014) A Low-Noise Solid-State Nanopore Platform Based on a Highly Insulating Substrate. *Scientific Reports*, **4**, Article No. 7448. https://doi.org/10.1038/srep07448

[16] Fanget, A. (2013) Towards Tunneling Electrodes for Nanopore-Based DNA Sequencing. Thèse No. 5700, Ecole Polytechnique Fèdèrale de Lausanne, Suisse, 2013.

[17] Garaj, S., Hubbard, W., Reina, A., Kong, J., Branton, D. and Golovchenko, J.A. (2010) Graphene as a Subnanometre Trans-Electrode Membrane. *Nature*, **467**, 190-193. https://doi.org/10.1038/nature09379

[18] Merchant, C.A., Healy, K., Wanunu, M., *et al.* (2010) DNA Translocation through Graphene Nanopores. *Nano Letters*, **10**, 2915-2921. https://doi.org/10.1021/nl101046t

[19] Schneider, G.F., Kowalczyk, S.W., Calado, V.E., *et al.* (2010) DNA Translocation through Graphene Nanopores. *Nano Letters*, **10**, 3163-3167. https://doi.org/10.1021/nl102069z

[20] Wanunu, M., Dadosh, T., Ray, V., Jin, J., McReynolds, L. and Drndić, M. (2010) Rapid Electronic Detection of Probe-Specific microRNAs Using Thin Nanopore Sensors. *Nature Nanotechnology*, **5**, 807-814. https://doi.org/10.1038/nnano.2010.202

[21] Morikawa, T., Yokota, K., Tanimoto, S., Tsutsui, M. and Taniguchi, M. (2017) Detecting Single-Nucleotides by Tunneling Current Measurements at Sub-MHz Temporal Resolution. *Sensors* (*Basel*), **17**, 885-891. https://doi.org/10.3390/s17040885

[22] Morikawa, T., Yokota, K., Tsutsui, M. and Taniguchi, M. (2017) Fast and Low-Noise Tunneling Current Measurements for Single-Molecule Detection in an Electrolyte Solution Using Insulator-Protected Nanoelectrodes. *Nanoscale*, **9**, 4076-4081.

https://doi.org/10.1039/C6NR09278K

[23] Das, M.P. and Bhuyan, M. (2013)Modeling of pH Dependent Electrochemical Noise in Ion Sensitive Field Effect Transistors ISFET. *Sensors and Transducers*, **149**, 102-108. https://www.sensorsportal.com/HTML/DIGEST/P_1134.htm

[24] Dean, M.J., Shinwari, M.W., Ranuárez, J.C. and Landheer, D. (2006) Noise Considerations in Field-Effect Biosensors. *Journal of Applied Physics*, **100**, Article ID: 074703. https://doi.org/10.1063/1.2355542

[25] Syu, Y., Hsu, W. and Linz, C. (2018) Review—Field-Effect Transistor Biosensing: Devices and Clinical Applications. *ECS Journal of Solid State Science and Technology*, **7**, Q3196-Q3207. https://doi.org/10.1149/2.0291807jss

[26] Bergveld, P. (1981) The Operation of an ISFET as an Electronic Device. *Sensors and Actuators*, **1**, 17-29. https://doi.org/10.1016/0250-6874(81)80004-2

[27] Hemmerli, A., Janata, J. and Brophy, J.J. (1982) Electrochemistry of Chemically Sensitive Field Effect Transistors. *Journal of the Electrochemical Society*, **129**, 2306-2312. https://doi.org/10.1149/1.2123500

[28] Barabash, R.P. and Cobbold, R.S.C. (1983) Basic Limitations of ISFET and Silicon Pressure Transducers: Noise Theory, Models and Device Scaling. *Sensors and Actuators*, **4**, 427-438. https://doi.org/10.1016/0250-6874(83)85054-9

[29] Yates, D.E., Levine, S. and Healy, T.W. (1974) Site-Binding Model of the Electrical Double Layer at the Oxide/Water Interface. *Journal of the Chemical Society*, *Faraday Transactions*, **70**, 1807-1818. https://doi.org/10.1039/f19747001807

[30] Abrahamian, Yu., Martirissyan, R., Gasparyan, F. and Kocharyan, K. (2004) Methods and Materials for Remote Sensing. Infrared Photo-Detectors, Radiometers and Arrays. Kluwer Academic Publishers, Boston/Dordrecht/New York/London. https://doi.org/10.1007/978-1-4419-9025-9

[31] Van der Ziel, A. (1970) Noise Sources, Characterization, Measurements. Prentice-Hall, Englewood Cliffs, NJ.

[32] Gasparyan, F.V. (2009) Photoresponse of LAPS with Different Species Membranes: Modeling and Simulation. *Sensors & Transducers Journal*, **111**, 141-154.

[33] Hassibi, A., Navid, R., Dutton, R.W. and Lee, T.H. (2004). Comprehensive Study of Noise Processes in Electrode Electrolyte Interfaces. *Journal of Applied Physics*, **96**, 1074-1082. https://doi.org/10.1063/1.1755429

[34] Hassibi, A., Zahedi, S., Navid, R., Dutton, R.W. and Lee, T.H. (2005) Biological Shot-Noise and Quantum-Limited Signal-to-Noise Ratio in Affinity-Based Biosensors. *Journal of Applied Physics*, **97**, Article ID: 084701. https://doi.org/10.1063/1.1861970

[35] Massobrio, G., Martinoa, S. and Grattarola, M. (1992) Light-Addressable Chemical Sensors: Modeling and Computer Simulations. *Sensors and Actuators B*: *Chemical*, **7**, 484-487. https://doi.org/10.1016/0925-4005(92)80348-2

[36] Tyagai, V.A. (1971) Faradaic Noise of Complex Electrochemical Reactions. *Electrochimica Acta*, **16**, 1647-1654. https://doi.org/10.1016/0013-4686(71)85075-2

[37] Johnston, I.G. (2012) The Chaos within: Exploring Noise in Cellular Biology. *Significance*, **19**, 17-21. https://doi.org/10.1111/j.1740-9713.2012.00586.x

[38] Kaern, M., Elston, T.R., Blake, W.J. and Collins, J.J. (2005) Stochasticity in Gene Expression: From Theories to Phenotypes. *Nature Reviews Genetics*, **6**, 451-464. https://doi.org/10.1038/nrg1615

[39] Maheshri, N. and O'Shea, E.K. (2007) Living with Noisy Genes: How Cells Function Reliably with Inherent Variability in Gene Expression. *Annual Review of Biophysics*

and Biomolecular Structure, **36**, 413-434.
https://doi.org/10.1146/annurev.biophys.36.040306.132705

[40] Breed, G. (2006) Noise and Spurious in Digital Systems and Digitized Signals. In: *High Frequency Electronics*, Summit Technical Media, LLC, 50-52.
https://www.highfrequencyelectronics.com/Sep06/HFE0906_Tutorial.pdf

[41] Heerema, S.J., Schneider, G.F., Rozemuller, M., Vicarelli, L., Zandbergen, H.W. and Dekker, C. (2015) 1/f Noise in Graphene Nanopores. *Nanotechnology*, **26**, Article ID: 074001. https://doi.org/10.1088/0957-4484/26/7/074001

[42] Chim, W.K., Leong, K.K. and Choi, W.K. (2001) Random Telegraphic Signals and Low-Frequency Noise in Rapid-Thermal-Annealed Silicon-Silicon Oxide Structures. *Japanese Journal of Applied Physics*, **40**, 1-6.
https://doi.org/10.1143/JJAP.40.1

[43] Gasparyan, F.V., Melkonyan, S.V., Aroutiounyan, V.M. and Asriyan, H.V. (2000) 1/f Noises of Homopolar and Heteropolar Semiconductors. *International Journal of Modern Physics B*, **14**, 751-760. https://doi.org/10.1142/S0217979200000637

[44] Jakobson, C., Bloom, I. and Nemirovsky, Y. (1998) 1/f Noise in CMOS Transistors for Analog Applications from Subthreshold to Saturation. *Solid-State Electronics*, **42**, 1807-1817. https://doi.org/10.1016/S0038-1101(98)00162-2

[45] Hooge, F.N. (1969) 1/f Noise Is No Surface Effect. *Physics Letters A*, **29**, 139-140.
https://doi.org/10.1016/0375-9601(69)90076-0

[46] Hooge, F.N., Kleinpenning, T.G.M. and Vandamme, L.K.J. (1981) Experimental Studies on 1/f Noise. *Reports on Progress in Physics*, **44**, 479-532.
https://doi.org/10.1088/0034-4885/44/5/001

[47] Hooge, F.N. (1994) 1/f Noise Sources. *IEEE Transactions on Electron Devices*, **41**, 1926-1935. https://doi.org/10.1109/16.333808

[48] Hung, K.K., Ko, P.K., Hu, C. and Cheng, Y.C. (1990) A Unified Model for the Flicker Noise in Metal-Oxide-Semiconductor Field-Effect Transistors. *IEEE Transactions on Electron Devices*, **37**, 654-665. https://doi.org/10.1109/16.47770

[49] Melkonyan, S.V., Gasparyan, F.V., Aroutiounyan, V.M. and Asriyan, H.V. (1998) Temperature Chaos and the Lattice Character of the Hooge Parameter in Semiconductors. *Modern Physics Letters B*, **12**, 1245-1254.
https://doi.org/10.1142/S0217984998001475

[50] Melkonyan, S.V., Gasparyan, F.V., Aroutiounian, V.M. and Korman, C.E. (2003) Current Carrier Mobility Fluctuations in Homogeneous Semiconductors. *SPIE's First International Symposium on Fluctuations and Noise*, **5115**, 412-420.

[51] Melkonyan, S.V., Gasparyan, F.V., Aroutiounian, V.M. and Asriyan, H.V. (2005). 1/f-Type Noise in View of Phonons Interface Percolation Dynamics. *AIP Conference Proceedings*, **780**, 87-91. https://doi.org/10.1063/1.2036705

[52] Melkonyan, S.V., Aroutiounian, V.M., Gasparyan, F.V. and Korman, C.E. (2005) Peculiarities of Electron Distribution Function's Fluctuations Damping in Homogeneous Semiconductors. *Physica B*: *Condensed Matter*, **357**, 398-407.
https://doi.org/10.1016/j.physb.2004.12.004

[53] Melkonyan, S.V., Aroutiounian, V.M., Gasparyan, F.V. and Asriyan, H.V. (2006) Phonon Mechanism of Mobility Equilibrium Fluctuation and Properties of 1/f-Noise. *Physica B*: *Condensed Matter*, **382**, 65-70.
https://doi.org/10.1016/j.physb.2006.01.521

[54] Melkonyan, S.V., Gasparyan, F.V. and Asriyan, H.V. (2007) Main Sources of Electron Mobility Fluctuations in Semiconductors. *SPIE Fourth International Sympo-*

sium on Fluctuations and Noise, **6600**, 66001K.

[55] Peransin, J.-M., Vignaud, P., Rigaud, D. and Vandamme, L.K.J. (1990) l/f Noise in MODFETs at Low Drain Bias. *IEEE Transactions on Electron Devices*, **37**, 2250-2253. https://doi.org/10.1109/16.59916

[56] McWhorter, A.L. (1957) 1/f Noise and Germanium Surface Properties. In: Kingston, R.H., Ed., *Semiconductor Surface Physics*, University of Pennsylvania Press, Philadelphia, 207-228.

[57] Hooge, F.N. (2004) 1/f Noise Sources. In: Sikula, J. and Levinshtein, M., Eds., *Advanced Experimental Methods for Noise Research in Nanoscale Electronic Devices. NATO Science Series II: Mathematics, Physics and Chemistry* (*II. Mathematics, Physics and Chemistry*), Vol. 151, 3-10. https://doi.org/10.1007/1-4020-2170-4_1

[58] Männik, J., Heller, I., Janssens, A.M., Lemay, S.G. and Dekker, C. (2008) Charge Noise in Liquid-Gated Single-Wall Carbon Nanotube Transistors. *Nano Letters*, **8**, 685-688. https://doi.org/10.1021/nl073271h

[59] Gasparyan, F.V., Vitusevich, S.A., Offenhäusser, A. and Schöning, M.J. (2011) Modified Charge Fluctuation Noise Model for Electrolyte-Insulator-Semiconductor Devices. *Modern Physics Letters B*, **25**, 831-840. https://doi.org/10.1142/S0217984911026103

[60] Hooge, F.N. (1976) Discussion of Recent Experiments on 1/f Noise. *Physica*, **60**, 130-144. https://doi.org/10.1016/0031-8914(72)90226-1

[61] Vandamme, L.K.J. and de Werd, H.M.M. (1980) 1/f Noise Model for MOSTs Biased in the Nonohmic Region. *Solid-State Electronics*, **23**, 325-329. https://doi.org/10.1016/0038-1101(80)90199-9

[62] Hooge, F.N. and Vandamme, L.K.J. (1978) Lattice Scattering Causes 1/f Noise. *Physics Letters A*, **66**, 315-316. https://doi.org/10.1016/0375-9601(78)90249-9

[63] Gasparyan, F.V., Poghossian, A., Vitusevich, S.A., *et al.* (2009) 1/f-Noise in EIS Bio-Sensors Functionalized with 3 Layer-by-Layer PAMAM/Single Walled Carbon Nanotubes. *Proceedings of the* 20*th International Conference on Noise and Fluctuation*, Pisa, Italy, 14-19 June 2009, 133-136.

[64] Gasparyan, F.V., Poghossian, A., Vitusevich, S.A., *et al.* (2011) Low-Frequency Noise in Field-Effect Devices Functionalized with Dendrimer/Carbon-Nanotube Multilayers. *IEEE Sensors Journal*, **11**, 142-149. https://doi.org/10.1109/JSEN.2010.2052355

[65] Christensson, S., Lundstrom, I. and Svensson, C. (1968) Low Frequency Noise in MOS Transistors—I. Theory. *Solid-State Electronics*, **11**, 797-812. https://doi.org/10.1016/0038-1101(68)90100-7

[66] Christensson, S. and Lundstrom, I. (1968) Low Frequency Noise in MOS Transistors—II. Experiments. *Solid-State Electronics*, **11**, 813-820. https://doi.org/10.1016/0038-1101(68)90101-9

[67] Reimbold, G. (1984) Modified 1/f Trapping Noise and Experiments in MOS Transistors Biased from Weak to Strong Inversion—Influence of Interface States. *IEEE Transactions on Electron Devices*, **31**, 1190-1198. https://doi.org/10.1109/T-ED.1984.21687

[68] Vandamme, L.K.J., Li, X. and Rigaud, D.M. (1994) 1/f Noise in MOS Devices, Mobility or Number Fluctuations? *IEEE Transactions on Electron Devices*, **41**, 1936-1945. https://doi.org/10.1109/16.333809

[69] Jacobson, C.G. and Nemirovsky, Y. (1999) 1/f Noise in Ion Sensitive Field Effect Transistor from Subthreshold to Saturation. *IEEE Transactions on Electron Devic-*

es, **46**, 259-261. https://doi.org/10.1109/16.737468

[70] Kaisti, M. (2017) Detection Principles of Biological and Chemical FET Sensors. *Biosensors and Bioelectronics*, **98**, 437-448. https://doi.org/10.1016/j.bios.2017.07.010

[71] Zagni, N., Pavan, P. and Alam, M.A. (2019) Two-Dimensional MoS_2 Negative Capacitor Transistors for Enhanced (Super Nernstian) Signal-to-Noise Performance of Next-Generation Nano Biosensors. *Applied Physics Letters*, **114**, Article ID: 233102. https://doi.org/10.1063/1.5097828

[72] McAndrew, C.C., Coram, G., Blaum, A. and Pilloud, O. (2005) Correlated Noise Modeling and Simulation. *NSTI-Nanotech 2005*, 40-45. https://www.semanticscholar.org/paper/Correlated-Noise-Modeling-and-Simulation-McAndrew-Coram/579c166296242367f12f5b98071c9b515f7fc9ad

[73] Brederlow, R., Weber, W., *et al.* (1998) A Physically Based Model for Low-Frequency Noise of Poly-Silicon Resistors. *International Electron Devices Meeting* 1998, 6-9 December 1998, San Francisco, CA, 89-92. https://doi.org/10.1109/IEDM.1998.746286

[74] Tsividis. Y. (1999) Operation and Modeling of the MOS Transistor. 2nd Edition, McGraw-Hill, New York.

[75] Taur, Y. and Ning, T.H. (2009) Fundamentals of Modern VLSI Devices. 2nd Edition, Cambridge University Press, Cambridge. https://doi.org/10.1017/CBO9781139195065

[76] Meixner, L.K. and Koch, S. (1992) Simulation of ISFET Operation Based on the Site-Binding Model. *Sensors and Actuators B*: *Chemical*, **6**, 315-318. https://doi.org/10.1016/0925-4005(92)80077-B

[77] Jin, B., Lee, G.-Y., Park, C., Kim, D., Choi, W., Yoo, J.-W., Pyun, J.-C. and Lee, J.-S. (2018) Electrical Characteristics and pH Response of a Parylene-H Sensing Membrane in a Si-Nanonet Ion-Sensitive Field-Effect Transistor. *Sensors*, **18**, 3892. https://doi.org/10.3390/s18113892

[78] Haartman, M.V. and Ostling, M. (2007) Low-Frequency Noise in Advanced MOS Devices. Springer, Berlin/Heidelberg, Germany, 216. https://doi.org/10.1007/978-1-4020-5910-0

[79] Gasparyan, F. (2010) Excess Noises in (Bio-)Chemical Nanoscale Sensors. *Sensors & Transducers Journal*, **122**, 72-84. https://www.sensorsportal.com/HTML/DIGEST/november_2010/P_711.pdf

[80] Gasparyan, F.V. (2013) Chapter 11: Noise Reduction in (Bio-)Chemical Sensors Functionalized with Carbon Nanotube Multilayers. In: Vaseashta, A. and Khudaverdyan, S., Eds., *Advanced Sensors for Safety and Security*, *NATO Science for Peace and Security Series B*: *Physics and Biophysics*, Springer, Dordrecht, 139-150. https://doi.org/10.1007/978-94-007-7003-4_11

[81] Gasparyan, F., Zadorozhnyi, I., Khondkaryan, H., Arakelyan, A. and Vitusevich, S. (2018) Photoconductivity, pH-Sensitivity, Noise, and Channel Length Effects in Si Nanowire FET Sensors. *Nanoscale Research Letters*, **13**, 87-96. https://doi.org/10.1186/s11671-018-2494-5

[82] Vitusevich, S. and Gasparyan, F. (2011) Chapter 11: Low-Frequency Noise Spectroscopy at Nanoscale: Carbon Nanotube Materials and Devices. In: Marulanda, J.M., Ed., *Carbon Nanotubes Applications on Electron Devices*, IntechOpen Limited, London, 257-296. https://doi.org/10.5772/20026

[83] Gasparyan, F.V., Asriyan, H.V., Melkonyan, S.V. and Korman, C.E. (2010) Method

of 1/f Noise Reduction and Noise Level Manipulation in Semiconductor Based Devices. U.S. Patent Application for Letters Patent of the United States No. 61/332, 408.

[84] Pavelka, J., Sikula, J., *et al.* (2002) Noise and Transport Characterization of Tantalum Capacitors. *Microelectronics Reliability*, **42**, 841-847. https://doi.org/10.1016/S0026-2714(02)00013-6

[85] Zhigal'skii, G.P., Putrya, M.G. and Fedorov, A.S. (1989) Effect of Silicon-Wafer Preoxidation on the Low-Frequency Noise of MIS Structures. *Radiophysics and Quantum Electronics*, **32**, 862-868. https://doi.org/10.1007/BF01038815

[86] Chertouk, M. and Chovet, A. (1996) Origins and Characterization of Low-Frequency Noise in GaAs MESFET's Grown on InP Substrates. *IEEE Transactions on Electron Devices*, **43**, 123-129. https://doi.org/10.1109/16.477602

[87] Haartman, M.V. and Ostling, M. (2007) Effect of Channel Positioning on the 1/f Noise in Silicon-Oninsulator Metal-Oxide-Semiconductor Field-Effect Transistors. *Journal of Applied Physics*, **101**, Article ID: 03456. https://doi.org/10.1063/1.2433772

[88] Tian, H. and Gamal, A.E. (2001) Analysis of 1/f Noise in Switched MOSFET Circuits. *IEEE Transactions on Circuits and Systems II*: *Analog and Digital Signal Processing*, **48**, 151-157. https://doi.org/10.1109/82.917783

[89] Jomaah, J., Balestra, F. and Ghibaudo, G. (2005) Low Frequency Noise in Advanced Si Bulk and SOI MOSFETs. *Journal of Telecommunications and Information Technology*, **1**, 24-33.

Scientific Research Publishing

Open Journal of Biophysics, 2021, 11, 205-224
https://www.scirp.org/journal/ojbiphy
ISSN Online: 2164-5396
ISSN Print: 2164-5388

Bio-Electromagnetics without Fields: The Effect of the Vector Potential

Andras Szasz

Biotechnics Department, St. Istvan University, Budaors, Hungary
Email: biotech@gek.szie.hu

How to cite this paper: Szasz, A. (2021) Bio-Electromagnetics without Fields: The Effect of the Vector Potential. *Open Journal of Biophysics*, **11**, 205-224.
https://doi.org/10.4236/ojbiphy.2021.112007

Received: March 18, 2021
Accepted: April 27, 2021
Published: April 30, 2021

Abstract

Numerous considerations deal with specialties of bioelectromagnetic effects, including the force-free and field-free interactions. The fact that bioelectromagnetic phenomena consist of effects without mechanical forces and even without measurable fields looks impossible in the simple considerations. However, the stochastic fluctuations cause surprising results, with scientifically proven bioelectromagnetism in field-free conditions. In the first steps, we show the scalar and vector potentials' specialties instead of electric and magnetic fields defined by the well-known Maxwellian equations. The vanishing of the fields is connected to the potentials' stochastic fluctuations, the noises control the "zero-ground". The result shows a possibility of a wave that has no attenuation during its transmission through the material. In this meaning, the result is similar to the consequences of the scalar-wave (SW) considerations. The structural changes follow a particular noise spectrum (called pink-noise or 1/f noise), which keeps the entropy constant in a broad range of scaling magnification.

Keywords

Vector-Potential, Scalar-Potential, Stochastic-Processes, Field-Free Effects, Curl-Free Fields, Axial-Vector, Life, Homeostasis, Entropy, 1/f Noise

1. Introduction

The scientific research on electromagnetic effects on biological systems involves numerous theoretical and practical aspects in the last couple of centuries. Electric and magnetic fields, depending on their intensity, frequency, and gradients, affect the biological processes, including the immune cells [1]. The magnetic field could support chemotherapy in oncology [2], despite missing observable clinical changes, the improvement of the patients' quality of life is expected. On

the other hand, the current research shows the active role of the magnetic vector potential in biological processes [3]. The effect of weak magnetic fields is frequently described with a vector potential in several biological studies of [4] [5]. The vector potential can modify the quantum-states of the water [6], which could modify the complete chain-processes in living objects, governed by the phosphorylation catalyzing metal ions with magnetic nuclei [7].

Alternative medicine frequently uses the idea of water-state modification considerations [8], sometimes applying unproven effects. Controversial discussions about the "silent" bioelectromagnetics as "energy-medicine", [9] with force-free action on the viability of bacteria *E. coli* [10], the "electrosmog" [11] [12], the "new biophysical field", "force-free actions" [13], "scalar-wave effects" [14], "subtle energies" [15] generate heated debates. Intense debates with opposing opinion on physical [16] and mathematical basis [17] [18] for evidence-less applications were published. Direct investigation of quackery [19] and the variants of electromagnetic methods are questioned [20] [21]. Despite some spectacular results of the magnetic therapies, solid scientific proof and clinical evidence are missing, but the public's hopes keep alive even the poorly documented cases. The weak proofs well support the medical skepticism [22] [23].

The famous Maxwell equations [24] base the classical electrodynamics. Maxwell revolutionary introduced new physical quantities: the electric ($\boldsymbol{\mathcal{E}}$) and the magnetic ($\boldsymbol{\mathcal{H}}$) fields. The standing (free charge density ρ) and moving (current density $\boldsymbol{j}$) charges in vacuum form the sources of the fields:

$$div\left(\boldsymbol{\mathcal{E}}\right)=\frac{1}{\varepsilon_0}\rho \quad \text{and} \quad div\left(\boldsymbol{\mathcal{H}}\right)=0 \tag{1}$$

and the sources of the field's whirls in vacuum:

$$rot\left(\boldsymbol{\mathcal{E}}\right)=-\frac{\partial\boldsymbol{\mathcal{H}}}{\partial t} \quad \text{and} \quad rot\left(\boldsymbol{\mathcal{H}}\right)=\boldsymbol{j}+\varepsilon_0\frac{\partial\boldsymbol{\mathcal{E}}}{\partial t} \tag{2}$$

where $\varepsilon_0 \cong 8.854\times10^{-12}\ \mathrm{F/m}$ is a universal constant.

The conservation law of the charge:

$$\frac{\partial\rho}{\partial t}+div\left(\boldsymbol{j}\right)=0 \tag{3}$$

Sources and whirls define a vector-field which mathematical scheme makes the Maxwell Equations (1)-(2) complete to determine the two field-vectors $\boldsymbol{\mathcal{E}}$ and $\boldsymbol{\mathcal{H}}$. In presence of materials (like living objects, too), we have to take into account the atomic and molecular structures, which have bounded charges. In the case of the presence of materials, new sources appear. Introducing the electric-($\boldsymbol{P}$) and magnetic-($\boldsymbol{M}$) polarization vectors, we get the electric displacement field ($\boldsymbol{D}$) and the magnetic induction ($\boldsymbol{B}$):

$$\boldsymbol{D}=\varepsilon_0\boldsymbol{\mathcal{E}}+\boldsymbol{P} \quad \text{and} \quad \boldsymbol{B}=\mu_0\boldsymbol{\mathcal{H}}+\boldsymbol{M} \tag{4}$$

and $\mu_0 \cong 1.256\times10^{-6}\ \mathrm{N/A^2}$, is a universal constant.

Generally, we assume $\boldsymbol{P}$ and $\boldsymbol{M}$ depend on the $\boldsymbol{\mathcal{E}}$ and $\boldsymbol{B}$ fields respectively, so their Taylor's series:

$$\boldsymbol{P}(\boldsymbol{\mathcal{E}}) = \left(\boldsymbol{P}(\boldsymbol{\mathcal{E}})\right)_{\boldsymbol{\mathcal{E}}=0} + \left(\frac{\partial \boldsymbol{P}}{\partial \boldsymbol{\mathcal{E}}}\right)_{\boldsymbol{\mathcal{E}}=0} \boldsymbol{\mathcal{E}} + \frac{1}{2}\left(\frac{\partial^2 \boldsymbol{P}}{\partial \boldsymbol{\mathcal{E}}^2}\right)_{\boldsymbol{\mathcal{E}}=0} \boldsymbol{\mathcal{E}}^2 + \frac{1}{6}\left(\frac{\partial^3 \boldsymbol{P}}{\partial \boldsymbol{\mathcal{E}}^3}\right)_{\boldsymbol{\mathcal{E}}=0} \boldsymbol{\mathcal{E}}^3 + \cdots$$

and

$$\begin{aligned} \boldsymbol{M}(\boldsymbol{\mathcal{H}}) = \left(\boldsymbol{M}(\boldsymbol{\mathcal{H}})\right)_{\boldsymbol{\mathcal{H}}=0} + \left(\frac{\partial \boldsymbol{M}}{\partial \boldsymbol{\mathcal{H}}}\right)_{\boldsymbol{\mathcal{H}}=0} \boldsymbol{\mathcal{H}} + \frac{1}{2}\left(\frac{\partial^2 \boldsymbol{M}}{\partial \boldsymbol{\mathcal{H}}^2}\right)_{\boldsymbol{\mathcal{H}}=0} \boldsymbol{\mathcal{H}}^2 \\ + \frac{1}{6}\left(\frac{\partial^3 \boldsymbol{M}}{\partial \boldsymbol{\mathcal{H}}^3}\right)_{\boldsymbol{\mathcal{H}}=0} \boldsymbol{\mathcal{H}}^3 + \cdots \end{aligned} \tag{5}$$

The practical engineering simplifies (5) by considering only the linear term:

$$\boldsymbol{P}(\boldsymbol{\mathcal{E}}) = \left(\frac{\partial \boldsymbol{P}}{\partial \boldsymbol{\mathcal{E}}}\right)_{\boldsymbol{\mathcal{E}}=0} \boldsymbol{\mathcal{E}} \quad \text{and} \quad \boldsymbol{M}(\boldsymbol{\mathcal{H}}) = \left(\frac{\partial \boldsymbol{M}}{\partial \boldsymbol{\mathcal{H}}}\right)_{\boldsymbol{\mathcal{H}}=0} \boldsymbol{\mathcal{H}} \tag{6}$$

consequently

$$\begin{aligned} \boldsymbol{D} &= \varepsilon_0 \left[1 + \frac{1}{\varepsilon_0}\left(\frac{\partial \boldsymbol{P}}{\partial \boldsymbol{\mathcal{E}}}\right)_{\boldsymbol{\mathcal{E}}=0}\right] \boldsymbol{\mathcal{E}} = \varepsilon_0 \varepsilon_r \boldsymbol{\mathcal{E}} \text{ and} \\ \boldsymbol{B} &= \mu_0 \left[1 + \frac{1}{\mu_0}\left(\frac{\partial \boldsymbol{M}}{\partial \boldsymbol{\mathcal{H}}}\right)_{\boldsymbol{\mathcal{H}}=0}\right] \boldsymbol{\mathcal{H}} = \mu_0 \mu_r \boldsymbol{\mathcal{H}} \end{aligned} \tag{7}$$

where ε_r and μ_r (relative permittivity and relative permeability, respectively) denote the material parameters, which are constant in the linear approach. The linearity requests very special conditions: homogeneous materials, adequately small fields, and no permanent/remnant polarization/magnetization, and additionally the $\boldsymbol{P}(\boldsymbol{\mathcal{E}})$ and $\boldsymbol{M}(\boldsymbol{\mathcal{H}})$ functions must be smoothly continuous (existing derivatives are necessary).

2. Bio-Electromagnetism

First, confirm that you have the correct template for your paper size. The living material is inherently highly polarized and extremely heterogeneous and has various non-linear processes (physiological feedback). The linear approach does not describe the real, heterogeneous, non-linear living phenomena. The correct formulation of the complete Maxwell equations for living matter uses (4):

$$div(\boldsymbol{\mathcal{E}}) = \frac{\rho}{\varepsilon_0} - div(\boldsymbol{P}) \tag{8}$$

$$div(\boldsymbol{B}) = 0 \tag{9}$$

$$rot(\boldsymbol{\mathcal{E}}) = -\frac{\partial \boldsymbol{B}}{\partial t} \tag{10}$$

$$rot(\boldsymbol{B}) = \mu_0 \boldsymbol{j} + \mu_0 \varepsilon_0 \frac{\partial \boldsymbol{\mathcal{E}}}{\partial t} + \mu_0 \frac{\partial \boldsymbol{P}}{\partial t} + \mu_0 rot(\boldsymbol{M}) \tag{11}$$

Define the effective sources by comparison (1)-(2) with (8)-(11):

$$\rho_{eff} = \rho - \varepsilon_0 div(\boldsymbol{P}) \tag{12}$$

and

$$\boldsymbol{j}_{eff} = \boldsymbol{j} + \frac{\partial \boldsymbol{P}}{\partial t} + rot(\boldsymbol{M}) \tag{13}$$

Instead of the free-charge conservation (3) effective charge considering the presence of the material makes connection between the effective values:

$$\frac{\partial \rho_{eff}}{\partial t} + div\left(\boldsymbol{j}_{eff}\right) = C_{eff} \tag{14}$$

where C_{eff} depends on the derivatives of the $\boldsymbol{P}$ and $\boldsymbol{M}$ vectors. When the derivatives vanish, the free-charge conservation (see (3)) remains in force, $C_{eff} = 0$. The zero divergence in (9) (source-less condition because of magnetic monopole does not exist) defines a new quantity by introducing a vector-field ($\boldsymbol{A}$, called magnetic vector potential)

$$\boldsymbol{B} = rot\left(\boldsymbol{A}\right) \tag{15}$$

which automatically satisfies (9), because of $div\left(rot\left(\boldsymbol{A}\right)\right) \equiv 0$. The induction flux Φ of an open surface *S*, defines the physical meaning of the vector potential $\boldsymbol{A}$ having special role in bio-systems [25]. The Stokes' theorem gives the induction flux (Φ) encircled by the curve

$$\Phi = \int_S \boldsymbol{B}\mathrm{d}\boldsymbol{S} = \int_S rot\left(\boldsymbol{A}\right)\mathrm{d}\boldsymbol{S} = \int_L \boldsymbol{A}\mathrm{d}\boldsymbol{r} \tag{16}$$

where, the *L* circumflex of open surface *S*. Therefore, in the closed contour-line integral of vector potential gives Φ. On the one hand, the magnetic flux density in accordance with Faraday's induction law (10) generates Eddy-current loops of $\boldsymbol{\mathcal{E}}$. Let us enter the relationship using (15) and (10):

$$rot\left(\boldsymbol{\mathcal{E}} + \frac{\partial \boldsymbol{A}}{\partial t}\right) = 0 \tag{17}$$

which obviously introduces the φ scalar potential:

$$\left(\boldsymbol{\mathcal{E}} + \frac{\partial \boldsymbol{A}}{\partial t}\right) = -grad\left(\varphi\right) \tag{18}$$

To define the scale of the potentials, we usually fix the $div\boldsymbol{A}$ by the Lorentz condition:

$$div\boldsymbol{A} + \varepsilon_0\mu_0\frac{\partial \varphi}{\partial t} = 0 \tag{19}$$

The wave equations of the potentials:

$$\begin{aligned} \Delta\boldsymbol{A} - \varepsilon_0\mu_0\frac{\partial^2 \boldsymbol{A}}{\partial t^2} &= \mu_0\boldsymbol{j}_{eff} \\ \Delta\varphi - \varepsilon_0\mu_0\frac{\partial^2 \varphi}{\partial t^2} &= -\frac{\rho_{eff}}{\varepsilon_0} \end{aligned} \tag{20}$$

The simple realization of "pure" $\boldsymbol{A}$ vector is the space outside of an infinite cylindrical solenoid with r_0 radius supplied by *I* current in *n* loops creates the situation of $\boldsymbol{A} \neq 0$ when $\boldsymbol{\mathcal{E}} = 0$ and $\boldsymbol{B} = 0$, when the distance (*d*) from the solenoid $d'' r_0$. In this case $\boldsymbol{A}$ has only azimuthal component (A_θ) in the entire space from *d* distance. Inside the coil, we have, of course, the well-known $rot\left(\boldsymbol{B}\right) = B_z = 4\pi\varepsilon_0\mu_0 nI$.

The basic effects of the vector potential $\boldsymbol{A}$ in the quantum-mechanical processes indeed had been shown experimentally by the Aharonov-Bohm (AB) effect [26]. The $\boldsymbol{A}$ potential was directly verified pursuant to Equation (16). According to another experiment [27], the interference image shifts as compared to the free of the current case if the coil current is not equal to zero. The vector-potential $\boldsymbol{A}$ is a phase-shifter of the de Broglie-waves [28], measured experimentally too [29] Figure 1.

The minimal value of $\boldsymbol{A}^2$ has physical meaning [30], measures the existence (change) of the topologic structures. It could be connected to a phase transition in quantum-chromodynamics too [31]. Despite the AB effect has a quantum (microscopic) nature, some AB observations are macroscopic presenting their theoretical and practical proofs.

The two potentials ($\boldsymbol{A}$ and φ) determine the full field picture by simple mathematical transformations, so instead of the six variables (two vectors $\boldsymbol{\mathcal{E}}$ and $\boldsymbol{\mathcal{H}}$), only four parameters ($\boldsymbol{A}$ is a vector and φ, is scalar) describes the complete electromagnetic phenomenon [32]. The potentials are not only auxiliary quantities, presented as the basis of the description of electromagnetism [32]. The conservation of electric charge in (3) and (14) was considered as a fundamental condition instead of the induction law (10). The potential Equation (18) was used [32]. In this approach, a variation principle derives from the above equations and the Maxwell theory. Interestingly the opposite process, from [32] from Maxwell equations, does not work. In the relativistic four-dimensional curved space-time the basis of the electrodynamic discussions is the four-dimensional potential vector, composed from the components of $\boldsymbol{A}$ and φ [33] [34].

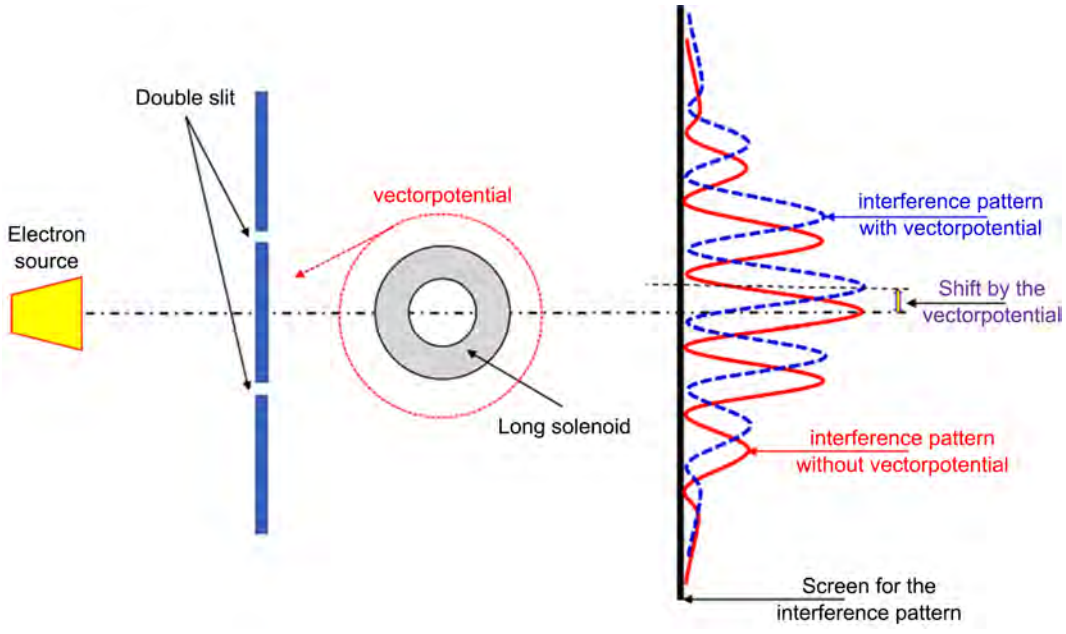

Figure 1. Effect of vectorpotential on the electron's eigenfunction, and the interference pattern. The shift is created by the presence of vectorpotential (Aharonov-Bohm effect).

3. Electromagnetic Forces

The fields are senseless for humans. A transformation to mechanical or high frequencies optical form must be involved to sense the electromagnetic activity. The optical frequencies present the fields in radiative waveforms, so presently, we deal with the force-transformation in invisible lower frequencies. Lorentz force density ($\boldsymbol{f}$) [35] connects the fields with the classical "force-based", human mechanical sensing:

$$\boldsymbol{f} = \rho\boldsymbol{\mathcal{E}} + \boldsymbol{j}\times\mu_0\boldsymbol{\mathcal{H}} \tag{21}$$

In the existence of materials, when $\boldsymbol{P}$ and/or $\boldsymbol{M}$ are presented (this is the real case) ρ_{eff} and $\boldsymbol{j}_{eff}$ have to be applied in the Lorentz force:

$$\boldsymbol{f} = \rho_{eff}\boldsymbol{\mathcal{E}} + \boldsymbol{j}_{eff}\times\boldsymbol{B} \tag{22}$$

The trivial force-free solution is when fields vanish. (See below the "field-free" solution.) The other, non-trivial vanish of the force is [36] when

$$\rho\boldsymbol{\mathcal{E}}'' \; \boldsymbol{j}\times\mu_0\boldsymbol{\mathcal{H}} \quad \text{and} \quad \boldsymbol{j} \parallel \boldsymbol{\mathcal{H}} \tag{23}$$

Formulate it with the polarization terms [37]:

$$\boldsymbol{f} = \rho\boldsymbol{\mathcal{E}} + \boldsymbol{j}\times\boldsymbol{B} + (\boldsymbol{P}\nabla)\boldsymbol{\mathcal{E}} + (\boldsymbol{M}\nabla)\boldsymbol{B} + \left(\mu_0\frac{\partial\boldsymbol{P}}{\partial t}\times\boldsymbol{B}\right) - \left(\mu_0\frac{\partial\boldsymbol{M}}{\partial t}\times\boldsymbol{\mathcal{E}}\right) \tag{24}$$

The complex force of (24) contains the direct forces, the dipole interactions ($\boldsymbol{f}_{dipole}$), and the radiation pressure ($\boldsymbol{f}_{rad}$) by two-two terms, respectively:

$$\boldsymbol{f}_{dipole} = (\boldsymbol{P}\nabla)\boldsymbol{\mathcal{E}} + (\boldsymbol{M}\nabla)\boldsymbol{B} \tag{25}$$

$$\boldsymbol{f}_{rad} = \left(\mu_0\frac{\partial\boldsymbol{P}}{\partial t}\times\boldsymbol{B}\right) - \left(\mu_0\frac{\partial\boldsymbol{M}}{\partial t}\times\boldsymbol{\mathcal{E}}\right) \tag{26}$$

These terms do not annihilate by (23) conditions. In consequence, the non-trivial solution of the force-field condition does not exist in bio-matter.

The potential formulation of the Lorentz force density by potentials (15) and (18) in the formulae (24):

$$\begin{aligned}\boldsymbol{f} = &-\rho\left(\frac{\partial\boldsymbol{A}}{\partial t} + grad(\varphi)\right) + \boldsymbol{j}\times rot(\boldsymbol{A}) - (\boldsymbol{P}\nabla)\left(\frac{\partial\boldsymbol{A}}{\partial t} + grad(\varphi)\right)\\ &+ (\boldsymbol{M}\nabla)rot(\boldsymbol{A}) + \left(\mu_0\frac{\partial\boldsymbol{P}}{\partial t}\times rot(\boldsymbol{A})\right) + \left(\mu_0\frac{\partial\boldsymbol{M}}{\partial t}\times\left(\frac{\partial\boldsymbol{A}}{\partial t} + grad(\varphi)\right)\right)\end{aligned} \tag{27}$$

The dynamics of charged particles could also be introduced in parallel of the classical dynamics an equation [38].

$$\frac{\mathrm{d}}{\mathrm{d}t}\left(\boldsymbol{p}_e + \frac{q}{c}\boldsymbol{A}\right) = q(\boldsymbol{v}\nabla)\boldsymbol{A} + q\cdot\boldsymbol{v}\times rot\boldsymbol{A} - q\nabla\varphi \tag{28}$$

where q is the electric charge. In more symmetric form:

$$\frac{\mathrm{d}}{\mathrm{d}t}\left(\boldsymbol{p}_e + \frac{q}{c}\boldsymbol{A}\right) = -q\nabla\left(\varphi - \frac{1}{c}(\boldsymbol{v}\cdot\boldsymbol{A})\right) \tag{29}$$

The Equation (29) shows important behaviors of the potentials: $e\boldsymbol{A}$ is a momentum-like term, while ($\boldsymbol{v}\cdot\boldsymbol{A}$) together with φ has potential character.

4. Tunneling through a Potential Barrier

There is no Lorentz force acting in the direction of the charge velocity, so no energy exchange could happen. The probability p_i of an energy-state E_i is proportional with the Boltzmann expression:

$$p_i \sim \mathrm{e}^{-\frac{E_i}{kT}} \tag{30}$$

does not change by (curl-free) magnetic action in particle-description. In principle, we expect an effect of the curl-free field [39], on the basis of quantum mechanics.

The quantum-mechanics derives the surface and bulk chemical reactions governing the living processes. The Schrödinger picture of quantum mechanics in a case when a particle of charge q moves in the electromagnetic field can be described by the time-dependent single-particle equation with Ψ wave-function and $\hat{\boldsymbol{H}}$ Hamilton operator ignoring the reaction of a particle to the field:

$$i\hbar\frac{\partial\Psi}{\partial t}=\hat{\boldsymbol{H}}\Psi \tag{31}$$

The information obtainable about the system is given by the wave function Ψ normalized to one. Consequently, the phase of wave function includes all information relating to the system. It was shown by Aharonov and Bohm in their famous effect [40] that the potentials have a fundamental role in quantum-mechanics without using the electromagnetic fields. Schrödinger equation where $\Psi(\boldsymbol{r},t)$ is the complex wave function $\hat{\boldsymbol{H}}$ is a Hamilton operator, describing the total energy of the system, which, in the case of Aharonov-Bohm conditions [40], can be expressed as follows:

$$\hat{\boldsymbol{H}}=\frac{1}{2m}\left(\frac{\hbar}{i}\nabla-q\boldsymbol{A}\right)^2+q\varphi. \tag{32}$$

where q is the charge in the V volume

$$q=\int_V \rho \mathrm{d}r^3 \tag{33}$$

Consequently, the Schrödinger equation of (31):

$$i\hbar\frac{\partial\Psi}{\partial t}=\frac{1}{2m}\left(\frac{\hbar}{i}\nabla-q\boldsymbol{A}\right)^2\Psi+q\varphi\Psi=\hat{\boldsymbol{H}}\Psi \tag{34}$$

In Equation (34) only the potentials have a role; the classical fields are completely missing. The scalar potential affects the potential energy, while the vector potential is connected to the charge's momentum in the Schrodinger equation. In the plane-wave solution

$$\Psi(\boldsymbol{r},t)\propto\exp\left(i\frac{E\cdot t-(\boldsymbol{p}_m+q\boldsymbol{A})\boldsymbol{r}}{h}\right) \tag{35}$$

Note classical fields do not appear in Equation (34) too. Where $\boldsymbol{p}_m$ is the mechanical momentum of the particle with m mass and $\boldsymbol{v}$ speed:

$$\boldsymbol{p}_m=m\cdot\boldsymbol{v} \tag{36}$$

In consequence of (35), the magnetic vector-potential changes the wave-number only. Using the normality of Ψ

$$\int_{V,|\boldsymbol{r}|\to\infty} \Psi(\boldsymbol{r},t)\Psi^{*}(\boldsymbol{r},t)\mathrm{d}V = 1 \tag{37}$$

and using (35) the coordination dependence of Ψ is:

$$\frac{1}{r}\exp\left(-\frac{p_r r}{h}\right)\exp\left(-i\frac{qA_r r}{h}\right) \tag{38}$$

which changes the amplitude of the wave-function at the transmission of a potential-barrier (Figure 2). The amplitude of the probability could be higher and also less under the action of the vector potential than without it.

Consequently, when two charged particles create a chemical bond, the external vector-potential interacts and changes the structure.

The average of effective sources $\boldsymbol{j}_{eff}$ and ρ_{eff} could be expressed by:

$$\langle \boldsymbol{j}_{eff} \rangle = Tr[\boldsymbol{j}\hat{\boldsymbol{S}}], \quad \langle \rho_{eff} \rangle = Tr[\rho\hat{\boldsymbol{S}}] \tag{39}$$

where $\hat{\boldsymbol{S}}$ is the Neumann's density operator:

$$\frac{\partial\hat{\boldsymbol{S}}}{\partial t} = -\frac{\boldsymbol{j}}{\hbar}[\hat{\boldsymbol{S}},\hat{\boldsymbol{H}}], \quad [\hat{\boldsymbol{S}} = \Psi\circ\Psi] \tag{40}$$

This approach (in principle) makes the complex system completely calculable.

5. The "Curl-Free" Potential Situation

A challenge arises when we have a curl-free magnetic vector potential:

$$rot(\boldsymbol{A}) = 0\,, \tag{41}$$

In this case, (according to (15)) the $\boldsymbol{B}$ field vanishes, pure $\boldsymbol{A}$ field exists only [41]. A kind of the curl-free solution is free from the magnetic field, but according to (11) at high frequencies:

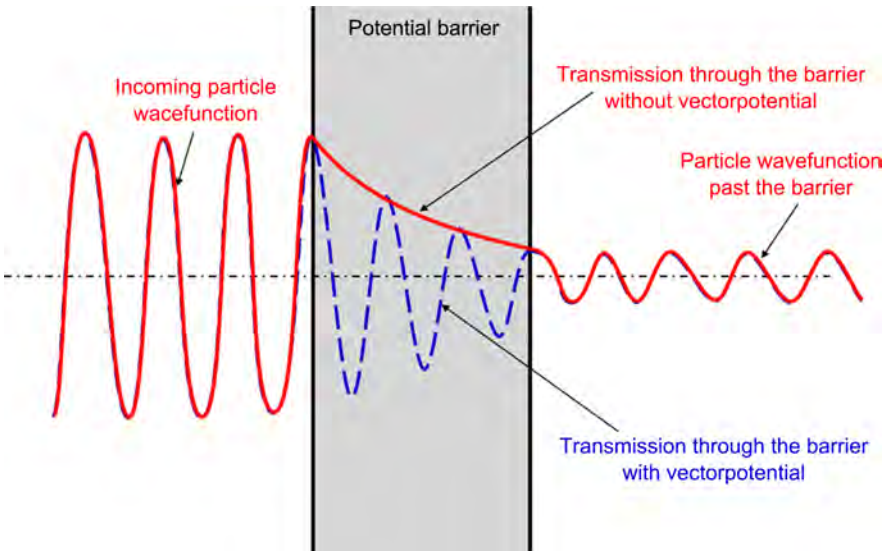

Figure 2. Particle transmission through a potential barrier with and without magnetic vector potential.

$$rot(\boldsymbol{B}) \approx 0 \tag{42}$$

because from (11) a part could be zero, and the other part near to zero:

$$\mu_0 \boldsymbol{j} + \mu_0 rot(\boldsymbol{M}) = 0 \quad \text{and} \quad \mu_0 \varepsilon_0 \frac{\partial \boldsymbol{\mathcal{E}}}{\partial t} + \mu_0 \frac{\partial \boldsymbol{P}}{\partial t} \approx 0 \tag{43}$$

The electric field does not vanish if $\boldsymbol{A}$ changes by time ($\boldsymbol{A} = \boldsymbol{A}(t)$):

$$\boldsymbol{\mathcal{E}} = -grad(\varphi) - \frac{\partial \boldsymbol{A}}{\partial t} \neq 0 \tag{44}$$

Of course, the curl-free solution could have bio-interactions having electric field and through this direct forces and energy absorption in the material. Using the potentials and the material parameters effective values of the sources (ρ_{eff} and $\boldsymbol{j}_{eff}$) can be introduced by potentials alone in case of (41) conditions, too:

$$\boldsymbol{j}_{eff} = \boldsymbol{j} + \frac{\partial \boldsymbol{P}}{\partial t} + rot(\boldsymbol{M}) = \frac{1}{\mu_0}\left(\Delta \boldsymbol{A} - \varepsilon_0 \mu_0 \frac{\partial^2 \boldsymbol{A}}{\partial t^2}\right) \tag{45}$$

and

$$\rho_{eff} = \rho - \varepsilon_0 div(\boldsymbol{P}) = -\varepsilon_0 \left(\Delta \varphi - \varepsilon_0 \mu_0 \frac{\partial^2 \varphi}{\partial t^2}\right) \tag{46}$$

The time-dependent curl-free solution is a solution in the "pure" $\boldsymbol{\mathcal{E}}$-field, which is the most common in the literature, and mistakenly used as field free. The entire free field solution requests the following conditions:

$$\frac{\partial \boldsymbol{A}}{\partial t} = 0 \quad \text{and} \quad grad(\varphi) = const. \tag{47}$$

Note due to (41) a χ scalar-potential could be introduced:

$$\boldsymbol{A} = -grad(\chi) \tag{48}$$

and so

$$\frac{\partial \boldsymbol{A}}{\partial t} + grad(\varphi) = grad\left(-\frac{\partial \chi}{\partial t} + \varphi\right) = 0 \tag{49}$$

Consequently, due to (18) the new scalar potential is time-dependent, as:

$$\varphi'(t) \Rightarrow \varphi - \frac{\partial \chi}{\partial t} \tag{50}$$

6. "Field-Free" Solution

The important question is the real field-free solution, when nor $\boldsymbol{\mathcal{E}}$ nor $\boldsymbol{B}$ exist.

$$\boldsymbol{B} = rot(\boldsymbol{A}) = 0 \quad \text{and} \quad \boldsymbol{\mathcal{E}} = -grad(\phi) - \frac{\partial \boldsymbol{A}}{\partial t} = 0 \tag{51}$$

The field-free solution does not mean that the space is also potential free. Could it interact with the biomatter?

The field-free condition involves a full annihilation of the existing but identical and opposite fields. Due to the opposite ponderomotoric forces, the fields will

vanish from the system. The zero $\boldsymbol{B}$ could be described by the two oppositely effective (destructive interference) vector potentials $\boldsymbol{A}$ and $\boldsymbol{A}^{\star}$:

$$\boldsymbol{B} = rot\left(\boldsymbol{A} - \boldsymbol{A}^{\star}\right) = 0 \tag{52}$$

In consequence, we could have a U scalar potential due to $rot\left(\boldsymbol{A}\right) = 0$ for the difference $\boldsymbol{A}_0$

$$\boldsymbol{A}_0 = \left(\boldsymbol{A} - \boldsymbol{A}^{\star}\right) = grad\left(U\right) \tag{53}$$

Let us choose at the same time the scalar potential on the way that $\boldsymbol{\mathcal{E}}$ has zero value as well:

$$\boldsymbol{\mathcal{E}} = -grad\left(\varphi - \varphi^{*}\right) - \frac{\partial\left(\boldsymbol{A} - \boldsymbol{A}^{\star}\right)}{\partial t} = 0 \tag{54}$$

In this case, using (52) we define:

$$\varphi_0 = \left(\varphi - \varphi^{*}\right) = \frac{\partial U}{\partial t} \tag{55}$$

Similarly to (20), the wave equations of these potentials belong to the field-free (source-free) conditions. In consequence of (45) and (46), the waves of null-potentials have zero effective charge- and current-densities

$$\begin{aligned} \boldsymbol{j}_{eff}\left(\boldsymbol{A},\varphi\right) + \boldsymbol{j}_{eff}\left(-\boldsymbol{A}^{\star},-\varphi^{*}\right) &= \boldsymbol{j}_{eff}\left(\boldsymbol{A}_0,\varphi_0\right) = 0 \\ \rho_{eff}\left(\boldsymbol{A},\varphi\right) + \rho_{eff}\left(-\boldsymbol{A}^{\star},-\varphi^{*}\right) &= \rho_{eff}\left(\boldsymbol{A}_0,\varphi_0\right) = 0 \end{aligned} \tag{56}$$

The sum is zero in the macroscopic view. However, it does not automatically make terms vanish, the terms could be non-zero in a microscopic view! In this way, the potentials associated with null-fields appear as waves:

$$\begin{aligned} \Delta\boldsymbol{A}_0 - \varepsilon_0\mu_0\frac{\partial^2\boldsymbol{A}_0}{\partial t^2} &= \mu_0\boldsymbol{j}_{eff} = 0 \\ \Delta\varphi_0 - \varepsilon_0\mu_0\frac{\partial^2\varphi_0}{\partial t^2} &= -\frac{\rho_{eff}}{\varepsilon_0} = 0 \end{aligned} \tag{57}$$

There is a huge challenge: the waves of potentials in field-free solutions have no dumping. In consequence of the zero-field conditions, a U scalar potential in (53) and (55) is the potentials' generator-function. Using (19), (52) and (54), a wave-equation is obtained for U:

$$\Delta U - \varepsilon_0\mu_0\frac{\partial^2 U}{\partial t^2} = 0 \tag{58}$$

The result in (58) supports the propagation of the scalar-wave (SW), which has no energy-dissipation in its transmission in the material [42]. The consequence of the SW concept, the Lorentz condition in (19) has been modified:

$$div\boldsymbol{A} + \varepsilon_0\mu_0\frac{\partial\varphi}{\partial t} = C \tag{59}$$

where $C \neq 0$ constant, and followingly [43]:

$$\Delta C - \varepsilon_0\mu_0\frac{\partial^2 C}{\partial t^2} = \mu\left(\frac{\partial\rho}{\partial t} + div\left(\boldsymbol{j}\right)\right) \tag{60}$$

Due to the charge conservation rule (3):

$$\left(\frac{\partial \rho}{\partial t} + div(\boldsymbol{j})\right) = 0 \tag{61}$$

Consequently:

$$\Delta C - \varepsilon_0 \mu_0 \frac{\partial^2 C}{\partial t^2} = 0 \tag{62}$$

Which is equal with (58).

Due to

$$\varepsilon_0 \mu_0 = \frac{1}{c^2} \tag{63}$$

These null-potential waves (together with the wave of the U potential (58)), are traveling by the speed of light in the vacuum (c), and so there are not dumping. [Note the limited velocity (c) of null-field potential obtained only with Lorencz condition (19).] Also, as we see from (16), the Φ flux obtained zero of course for field-free potentials for classical approach because

$$\oint_L \underline{A} \mathrm{d}\underline{r} = \oint_L -grad(U)\mathrm{d}\underline{r} = 0 \tag{64}$$

The field-free potential in the Schrodinger equation is:

$$\hat{\boldsymbol{H}}_0 = \frac{1}{2m_q}\left(\boldsymbol{p}_q - q \cdot grad(U)\right)^2 - q\frac{\partial U}{\partial t} \tag{65}$$

The application of the Lorentz condition (19) is equal with the wave-equation condition (58) of the scale-transformation because the

$$\begin{aligned} \boldsymbol{A} &\leftrightarrow \boldsymbol{A} + grad(U) \\ \phi &\leftrightarrow \phi - \frac{\partial U}{\partial t} \end{aligned} \tag{66}$$

transformations make identical results. Without damping the traveling waves, their interaction with the matter is questionable due to the missing energy loss. Is this challenge dissolvable?

7. The Stochastic Solution of the Field-Free Challenge

The mean's zero value does not mean that all terms vanish in the sum. The sum of the terms is zero (time-averaged), but because of the non-linear $\boldsymbol{P}$ and $\boldsymbol{M}$, the terms in sums in (56) could have non-zero values, keeping their sum zero. The effective current and charge densities as the fields' sources could have fluctuation around zero in the field-free solutions, which is, in fact, a fluctuating field with zero outcomes. Consequently, the zero-field potential could affect the electrical and magnetic polarization pattern, or ohmic terms, in creep. Ponderomotoric forces do not connect to zero potential waves. The forces reorganize only the pattern of charges and currents, rearrange the structure without energy absorption. The fluctuations drive the structural changes of the patterns. This is a direct potential effect without any change of the actual energy state only rear-

ranges its fluctuation distribution, which was shown on water-structure and in the water content of seeds too [44]. The vector potential affects the coupling matrixes of the transport equations and modifies the quantum-states of the water [45]. The water state changes show the clustering, and the experiments well agreed with the direction of the effect.

The spatio-temporal distribution of the fluctuations could vary without any change in the average (mean) values. Denote a living process without stochastic memory as $X(t)$. Its fluctuation by time *dt*:

$$X(t+dt)-X(t)=\Theta\left[X(t),t,dt\right] \tag{67}$$

The $t+dt$ time develops by its previous value at *t* time in (67). It is a Markovian process [46], determines the development in subsequent series of values. The $\Theta\left[X(t),t,dt\right]$ function depends on the *X*, *t*, *dt* variables, and

$$\lim_{dt\to 0} X(t+dt)=X(t). \tag{68}$$

A self-similar process characterized [47] [48] by:

$$\begin{aligned} X(t+dt)-X(t) &= \Theta\left[X(t),t,dt\right] \\ &= \sum_{i=1}^{n} X\left(t+i\frac{dt}{n}\right)-X\left(t+(i-1)\frac{dt}{n}\right) \\ &= \sum_{i=1}^{n} \Theta\left[X\left(t+(i-1)\frac{dt}{n}\right),(i-1)\frac{dt}{n},\frac{dt}{n}\right] \end{aligned} \tag{69}$$

and in $dt\to 0$ limit:

$$\begin{aligned} &t_{i-1}\to t \\ &X(t_{i-1})=X(t), \\ &\Theta\left[X(t),t,dt\right]=\textstyle\sum_{i=1}^{n}\Theta_i\left[X(t),t,\frac{dt}{n}\right]. \end{aligned} \tag{70}$$

The $\Theta\left[X(t),t,\frac{dt}{n}\right]$ terms are statistically independent representations in cases without memory. The sum of the *n*-pieces of the $\Theta\left[X(t),t,\frac{dt}{n}\right]$ is normally distributed, [49] at large *n* according to the functional central limit theorem. Consequently, from (70):

$$\begin{aligned} m\left\{\Theta\left[X(t),t,dt\right]\right\} &= n\cdot mean\left\{\Theta\left[X(t),t,\frac{dt}{n}\right]\right\} \\ \sigma\left\{\Theta\left[X(t),t,dt\right]\right\} &= n\cdot var\Theta\left\{\left[X(t),t,\frac{dt}{n}\right]\right\} \end{aligned} \tag{71}$$

where "*mean*" signifies the mean-value, *m* is the first, and σ is the second momentum of the distribution; and "*var*" denotes the standard deviation. The solutions of the function-Equation (71) are:

$$\begin{aligned} m\left\{\Theta\left[X(t),t,dt\right]\right\} &= A\left[X(t),t\right]dt \\ \sigma\left\{\Theta\left[X(t),t,dt\right]\right\} &= D\left[X(t),t\right]dt \end{aligned} \tag{72}$$

where A and D are smooth functions of X and t, as well as D is positive. With the normality conditions of (67) we get:

$$\begin{aligned} X(t+dt)-X(t) &= \Theta\left[X(t),t,dt\right] \\ &= \boldsymbol{N}_0\left[A(X,t)dt, D(X,t)dt\right] \\ &= A(X,t)dt + D^{\frac{1}{2}}\boldsymbol{N}_0(0,1)dt^{\frac{1}{2}} \end{aligned} \tag{73}$$

where $\boldsymbol{N}_0\left(m',\sigma'^2\right)$ is a normally distributed stochastic process with a mean and standard deviation m' and σ', respectively. (73) leads to a Langevin equation with an infinite standard deviation pumped by a normally distributed white noise ($\Gamma(t)$):

$$\frac{\mathrm{d}X}{\mathrm{d}t} = A(X,t) + D^{\frac{1}{2}}(X,t)\Gamma(t) \tag{74}$$

where:

$$\Gamma(t) = \lim_{dt\to 0} N\left(0, dt^{-1}\right) \tag{75}$$

A set of N self-similar stochastic processes could model the living system. Using the above considerations, we get a generalized Langevin equation:

$$\frac{\mathrm{d}X_i}{\mathrm{d}t} = A_i\left(X_j,t\right) + D_i^{\frac{1}{2}}\left(X_j,t\right)\Gamma(t), \quad (i,j=0,1,2,\cdots,N-1) \tag{76}$$

Assuming the $A_i\left(X_j,t\right)$ as a homogeneous linear function:

$$A_i\left(X_j,t\right) = \sum_{k=0}^{N-1} c_{ik}X_k \tag{77}$$

we get the comprehensive vectorial form of the generalized Langevin equation.

$$\frac{\mathrm{d}\boldsymbol{X}}{\mathrm{d}t} = \bar{\boldsymbol{C}}\boldsymbol{X} + \boldsymbol{D}^{1/2}\Gamma(t) \tag{78}$$

where $\boldsymbol{X}$, $\boldsymbol{D}$ and $\bar{\boldsymbol{C}}$ are derived from x_i, D_i and C_{ik}, respectively. According to the Onsager's conditions [50] the $\bar{\boldsymbol{C}}$ matrix is symmetrical, and the cross-effects are equal. The living matter forms a highly self-organized hierarchical structure, with a non-linear, dynamic equilibrium with no stationary processes [51]. Various physical, chemical, and physiological activities connect its subsystems, and interacting signals regulate and control a complex network. Even the simplest living biological systems show several interconnected processes on different time scales, determined by bioscaling connections [52]. Two identical living objects do not exist. The living matter is variable, changeable, mutable, and adaptable [53]. The living matter essentially differs from the lifeless ones [54]. While the thermal and quantum fluctuations in the lifeless states are negligible due to the system's size. These lifeless materials do not change between identical environmental conditions. The living object has many randomly transformed and altered homologous phases and states interacting with each other, mutating over time, involving a permanent and immanent change that allows adaptation, mutation, and natural selection. This dynamism appears in the change of the confirmation state of proteins, optimizing life's enzymatic reac-

tions. Due to the inherent fluctuations, the living matter is "noisy". The self-similar [55] and self-organized [56] behaviors drive the power-spectrum of their noise to a highly specialized frequency distribution, called pink-noise (1/f noise), [57] [58]. As we had shown earlier [59], the symmetrical, cyclical $\overline{\overline{\boldsymbol{C}}}$ matrix mandatory for pink noise in a system. Consequently, if a stochastic process is self-similar, then generates pink-noise with a power density spectrum by *f* frequency:

$$S(f) \propto \frac{1}{f} \tag{79}$$

This spectrum is independent of the kind and number of variables. The only assumption is its coupling matrix cyclically symmetric [59]. The living matter has such a matrix form, and its noises satisfy the (79) equation.

The vector-potential $\boldsymbol{A}$ is an axial vector (pseudovector), which at the reflection is opposite to its mirror image, without changing its magnitude, while the reflection of a true (polar) vector is exactly the same as its mirror image. The symmetry drastically changes by the effect of an axial vector, and Casimir's anti-symmetric relation [60] replaces the Onsager's symmetry:

$$\overline{\overline{\boldsymbol{C}}}(\boldsymbol{A};\boldsymbol{\omega}) = \overline{\overline{\boldsymbol{C}}}^{\mathrm{T}}(-\boldsymbol{A};-\boldsymbol{\omega}) \tag{80}$$

in the indexed form:

$$C_{ij}(\boldsymbol{A};\boldsymbol{\omega}) = C_{ji}(-\boldsymbol{A};-\boldsymbol{\omega}) \tag{81}$$

This effect is the rearranging of the fluctuation-noise distribution by the changing of the coupling of interconnected processes. This effect is independent of the presence of fields, only the action of the vector-potential ($\boldsymbol{A}$) is necessary. In a zero-field ("field-free") case, the microscopic (quantum-level) $\boldsymbol{A}$ could vary freely, keeping the condition (56) valid in the macroscopic scale.

Resulting from our above calculation, the presence of any axial-vectors (e.g., magnetic field $\boldsymbol{B}$ or vector potential $\boldsymbol{A}$) could destroy the symmetry of the $\overline{\overline{\boldsymbol{C}}}$ -matrix [30]. Consequently, any axial-vector changes the coupling between the transport processes and effectively affects the noise-spectra and the interconnection of the various homologous phases of the actual living state. This special interaction behavior could give a clue to explain the certain respiration change by a magnetic field [61] or a proposed tumor-genesis theory by magnetic field interactions [62] [63]. The action of axial vectors on the bio-system could affect its self-organizing ability, directly affecting individual cellular organizing autonomy, which characterizes the cancer cells. The pink-noise fluctuation (and the connected large-scale maximal entropy) is broken by the axial vectors' effect, modifying the transport properties and the interactions' symmetry. This effect could modify the critical state and the correlation length of the interactions [64] and could create a stress-like effect on the organism.

8. The Bio-Entropy

We are able to formulate our results on the basis of thermodynamics as well. The

highest deficiency of information (highest entropy) is achieved by the noise, which has Gaussian distribution [60] (Gaussian noise). Because the effective power-density of pink-noise is constant in all the characteristic scales, the Gaussian pink-noise then has maximal entropy in all the scales. The living system has special fractal dynamism, [65], in consequence of its self-similar stochastic behavior, it fluctuates by pink-noise, [59] [66]. The maximal entropy of Gaussian pink-noise allows an important conclusion: the living state's noise has maximal entropy (stable dynamic equilibrium) in all of the characteristic scales. Applied the Focker-Plank equation [67] we had shown [30] that the entropy fluctuation is connected to the coefficients of the Langevin-equation too:

$$\Delta S = k\frac{1}{2}\left(\boldsymbol{X}^{\mathrm{T}}\overline{\overline{\boldsymbol{Q}^{-1}}}\overline{\overline{\boldsymbol{C}}}\boldsymbol{X}\right). \tag{82}$$

In this case the elements of the cyclic $\overline{\overline{\boldsymbol{C}}}$-matrix will determine the change of the entropy. The applied field-free potential could change the configurational entropy and the noise-spectra of the living matter. This agrees well with the meaning of the minimum value of the volume integral of vector-potential squared ($\boldsymbol{A}^2_{\min}$), which is connected to the topological structures of the matter [30].

Numerous negative feedback loops control the homeostasis [68] [69], creating both the micro and macro-structures in equilibrium. The control forms oppositely effective physiologic feedback signal-pairs (promoter-suppressor actions) in various time-scales. The system is well controlled at all times. The homeostasis fixes the system in regulated dynamic equilibrium.

To characterize the homeostatic equilibrium, we may introduce a special entropy-definition. There are various proposals to calculate the entropy of finite data-series, which are coherent with the Shannon-type entropy [70]. Measuring the complexity of time-series was introduced by the Richman-Moorman-entropy (S_E) [71], which is the negative logarithm of that conditional probability that the vectors remain r-neighbors when we add a new sample-point to the time-series so the length of the vectors is elongated to $m+1$. Consequently:

$$S_E = InP\left(\left|x_i - x_j\right| \le r, \left|x_{i-1} - x_{j-1}\right| \le r\right) \tag{83}$$

The signals are kept in a definite interval, controlled on all scales of the homeostatic system. The entropy S_E of every signal in this state is identical and constant; $S_E = 1.8$, independent of the scale of measurements, [72]. The controlling physiological signals fluctuate around their average values. The fluctuation is time-fractal (pink-noise), which characterizes homeostasis.

A special method, called multiscale entropy analysis (MSE) [73], has proved the scale-independency of pink-noise in a definite interval of the signals, proven by evaluation of various physiological signals [74]. Applying the MSE for pink- and white-noises and the entropy vs. the applied scale factors (number of the members of the actual averaging) had different functions. The smoothing (filtering, cutting the high-frequencies) is irrelevant in the case of the pink-noise.

When the original was pink, the entropy remains constant on all scales in a very wide range of limits. The growing scale-factors decrease the white-noise entropy due to the very short correlation, but its entropy is high at the small scales due to the short-range correlations. While in the case of pink-noise, the short correlation is weak, but the long is strong.

9. Conclusions

Our present work shows the possible bio-effects of the electromagnetic potentials without the presence of electromagnetic fields. The effect is expected on the quantum level. It is based on the change of interactions of stochastic processes in living objects.

The practical benefit of the results is evident. It is not only a great possibility to work out new bio-effects, but it has industrial application possibilities also. The amplitude of field-free potential does not decrease because it does not induce Eddy current by the induction law to dissipate its energy. Consequently, effective communication methods can be achieved by applying low energies. Extensive research had been carried out in this field. An example, several patents were filed on behalf of Honeywell Inc., and granted on the communication system of this type [75].

Acknowledgements

This work was supported by the Hungarian National Research Development and Innovation Office PIACI KFI grant: 2019-1.1.1-PIACI-KFI-2019-00011.

Conflicts of Interest

The author declares no conflicts of interest regarding the publication of this paper.

References

[1] Lei, H., Pan, Y., Wu, R. and Lv, Y. (2020) Innate Immune Regulation under Magnetic Fields with Possible Mechanisms and Therapeutic Applications. *Frontiers in Immunology*, **11**, Article ID: 582772. https://doi.org/10.3389/fimmu.2020.582772

[2] Zhu, M., Yang, Z., Yu, H., *et al.* (2020) The Efficacy and Safety of Low-Frequency Rotating Static Magnetic Field Therapy Combined with Chemotherapy on Advanced Lung Cancer Patients: A Randomized, Double Blinded, Controlled Clinical Trial. *International Journal of Radiation Biology*, **96**, 943-950. https://doi.org/10.1080/09553002.2020.1748737

[3] Diao, Y.L., Sun, W.N., He, Y.Q., *et al.* (2017) Equivalent Magnetic Vector Potential Model for Low-Frequency Magnetic Exposure Assessment. *Physics in Medicine and Biology*, **62**, 7905-7922. https://doi.org/10.1088/1361-6560/aa8490

[4] Lednev, V.V. (1991) Possible Mechanism for the Influence of Weak Magnetic Fields on Biological Systems. *Bioelectromagnetics*, **12**, 71-75. https://doi.org/10.1002/bem.2250120202

[5] Belyavskaya, N.A. (2004) Biological Effects Due to Weak Magnetic Field on Plants. *Advances in Space Research*, **34**, 1566-1574.

https://doi.org/10.1016/j.asr.2004.01.021

[6] Tao, F.-M. (2003) Solvent Effects of Individual Water Molecules. In: Buch, V. and Devilin, J.P., Eds., *Water in Confining Geometries*, *Cluster Physics*, Springer Verlag, Berlin, 79-99. https://doi.org/10.1007/978-3-662-05231-0_5

[7] Buchachenko, A. (2016) Why Magnetic and Electromagnetic Effects in Biology Are Irreproducible and Contradictory? *Bioelectromagnetics*, **37**, 1-13. https://doi.org/10.1002/bem.21947

[8] Smith, W. (2004) Quanta and Coherence Effects in Water and Living Systems. *The Journal of Alternative and Complementary Medicine*, **10**, 69-78. https://doi.org/10.1089/107555304322848977

[9] Eden, D. (2008) Energy Medicine. Little, Brown Book Group.

[10] Rampl, I., Palko, L., Hyrsl, P. and Vojtek, L. (2012) Pulsed Vector Magnetic Potential Field Existence. *World Journal of Condensed Matter Physics*, **2**, 202-207. https://doi.org/10.4236/wjcmp.2012.24034

[11] Randerson, J. (2007) Electrosmog in the Clear with Scientists. *The Guardian*, January 18. https://www.theguardian.com/technology/2007/jan/18/guardianweeklytechnologysection4

[12] Oschman, J. (2000) Energy Medicine. The Scientific Basis, Churchill Livingstone.

[13] Jain, S. and Mills, P.J. (2010) Biofield Therapies: Helpful or Full of Hype? A Best Evidence Synthesis. *International Journal of Behavioral Medicine*, **17**, 1-16.

[14] Meyl, K. (2001) Scalar Waves: Theory and Experiments. *Journal of Scientific Exploration*, **15**, 199-205. https://doi.org/10.1054/cuor.2001.0179

[15] Tiller, W.A. (1999) Subtle Energies. *Science & Medicine*, **6**, May/June.

[16] Hall, H. (2005) A Review of Energy Medicine: The Scientific Basis. *Skeptic Magazine*, **11**. http://quackfiles.blogspot.com/2006/01/review-of-energy-medicine-scientific.html

[17] Bruhn, G.W. (2000) Commentary on the Chapter "Scalar Waves" in "Energy Medicine—The Scientific Basis". http://www.mathematik.tu-darmstadt.de/~bruhn/Commentary-Oschman.htm

[18] Bruhn, G.W. (2001) On the Existence of K. Meyl's Scalar Waves. *Journal of Scientific Exploration*, **15**, 206-210.

[19] Hornberger, J. (2019) Who Is the Fake One Now? Questions of Quackery, Worldliness and Legitimacy. *Critical Public Health*, **29**, 484-493. https://doi.org/10.1080/09581596.2019.1602719

[20] Maclis, R.M. (1993) Magnetic Healing, Quackery, and the Debate about the Health Effects of Electromagnetic Fields. *Annals of Internal Medicine*, **118**, 376-383. https://doi.org/10.7326/0003-4819-118-5-199303010-00009

[21] Mckenzie, B. (2020) Do Pulsed Electromagnetic Field Devices Offer Any Benefit? *Veterinary Practice News*, Jan. 2 2020.

[22] Basford, J.R. (2001) A Historical Perspective of the Popular Use of Electric and Magnetic Therapy. *Archives of Physical Medicine and Rehabilitation*, **82**, 1261-1269. https://doi.org/10.1053/apmr.2001.25905

[23] Barrett, S. (2008/2019) Magnet Therapy: A Skeptical View. *Quackwatch.* https://quackwatch.org/consumer-education/qa/magnet

[24] Maxwell, J.C. (1998) A Treatise on Electricity and Magnetism. Clarendon Press, Oxford.

[25] Lee, J.-H. and Chen, K.-M. (1982) Eddy Currents Induced by RF Magnetic Fields in Biological Bodies. *Radio Science*, **17**, 61S-76S.

[26] Pauli, W. (1958) Prinzipien Der Quantentheorie. Handbuch Der Physik bd. V. Springer Verlag, Berlin.

[27] Marton, L. (1952) Electron Interferometer. *Physical Review*, **85**, 1057-1058. https://doi.org/10.1103/PhysRev.85.1057

[28] Konopinsky, E.J. (1978) What the Electromagnetic Vector Potential Describes. *American Journal of Physics*, **46**, 499-502. https://doi.org/10.1119/1.11298

[29] Chambers, R.G. (1960) Shift of an Electron Interference Pattern by Enclosed Magnetic Flux. *Physical Review Letters*, **5**, 3-5. https://doi.org/10.1103/PhysRevLett.5.3

[30] Gubarev, F.V., Sodolsky, L. and Zakharov, V.I. (2001) On the Significance of the Vector Potential Squared. *Physical Review Letters*, **86**, 2220-2222. https://doi.org/10.1103/PhysRevLett.86.2220

[31] Gubarrev, F.V. and Zakharov, V.I. (2000) On the Emerging Phenomenology of $\langle (A_\mu^a)^2_{min} \rangle$ *Physics Letters B*, **501**, 28-36. https://doi.org/10.1016/S0370-2693(01)00085-5

[32] Mie, G. (1912) Grundlagen einer theorie der materie. *Annalen der Physik*, **37**, 39, 40. https://doi.org/10.1002/andp.19123441102

[33] Griffiths, D.J. (2007) Introduction to Electrodynamics. 3rd Edition, Pearson Education, Dorling Kindersley, London.

[34] Cleani, F., Di Tommaso, A.O. and Vassallo, G. (2017) Maxwell's Equations and Occam's Razor. *Journal of Condensed Matter Nuclear Science*, **25**, 100-128.

[35] Simonyi, K. (1979) Theoretische Elektrotechnik. Vol. 20, 7th Edition, VEB Verlag, Berlin.

[36] Vandas, M. and Romashets, E.P. (2003) A Force-Free Field with Constant Alpha in an Oblate Cylinder: A Generalization of the Lundquist Solution. *Astronomy & Aastrophysics*, **398**, 801-807. https://doi.org/10.1051/0004-6361:20021691

[37] Einstein, A. and Laub, J. (1908) Über die im elektromagnetischen Felde auf ruhende Körper ausgeübten ponderomotorischen Kräfte [On the Ponderomotive Forces Exerted on Bodies at Rest in the Electromagnetic Field]. *Annalen der Physik*, **26**, 541-550. (In German) https://doi.org/10.1002/andp.19083310807

[38] Landau, L.D. and Lifsic, E.M. (1973) Theoretical Physics, II. Field Theory. Nauka Press, Moscow. (In Russian)

[39] Rein, G. and Tiller, W.A. (1996) Anomalous Information Storage in Water: Spectroscopic Evidence for Non-Quantum Informational Transfer. *Proceedings* 3*rd International Symposium on New Energy*, Denver, 24-28 April 1996, 365.

[40] Aharonov, Y. and Bohm, D. (1959) Significance of Electromagnetic Potentials in Quantum Theory. *Physical Review*, **115**, 485-491. https://doi.org/10.1103/PhysRev.115.485

[41] Szasz, A., Vincze, Gy., Andocs, G. and Szasz, O. (2009) Do Field-Free Electromagnetic Potentials Play a Role in Biology? *Electromagnetic Biology and Medicine*, **28**, 135-147. https://doi.org/10.1080/15368370802711938

[42] Reed, D. and Hively, L.M. (2020) Implications of Gauge-Free Extended Electrodynamics. *Symmetry*, **12**, 2110. https://doi.org/10.3390/sym12122110

[43] Reed, D. (2019) Unravelling the Potentials Puzzle and Corresponding Case for the Scalar Longitudinal Electrodynamic Wave. *IOP Journal of Physics Conference Series*, **1251**, Article ID: 012043. https://doi.org/10.1088/1742-6596/1251/1/012043

[44] Andocs, G., Vincze, Gy., Szasz, O., Szendro, P. and Szasz, A. (2009) Effect of Curl-Free Potentials on Water. I. *Electromagnetic Biology and Medicine*, **28**, 166-181. https://doi.org/10.1080/15368370902724724

[45] Tao, F.-M. (2003) Solvent Effects of Individual Water Molecules, In: Buch, V. and Devilin, J.P., Eds., *Water in Confining Geometries*, *Cluster Physics*, Springer Verlag, Berlin, 79-99. https://doi.org/10.1007/978-3-662-05231-0_5

[46] Gagniuc, P.A. (2017) Markov Chains: From Theory to Implementation and Experimentation. John Wiley & Sons, Amsterdam, 1-235. https://doi.org/10.1002/9781119387596

[47] Gillespie, D.T. (1992) Markov Processes. Academic Press, San Diego.

[48] Gillespie, D.T. (1996) The Mathematics of Brown Motion and Johnson Noise. *American Journal of Physics*, **64**, 225. https://doi.org/10.1119/1.18210

[49] Vincze, I. (1971) Matematische Statistik mit Industriellen Anwendungen. Akadémiai Kiadó, Budapest.

[50] Onsager, L. (1931) Reciprocal Relations in Irreversible Processes. *Physical Review*, **37**, 405-426. https://doi.org/10.1103/PhysRev.37.405

[51] Walleczek, J. (2000) Self-Organized Biological Dynamics & Nonlinear Control. Cambridge University Press, Cambridge. https://doi.org/10.1017/CBO9780511535338

[52] Brown, J.H. and West, G.B. (2000) Scaling in Biology. Santa Fe Institute in the Sciences of Complexity, Oxford University Press, Oxford.

[53] Musha, T. and Sawada, Y. (1994) Physics of the Living State. IOS Press, Amsterdam.

[54] Marjan, M.I. and Szasz, A. (2000) Self-Organizing Processes in Non-Crystalline Materials: From Lifeless to Living Objects. OncoTherm Kft., Budapest.

[55] West, G.B., Brown, J.H. and Enquist, B.J. (1999) The Four Dimension of Life: Fractal Geometry and Allometric Scaling of Organisms. *Science*, **284**, 1677-1679. https://doi.org/10.1126/science.284.5420.1677

[56] Camazine, S., Deneubourg, J.-L., Franks, N.R., Sneyd, J., Theraulaz, G. and Bonabeau, E. (2003) Self-Organization in Biological Systems, Princeton Studies in Complexity. Princeton University Press, Oxford.

[57] West, B.J. (1990) Fractal Physiology and Chaos in Medicine. World Scientific, Singapore.

[58] Bassingthwaighte, J.B., Leibovitch, L.S. and West, B.J. (1994) Fractal Physiology. Oxford University Press, New York. https://doi.org/10.1007/978-1-4614-7572-9

[59] Szendro, P., Vincze, G. and Szasz, A. (2001) Pink Noise Behaviour of the Bio-Systems. *European Biophysics Journal*, **30**, 227-231. https://doi.org/10.1007/s002490100143

[60] Sharipov, F. (2006) Onsager-Casimir Reciprocal Relations Based on the Boltzmann Equation and Gas-Surface Interaction: Single Gas. *Physical Review E*, **73**, Article ID: 026110. https://doi.org/10.1103/PhysRevE.73.026110

[61] Reno, V.R. and Nutini, L.G. (1963) Effect of Magnetic Fields on Tissue Respiration. *Nature*, **198**, 204-205. https://doi.org/10.1038/198204b0

[62] Wolf, A.A. (1981) On a Unified Theory of Cancer Etiology and Treatment Based on the Superconduction Double-Dipole Model. *Physiological Chemistry and Physics*, **13**, 493-510.

[63] Easterly, C.E. (1981) Cancer Link to Magnetic Field Exposure: A Hypothesis. *American Journal of Epidemiology*, **114**, 169-175. https://doi.org/10.1093/oxfordjournals.aje.a113179

[64] Bak, P., Tang, Ch. and Wiesenfeld, K. (1987) Self-Organized Criticality: An Expla-

nation of 1/f Noise. *Physical Review Letters*, **59**, 381-384. https://doi.org/10.1103/PhysRevLett.59.381

[65] Goldberger, A.L., Amaral, L.A.N., Hausdorff, J.M., Ivanov, P.Ch. and Peng, C.-K. (2001) Fractal Dynamics in Physiology: Alterations with Disease and Aging. *PNAS Colloquium*, **99**, 2466-2472. https://doi.org/10.1073/pnas.012579499

[66] Szendro, P., Vincze, Gy. and Szasz, A. (2001) Bio-Response to White Noise Excitation. *Electro- and Magnetobiology*, **20**, 215-229. https://doi.org/10.1081/JBC-100104145

[67] Haken, H. (1977) Synergetics. Springer-Verlag, Berlin. https://doi.org/10.1007/978-3-642-66784-8

[68] Sneppen, K., Krisna, S. and Semsey, S. (2010) Simplified Models of Biological Networks. *Annual Review of Biophysics*, **39**, 43-59. https://doi.org/10.1146/annurev.biophys.093008.131241

[69] Turrigiano, G. (2007) Homeostatic Signaling: The Positive Side of Negative Feedback. *Current Opinion in Neurobiology*, **17**, 318-324. https://doi.org/10.1016/j.conb.2007.04.004

[70] Shannon, C.E. (1948) A Mathematical Theory of Communication. *Bell System Technical Journal*, **27**, 379-423 and 623-656. https://doi.org/10.1002/j.1538-7305.1948.tb00917.x

[71] Richman, J.S. and Moorman, J.R. (2000) Physiological Time-Series Analysis Using Approximate Entropy and Sample Entropy. *American Journal of Physiology*, **278**, H2039-H2049. https://doi.org/10.1152/ajpheart.2000.278.6.H2039

[72] Hegyi, G., Vincze, Gy. and Szasz, A. (2007) Axial Vector Interaction with Bio-Systems. *Electromagnetic Biology and Medicine*, **26**, 107-118. https://doi.org/10.1080/15368370701380835

[73] Costa, M., Goldberger, A.L. and Peng, C.K. (2005) Multiscale Entropy Analysis of Biological Signals. *Physical Review E*, **71**, Article ID: 021906. https://doi.org/10.1103/PhysRevE.71.021906

[74] Thuraisingham, R.A. and Gottwald, G.A. (2006) On Multiscale Entropy Analysis for Physiological Data. *Physica A*, **366**, 323-332. https://doi.org/10.1016/j.physa.2005.10.008

[75] Gelinas, R.C. (1984) United States Patent 4, 429, 280 (Jan. 31, 1984). https://doi.org/10.1093/nq/31-2-280

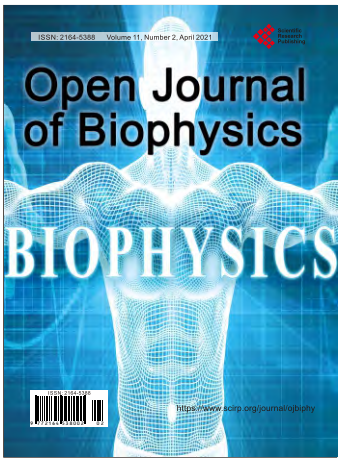

Call for Papers

Open Journal of Biophysics

ISSN Print: 2164-5388 ISSN Online: 2164-5396
https://www.scirp.org/journal/ojbiphy

Open Journal of Biophysics (OJBIPHY) is an international journal dedicated to the latest advancement of biophysics. The goal of this journal is to provide a platform for scientists and academicians all over the world to promote, share, and discuss various new issues and developments in different areas of biophysics.

Subject Coverage

All manuscripts must be prepared in English, and are subject to a rigorous and fair peer-review process. Accepted papers will immediately appear online followed by printed hard copy. The journal publishes original papers including but not limited to the following fields:

- Bioelectromagnetics
- Bioenergetics
- Bioinformatics and Computational Biophysics
- Biological Imaging
- Biomedical Imaging and Bioengineering
- Biophysics of Disease
- Biophysics of Photosynthesis
- Cardiovascular Biophysics
- Cell Biophysics
- Medical Biophysics
- Membrane Biophysics
- Molecular Biophysics and Structural Biology
- Physical Methods
- Physiology and Biophysics of the Inner Ear
- Proteins and Nucleic Acids Biophysics
- Radiobiology
- Receptors and Ionic Channels Biophysics
- Sensory Biophysics and Neurophysiology
- Systems Biophysics
- Theoretical and Mathematical Biophysics

We are also interested in: 1) Short Reports—2-5 page papers where an author can either present an idea with theoretical background but has not yet completed the research needed for a complete paper or preliminary data; 2) Book Reviews—Comments and critiques.

Notes for Intending Authors

Submitted papers should not have been previously published nor be currently under consideration for publication elsewhere. Paper submission will be handled electronically through the website. All papers are refereed through a peer review process. For more details about the submissions, please access the website.

Website and E-Mail

https://www.scirp.org/journal/ojbiphy **E-mail: ojbiphy@scirp.org**

What is SCIRP?

Scientific Research Publishing (SCIRP) is one of the largest Open Access journal publishers. It is currently publishing more than 200 open access, online, peer-reviewed journals covering a wide range of academic disciplines. SCIRP serves the worldwide academic communities and contributes to the progress and application of science with its publication.

What is Open Access?

All original research papers published by SCIRP are made freely and permanently accessible online immediately upon publication. To be able to provide open access journals, SCIRP defrays operation costs from authors and subscription charges only for its printed version. Open access publishing allows an immediate, worldwide, barrier-free, open access to the full text of research papers, which is in the best interests of the scientific community.

- High visibility for maximum global exposure with open access publishing model
- Rigorous peer review of research papers
- Prompt faster publication with less cost
- Guaranteed targeted, multidisciplinary audience

Scientific Research Publishing

Website: https://www.scirp.org

Subscription: sub@scirp.org

Advertisement: service@scirp.org